Centriole-independent centrosome assembly in interphase mammalian cells

Fangrui Chen[1], Jingchao Wu[1], Malina K. Iwanski[1], Daphne Jurriens[1], Arianna Sandron[1], Milena Pasolli[1], Gianmarco Puma[1], Jannes Z. Kromhout[1], Chao Yang[1], Wilco Nijenhuis[1,2], Lukas C. Kapitein[1,2] and Anna Akhmanova[1]

[1] Cell Biology, Neurobiology and Biophysics, Department of Biology, Faculty of Science, Utrecht University, Utrecht, Netherlands

[2] Center for Living Technologies, Eindhoven-Wageningen-Utrecht Alliance, the Netherlands

Correspondence: a.akhmanova@uu.nl

Abstract

The major microtubule-organizing center (MTOC) in animal cells, the centrosome, comprises a pair of centrioles surrounded by pericentriolar material (PCM), which nucleates and anchors microtubules. Centrosome assembly depends on the interactions of PCM with centrioles, PCM self-association and dynein-mediated transport. Here, we show that if centrioles are lost due to PLK4 depletion or inhibition, PCM still forms a single centrally located MTOC when non-centrosomal microtubule minus-end organization pathways are disabled. Acentriolar MTOC assembly depends on dynein-driven coalescence of PCM clusters with attached microtubule minus ends and requires γ-tubulin, pericentrin, CDK5RAP2 and ninein, but not NEDD1, CEP152 or CEP192. PCM self-assembly is inhibited by AKAP450-dependent PCM recruitment to the Golgi and by CAMSAP2-mediated microtubule minus-end stabilization. However, if CAMSAP2 is linked to a minus-end-directed motor, a single MTOC containing PCM components can still form, and its organization depends on the presence of pericentrin. Our results reveal that the formation of a single central MTOC in interphase mammalian cells is not strictly centriole dependent but can be driven by self-organization of PCM and microtubule minus ends.

Introduction

The centrosome is the major microtubule organizing center (MTOC) in animal cells. It consists of two centrioles surrounded by pericentriolar material (PCM) (reviewed in (Conduit et al., 2015; Paz and Luders, 2017)). Major PCM components are microtubule-nucleating and anchoring proteins, which can associate with centrioles and with each other. While for a long time PCM was thought to be amorphous, super-resolution microscopy studies have shown that it has a distinct organization, with some proteins likely attached to the centriole wall and others organized around them (Fu and Glover, 2012; Lawo et al., 2012; Mennella et al., 2014; Mennella et al., 2012). This distinct organization is more obvious in interphase than in mitosis, when the microtubule-organizing capacity of the centrosome increases due to enhanced PCM recruitment. Many PCM components are known to oligomerize and interact with each other, and recent work suggested that phase separation of interacting PCM components can contribute to centrosome assembly (Raff, 2019; Woodruff et al., 2017). This idea is underscored by data showing that various cell-type specific assemblies of PCM components can form clusters which can nucleate and organize microtubules and serve as MTOCs in the absence of centrioles, particularly during the formation of mitotic spindle poles (Balestra et al., 2021; Chinen et al., 2021; Gartenmann et al., 2020; Meitinger et al., 2020; Watanabe et al., 2020; Yeow et al., 2020). Furthermore, an important centrosome component, cytoplasmic dynein, is a motor that can bind to different PCM proteins and transport them to the centrosome-anchored microtubule ends, where these PCM proteins can nucleate and anchor more microtubules, thus generating a positive feedback loop in centrosome assembly (Balczon et al., 1999; Burakov et al., 2008; Purohit et al., 1999; Redwine et al., 2017). Dynein and its mitotic binding partner NuMA also strongly participate in the formation of mitotic and meiotic spindle poles (Chinen et al., 2020; Khodjakov et al., 2000; Kolano et al., 2012). The relative importance of different molecular pathways of MTOC assembly varies between cell systems and phases of the cell cycle.

Many interphase mammalian cell types have a radial microtubule array. In immune cells, which have a sparse microtubule network, the majority of microtubule minus ends are attached to the centrosome (reviewed in (Meiring et al., 2020)). However, in most commonly studied cultured cell lines, such as fibroblasts, epithelial, endothelial or cancer cells, microtubule networks are denser and not all minus ends can be directly attached to the centrosome. In such cells, non-centrosomal microtubule minus ends are often stabilized by the members of CAMSAP family (Jiang et al., 2014; Meng et al., 2008; Tanaka et al., 2012), and the Golgi apparatus serves as a secondary MTOC (Efimov et al., 2007; Rios, 2014; Wu et al., 2016; Zhu and Kaverina, 2013). If centrosomes are lost because centriole duplication is blocked by inhibiting the kinase PLK4 or depleting another essential centriole component, Golgi-dependent microtubule organization becomes predominant (Gavilan et al., 2018;

59 Martin et al., 2018; Wu et al., 2016). The ability of the Golgi complex to serve as an MTOC critically
60 depends on the Golgi adaptor AKAP450, which recruits several PCM components that nucleate
61 microtubules, including the γ-tubulin ring complex (γ-TuRC), CDK5RAP2 and pericentrin. Moreover,
62 AKAP450 also tethers microtubule minus ends stabilized by CAMSAP2 to the Golgi membranes
63 (Gavilan et al., 2018; Rivero et al., 2009; Wu et al., 2016). In the absence of AKAP450, the Golgi ribbon
64 is maintained, but neither PCM components nor CAMSAP-stabilized microtubule minus ends can be
65 attached to the Golgi membranes (Gavilan et al., 2018; Rivero et al., 2009; Wu et al., 2016). These
66 data seem to suggest that centrioles and/or Golgi membranes are essential for assembling a single
67 MTOC in interphase. However, this notion appears to be inaccurate: in our previous study in RPE1
68 cells, we observed that a single compact acentriolar MTOC (aMTOC) can still form after centriole loss
69 in AKAP450 knockout cells, which lack the ability to organize microtubules at the Golgi, if the
70 stabilization of free minus ends in these cells is disabled by knocking out CAMSAP2 (Wu et al., 2016).

71 Here, we used this observation as a starting point to explore the centriole-independent pathway of
72 centrosome assembly in interphase mammalian cells. We found that AKAP450/CAMSAP2 knockout
73 cells formed compact aMTOCs when PLK4 was either inhibited or depleted. aMTOC formation in these
74 cells required microtubules and depended on dynein, which brought together small PCM clusters with
75 attached minus ends. The resulting aMTOCs were often cylindrical rather than spherical in shape and
76 contained a subset of the major centrosome components. γ-tubulin, pericentrin, CDK5RAP2 and
77 ninein were necessary for the formation of compact aMTOCs, whereas some other major PCM
78 proteins, namely CEP192, CEP152 and NEDD1, were neither enriched in these structures nor required
79 for their formation. A single aMTOC could also form in the presence of CAMSAP2, if this protein was
80 directly linked to a microtubule minus-end-directed motor. The formation of a compact MTOC in such
81 cells still required pericentrin. Assembly of a single MTOC in interphase mammalian cells can thus be
82 achieved without centrioles through the concerted action of scaffolds for microtubule nucleation and
83 stabilization, provided that they are linked to a minus-end-directed motor.

84

85 **Results**

86 ***Assembly of microtubule-dependent aMTOCs in AKAP450/CAMSAP2 KO cells lacking PLK4 activity***

87 To induce centrosome loss in RPE1 cells, we treated these cells for 11 days with the PLK4 inhibitor
88 centrinone B (Wong et al., 2015) (Figure 1A,B). In wild type (WT) cells, PCM (detected with antibodies
89 against pericentrin) relocalized to the Golgi apparatus, and the microtubule array reorganized around
90 the Golgi membranes, as described previously (Gavilan et al., 2018; Wu et al., 2016) (Figure 1C,D). In

91 AKAP450 knockout cells, centriole loss led to the appearance of strongly dispersed PCM clusters,
92 which could no longer bind to the Golgi, and a highly disorganized microtubule system, consistent with
93 published work (Gavilan et al., 2018; Wu et al., 2016) (Figure 1D,E). In contrast, in AKAP450/CAMSAP2
94 double knockout cells, a single compact MTOC with microtubules focused around it was observed
95 (Figure 1D-F). Formation of a single compact aMTOC was also observed in AKAP450 knockout cells
96 transiently depleted of CAMSAP2 by siRNA transfection (Figure 1 – figure supplement 1A,B).

97 Unlike the centrosomes, which always have a spherical shape, compact aMTOCs in
98 AKAP450/CAMSAP2 knockout cells were cylindrical in ~35% of the cells, whereas in the remaining cells
99 that lacked centrioles based on staining for centrin, MTOCs had a round shape (~38% of the cells); the
100 rest of the centrin-negative cells either had dispersed PCM clusters (~7%) or no detectable PCM
101 clusters (~11%) (Figure 1 – figure supplement 1C,D). In contrast, ~72% of acentriolar AKAP450
102 knockout cells had dispersed PCM, while compact aMTOCs were very rare (Figure 1E, Figure 1 – figure
103 supplement 1C,D). Analysis by Stimulated Emission Depletion (STED) microscopy revealed that
104 cylindrical aMTOCs in AKAP450/CAMSAP2 knockout cells consisted of small clusters of PCM
105 components, including pericentrin, CDK5RAP2, γ-tubulin, ninein and dynein heavy chain (Figure 1F).
106 aMTOCs with a clearly elongated shape had an average length of ~11 µm and an average width of ~1.5
107 µm (Figure 1G).

108 To study PCM dynamics in aMTOCs, we generated cell lines stably expressing the PCM component
109 CDK5RAP2 tagged with GFP. In WT cells, GFP-CDK5RAP2 was localized to the centrosome and the Golgi
110 apparatus as expected (Figure 1 – figure supplement 2A). In centrinone-treated AKAP450/CAMSAP2
111 knockout cells, it was strongly enriched within aMTOCs and sometimes also present in small motile
112 clusters around an aMTOC (Figure 1H, Figure 1 – figure supplement 2B). Fluorescence recovery after
113 photobleaching (FRAP) assays showed that when the whole aMTOC was bleached, the recovery was
114 very slow and incomplete (Figure 1H, I). If an aMTOC was photobleached partially, the dynamics of
115 recovery showed cell-to-cell variability. Highly compacted aMTOCs did not undergo rearrangement
116 and displayed slow redistribution of GFP-CDK5RAP2. In more loosely organized aMTOCs, some
117 rearrangement of small PCM clusters was observed (Figure 1H,I); however, the recovery was still far
118 from complete. These data indicate that aMTOCs display variable degrees of compaction and are
119 composed of PCM clusters that display limited exchange of GFP-CDK5RAP2 with the cytoplasmic pool,
120 possibly because most of the GFP-CDK5RAP2 is accumulated within the aMTOC.

121 Next, we investigated whether centriole loss induced by means other than pharmacological PLK4
122 inhibition could also cause the formation of a single aMTOC in AKAP450/CAMSAP2 knockout cells. To
123 achieve efficient protein depletion in RPE1 cells, they were transfected with siRNAs twice (on day 0

124 and day 2), treated with thymidine starting from day 4 to block cell cycle progression and fixed and
125 stained on day 5 or day 7 (Figure 1 – figure supplement 1E). Depletion of PLK4 using siRNAs caused
126 the appearance of compact round or cylindrical aMTOCs, similar to those observed after PLK4
127 inhibition with centrinone, indicating that catalytically inactive PLK4 had no scaffolding role within
128 these structures (Figure 1 – figure supplement 1E-H). The percentage of cells with compact aMTOCs
129 increased over time (Figure 1 – figure supplement 1E-H), possibly due to the gradual depletion of PLK4.
130 In contrast, depletion of an essential centriole biogenesis factor CPAP (Kohlmaier et al., 2009; Schmidt
131 et al., 2009; Tang et al., 2009), which also led to centriole loss, was much less efficient in inducing
132 compact aMTOCs, and cylindrical a MTOCs were not observed (Figure 1 – figure supplement 1E-G).
133 After CPAP depletion, cells in which pericentrin formed dispersed clusters or no visible clusters
134 predominated (~67%, Figure 1 – figure supplement E-G). Treatment of CPAP-depleted
135 AKAP450/CAMSAP2 knockout cells with centrinone for 1 day promoted the assembly of compact
136 round or cylindrical aMTOCs, and the proportion of such cells increased to ~55% after 3 days of
137 centrinone treatment (Figure 1 – figure supplement 1E-I). We also tested whether the inhibition of
138 PLK1, a kinase that is known to be a major regulator of PCM self-assembly in mitosis (Haren et al.,
139 2009; Joukov et al., 2014; Lee and Rhee, 2011), has an effect on the formation of aMTOCs, but found
140 this not to be the case (Figure 1 – figure supplement 1F). We conclude that PCM can assemble into a
141 single stable MTOC in the absence of centrioles if PLK4 is either inactivated or depleted and the two
142 major pathways of microtubule nucleation and minus-end stabilization dependent on AKAP450 at the
143 Golgi membranes and CAMSAP2 are disabled.

144

145 ***Composition of aMTOCs and their effect on microtubule organization***

146 To investigate the composition of aMTOCs, we stained centrinone-treated AKAP450/CAMSAP2
147 knockout cells with antibodies against different centrosome and centriole markers and microtubule-
148 associated proteins (MAPs). As indicated above, abundant PCM components pericentrin, CDK5RAP2,
149 ninein and γ-tubulin colocalized within aMTOCs (Figure 1F). In contrast, three other major PCM
150 proteins, CEP152, CEP192 and NEDD1, could not be detected in these structures although they were
151 present in centrosomes of AKAP450/CAMSAP2 knockout RPE1 cells that were not treated with
152 centrinone (Figure 2A-C) and were also expressed in centrinone-treated cells (Figure 2 – figure
153 supplement 1A). We then individually depleted all these proteins in centrinone-treated
154 AKAP450/CAMSAP2 knockout cells using siRNAs. After the depletion of pericentrin, no clusters of
155 other PCM components could be detected (Figure 2D, Figure 2 – figure supplement 1B). To confirm
156 this result, we also attempted to knock out pericentrin in AKAP450/CAMSAP2 knockout cells, but such

157 cells were not viable, likely because centrosome defects in these cells caused prolonged mitosis and
158 p53-dependent G1 arrest (Fong et al., 2016; Lambrus et al., 2016; Meitinger et al., 2016). However,
159 we were able to knock out pericentrin in cells lacking AKAP450, CAMSAP2 and p53 (Figure 2 – figure
160 supplement 2), confirming that the loss of p53 makes the cells more tolerant to centrosome defects.
161 Similar to pericentrin-depleted cells, these quadruple knockout cells were unable to form a single
162 aMTOC when treated with centrinone (Figure 2E). In these acentriolar quadruple knockout cells,
163 CDK5RAP2, γ-tubulin and cytoplasmic dynein displayed no clustering, while ninein and PCM1, a
164 centriolar satellite protein that localizes closely around the centrosome in normal cells (Prosser and
165 Pelletier, 2020), formed small clusters distributed throughout the cytoplasm (Figure 2 – figure
166 supplement 3).

167 Depletion of CDK5RAP2, γ-tubulin or ninein in centrinone-treated AKAP450/CAMSAP2 knockout cells
168 did not prevent the formation of small pericentrin clusters, but these failed to coalesce into a single
169 aMTOC (Figure 2F-H, J, Figure 2 – figure supplement 1B). In contrast, depletion of CEP152, CEP192 or
170 NEDD1 had no effect on the formation of aMTOCs (Figure 2A-C, J, Figure 2 – figure supplement 1B), in
171 agreement with the fact these proteins could not be detected within these structures. aMTOCs
172 contained several centriole biogenesis factors, including CPAP, CP110 and CEP120, but lacked centrin
173 and CEP135; however, the depletion of several centriolar proteins did not affect aMTOC formation
174 (Figure 2J, Figure 2 – figure supplement 1C). We also detected within aMTOCs the component of the
175 HAUS complex HAUS2, the centrosomal protein CEP170, dynein, dynactin, CLASP1/2, CLIP-115, CLIP-
176 170, chTOG, KIF2A and KIF1C (Figure 2J, Figure 2 – figure supplement 1C). We tested the importance
177 of some of these proteins for aMTOC formation by siRNA-mediated depletion (see Figure 2J for an
178 overview), but among the tested proteins, only cytoplasmic dynein appeared essential for this process.
179 In dynein-depleted cells, no clusters of pericentrin or other PCM components could be detected after
180 centrinone treatment (Figure 2I,J). It is important to note, however, that because we used siRNAs to
181 reduce protein expression, we cannot exclude that the residual levels of some of the investigated
182 proteins were sufficient to support aMTOC formation. Since we have detected in the aMTOCs several
183 microtubule plus-end tracking proteins (+TIPs), such as CLIP-170, CLASP1/2 and the large subunit of
184 dynactin p150Glued, we also tested for the presence of the core components of the +TIP machinery,
185 EB1 and EB3, but found that they were not enriched within the aMTOCs (Figure 2J, Figure 2 –
186 supplement 4A). Using the previously described EB1/EB3/CAMSAP2mut cells, which lack EB3,
187 CAMSAP2 and C-terminal partner-binding half of EB1 (Yang et al., 2017), we generated a knockout cell
188 line that also lacks AKAP450 and found that aMTOCs could still form in these cells (Figure 2J, Figure 2
189 – figure supplement 4B,C). We conclude that compact aMTOCs formed in AKAP450/CAMSAP2

190 knockout cells concentrate many but not all components of conventional centrosomes and require
191 some of them for their formation.

192 As could be expected, the presence of an aMTOC was a critical determinant of microtubule
193 organization and density in acentriolar cells: microtubules were focused around aMTOCs if present
194 and disorganized in cells lacking aMTOCs. The strongest loss of microtubule density was observed in
195 cells lacking pericentrin, dynein or γ-tubulin, while milder phenotypes were observed in cells lacking
196 CDK5RAP2 or ninein (Figure 3A,B). To further characterize microtubule organization after the loss of
197 these proteins, we analyzed the proportion of the radial and non-radial microtubules. Whereas control
198 cells (AKAP450/CAMSAP2 knockout cells treated with centrinone and control siRNA) formed radial
199 microtubule networks with ~12% non-radial microtubules, acentriolar cells lacking pericentrin or
200 cytoplasmic dynein had ~46% non-radial microtubules, and the depletion of CDK5RAP2, ninein and γ-
201 tubulin led to an intermediate phenotype with 25-30% non-radial microtubules (Figure 3C,D). aMTOC
202 formed in AKAP450/CAMSAP2 knockout cells upon centrinone treatment can thus organize
203 microtubules and increase microtubule density (Figure 3E), and the formation and function of such an
204 aMTOC depend on pericentrin, CDK5RAP2, ninein, γ-tubulin and dynein.

205

206 ***Dynamics of aMTOC assembly and disassembly***

207 To test whether the formation and maintenance of aMTOCs in AKAP450/CAMSAP2 knockout cells
208 depends on microtubules, we depolymerized them by treating cells with nocodazole at 37°C and found
209 that aMTOCs fragmented into small clusters during nocodazole treatment and reassembled into a
210 single structure after nocodazole washout (Figure 4A-C). Because we found that aMTOC formation is
211 dynein-dependent, we also included in these experiments the dynein inhibitor dynapyrazole A
212 (Steinman et al., 2017). We confirmed that treatment with dynapyrazole A for 3 hrs had no effect on
213 dynein expression (Figure 4D) and found that the addition of this drug before nocodazole treatment
214 prevented the disassembly of aMTOCs, whereas treatment of cells with dynapyrazole A during
215 nocodazole washout strongly inhibited aMTOC re-assembly (Figure 4A-C). These data indicate that
216 microtubule-dependent dispersal and coalescence of PCM clusters into aMTOCs are driven by dynein
217 activity.

218 We next studied PCM dynamics using stably expressed GFP-CDK5RAP2 as a marker in live cells where
219 microtubules were labeled SiR-tubulin. GFP-CDK5RAP2 was mostly immobile within aMTOCs before
220 nocodazole treatment (Figure 1 – figure supplement 2B, Video 1). After a few minutes of nocodazole
221 treatment, when the microtubule density was significantly reduced, small PCM clusters started to

222 move out of the aMTOC and undergo rapid directional motility with speeds of up to 2 µm/sec, which
223 is within the range characteristic for cytoplasmic dynein (Schlager et al., 2014) (Figure 4E,F, Figure 4 –
224 figure supplement 1A, Video 1). Once microtubules were completely disassembled, the movement of
225 GFP-CDK5RAP2-positive clusters stopped, indicating that it is microtubule-dependent but occurs only
226 when the microtubule network is partly depolymerized. Since cluster dispersal towards the cell
227 periphery could be blocked by a dynein inhibitor, and since cytoplasmic dynein is a minus-end-directed
228 motor, these data indicate that during microtubule disassembly by nocodazole at 37°C, there is a
229 transient stage when PCM clusters interact with only a few microtubules, some of which have their
230 minus-ends facing outwards, and these microtubules serve as tracks for PCM transport. To support
231 this idea, we used motor-PAINT, a technique that employs nanometric tracking of purified kinesin
232 motors on the extracted cytoskeleton of fixed cells to super-resolve microtubules and determine their
233 orientation (Tas et al., 2017). Using this approach, we determined microtubule orientations in
234 centrinone-treated AKAP450/CAMSAP2 knockout cells and in cells that were also treated with
235 nocodazole for 15 min to induce partial microtubule disassembly (Figure 4G, Figure 4 – figure
236 supplement 1B). We found that the cells contained a significant number of minus-end-out
237 microtubules, and their proportion increased during early stages of nocodazole treatment, possibly
238 because minus-end-out microtubules are more stable (Figure 4G, e.g., minus-end-out microtubules
239 constituted ~23% of the total microtubule length determined from kinesin-1 trajectories in the
240 untreated cell and ~46% in the nocodazole-treated cell). These microtubules could serve as tracks for
241 outward movement of PCM, causing the disassembly of aMTOC when the overall microtubule density
242 around the aMTOC was strongly reduced (Figure 4H). These data suggest that the dense network of
243 PCM-anchored microtubule minus-ends keeps aMTOC compacted by dynein-mediated forces, which
244 can, however, pull it apart when the microtubules are disorganized.

245 Next, we investigated in more detail aMTOC reassembly during nocodazole washout. Small PCM
246 clusters positive for pericentrin, CDK5RAP2, γ-tubulin and the centriolar satellite protein PCM1 that
247 co-localized with the ends of microtubules labeled with EB1 could be detected 30 s after nocodazole
248 washout; these nascent microtubules did not colocalize with the Golgi membranes (Figure 5A, Figure
249 5 – figure supplement 1A). Ninein was not detected within the clusters at this early stage of
250 microtubule regrowth but could be found 2 min after nocodazole washout. In contrast, no clusters of
251 CEP192 or NEDD1 were observed even 10 min after nocodazole washout (Figure 5A, Figure 5 –
252 supplement 1A, B). Depletion of pericentrin, CDK5RAP2 and γ-tubulin strongly inhibited microtubule
253 nucleation in these conditions, whereas the depletion of dynein heavy chain or ninein had a milder
254 effect (Figure 5B,C). Live cell imaging with GFP-CDK5RAP2 and SiR-tubulin showed that CDK5RAP2
255 clusters with attached microtubules coalesced by undergoing microtubule-based movements (Figure

256 5D), and measurements in cells fixed at different time points after nocodazole washout showed that
257 a partly radial microtubule system emerged already 2 min after nocodazole washout (Figure 5 – figure
258 supplement 1C). Reassembly of a single aMTOC in the central part of the cell happened within ~15
259 min after nocodazole washout, though typically it was less compact than in cells that were not treated
260 with nocodazole (Figure 5D-G). Depletion of pericentrin, γ-tubulin and dynein heavy chain strongly
261 inhibited the reformation of a radial microtubule network during nocodazole washout, whereas the
262 effect of depleting CDK5RAP2 and ninein was less strong (Figure 5 – figure supplement 1C-E). Live cell
263 imaging of acentriolar AKAP450/CAMSAP2 knockout RPE1 cells stably expressing GFP-CDK5RAP2
264 showed that when pericentrin was depleted, CDK5RAP2 clusters were not detectable and the
265 microtubule network, both before nocodazole treatment and after nocodazole washout, was
266 disorganized (Figure 5 – figure supplement 2, Video 2). Taken together, our data show that pericentrin
267 and γ-tubulin form microtubule-nucleating and anchoring units that can be assembled into larger
268 structures by dynein-based transport. CDK5RAP2 contributes to microtubule nucleation activity,
269 whereas ninein appears to act somewhat later and contributes to the formation of a single compact
270 aMTOC.

271

272 ***The role of CAMSAP2-stabilized minus ends in defining microtubule network geometry***

273 All the components of aMTOCs observed in AKAP450/CAMSAP2 knockout cells were also present in
274 AKAP450 knockout cells, yet these cells did not form a single aMTOC upon centrinone treatment
275 because they expressed CAMSAP2. In these cells, CAMSAP2-stabilized microtubule minus ends were
276 randomly distributed throughout the lamella, and microtubules were largely disorganized, although
277 many microtubules tended to co-align with the long axis of the lamella or of the whole cell (Figure 6A).
278 Live imaging of GFP-CDK5RAP2 together with SiR-tubulin in these cells showed that PCM clusters
279 moved along microtubules and occasionally encountered each other, but the movement directions
280 were random and PCM clusters did not coalesce into a single structure (Figure 6B, Figure 6 – figure
281 supplement 1A, Video 3). Treatment with nocodazole and subsequent nocodazole washout confirmed
282 that the motility of GFP-CDK5RAP2 clusters in centrinone-treated AKAP450 knockout cells is
283 microtubule-dependent and that these clusters can nucleate microtubules and move together with
284 their ends, but do not converge into a single compact aMTOC (Figure 6 – figure supplement 1A-C,
285 Video 3). Treatment with dynapyrazole A strongly inhibited the movements of small PCM clusters
286 (Figure 6 – figure supplement 1D,E, Video 4), indicating that they are dynein-driven. After the
287 depletion of pericentrin, GFP-CDK5RAP2 became completely diffuse, and it also did not form any
288 clusters during nocodazole treatment or washout (Figure 6 – figure supplement 2, Video 5), indicating

289 that clustering of GFP-CDK5RAP2 in AKAP450 knockout cells is pericentrin-dependent. Based on these
290 data, we conclude that in AKAP450 knockout cells, pericentrin still forms PCM clusters that can
291 nucleate microtubules and can be moved by dynein along other microtubules. However, since
292 CAMSAP2-stabilized microtubule minus-ends in these cells are not attached to the Golgi membranes
293 and do not interact with dynein, they are distributed randomly. This results in a disorganized
294 microtubule network, with the minus ends pointing both in- and outwards, and leads to random
295 motility of PCM clusters that prevents assembly of a single compact aMTOC (Figure 6C).

296 We next wondered whether we could force aMTOC formation in AKAP450 knockout cells by linking
297 CAMSAP2-stabilized minus ends to a minus-end-directed motor. To avoid potential cell toxicity
298 associated with manipulating cytoplasmic dynein, we used the motor-containing part of a moss
299 kinesin-14, type VI kinesin-14b from the spreading earthmoss *Physcomitrella patens* (termed here
300 ppKin14). The C-terminal motor-containing part of this protein can efficiently induce minus-end-
301 directed motility of different cargoes in mammalian cells when it is tetramerized through a fusion with
302 the leucine zipper domain of GCN4 (GCN4-ppKin14-VIb (861–1321)) and recruited to cargoes using
303 inducible protein heterodimerization (Jonsson et al., 2015; Nijenhuis et al., 2020). Here, we employed
304 a chemical heterodimerization system that is based on inducible binding of two protein domains, FRB
305 and FKBP, upon the addition of a rapamycin analog (rapalog) (Pollock et al., 2000). To ensure that all
306 CAMSAP2-decorated microtubule minus ends are linked to kinesin-14, we rescued centrinone-treated
307 AKAP450/CAMSAP2 knockout cells by expressing CAMSAP2 fused to a tandemly repeated FKBP
308 domain (2FKBP-mCherry-CAMSAP2) (Figure 6D-F). This construct was co-expressed with the FRB-
309 GCN4-tagBFP-ppKin14 fusion, which by itself localized quite diffusely, with only a weak enrichment
310 along microtubules, as described previously (Nijenhuis et al., 2020) (Figure 6D,F). In the absence of
311 rapalog, CAMSAP2-decorated microtubule minus ends were distributed randomly, similar to
312 endogenous CAMSAP2 in AKAP450 knockout cells (Figure 6F). However, upon rapalog addition,
313 ppKin14 was rapidly recruited to CAMSAP2-decorated microtubule ends, and after 2 hrs, more than
314 90% of cells acquired a radial microtubule organization (Figure 6E-G). In rapalog-treated cells,
315 CAMSAP2-bound microtubule minus ends formed either a tight cluster or a “whirlpool-like” ring in the
316 cell center (Figure 6D-G, Figure 6 – figure supplement 1F). The whirlpool-like arrangement likely comes
317 about when CAMSAP2-stretches are a bit longer and keep sliding against each other, forming a
318 nematic circular bundle. The major aMTOC components, pericentrin, CDK5RAP2, γ-tubulin and ninein
319 were also concentrated within the CAMSAP2 cluster, although they did not form a strongly compacted
320 assembly (Figure 6G, Figure 6 – figure supplement 1F). These data indicate that the positioning of
321 stabilized minus-ends is a very important determinant of the overall microtubule organization in

322 interphase cells, and that linking a minus-end-directed motor, even a heterologous one, to stable
323 minus ends can induce self-assembly of a radial microtubule array.

324

325 ***The role of PCM in CAMSAP2-driven microtubule organization***

326 Next, we tested whether PCM plays a role in CAMSAP-driven aMTOC formation by inducibly attaching
327 CAMSAP2 to ppKin14 in centrinone-treated cells with both AKAP450 and pericentrin knocked out
328 (AKAP450/CAMSAP2/p53/pericentrin knockout). In the absence of rapalog, CAMSAP2-stabilized
329 minus ends and the whole microtubule network were disorganized, as expected (Figure 7A,D). After
330 rapalog addition, microtubules acquired a radial organization, but their minus ends usually did not
331 converge in a single spot but rather accumulated in a ~30-70 µm-large ring-like structure (Figure 7A,D,
332 Figure 7- figure supplement 1, Video 6). Staining for PCM markers showed that CDK5RAP2 and γ-
333 tubulin were enriched in the vicinity of CAMSAP2-positive microtubule minus ends, whereas ninein
334 appeared rather diffuse (Figure 7A). To determine the nature of the structure "corralled" by the ring
335 of CAMSAP2-decorated minus ends in rapalog-treated cells, we stained for different membrane
336 organelles and found that whereas there was no strong correlation with the nucleus, Golgi membranes
337 or lysosomes, the majority of mitochondria were found within the CAMSAP2 ring, and the
338 endoplasmic reticulum (ER) displayed increased density overlapping with the CAMSAP2 ring (Figure
339 7B, Figure 7 - figure supplement 1B). It therefore appeared that in the absence of pericentrin,
340 CAMSAP2-decorated minus ends were brought together by ppKin14, but their convergence was
341 impeded by the ER and possibly mitochondria, which were enriched in the central, thicker part of the
342 cell before rapalog addition (see the upper panel of Figure 7 - figure supplement 1B). Transient
343 transfection of centrinone-treated AKAP450/CAMSAP2/p53/pericentrin knockout cells with GFP-
344 pericentrin rescued the formation of a tight CAMSAP2 cluster upon rapalog treatment (Figure 7C). Our
345 data show that pericentrin-containing PCM contributes to the formation of an aMTOC driven by
346 minus-end-directed transport of CAMSAP2-stabilized minus-ends.

347 To support this notion further, we also generated cells that were knockout for AKAP450, CAMSAP2,
348 CDK5RAP2, myomegalin (MMG, homologue of CDK5RAP2), p53 and pericentrin. To achieve this, we
349 used the previously described RPE1 cell line knockout for AKAP450, CAMSAP2, CDK5RAP2 and MMG
350 (Wu et al., 2016), in which we sequentially knocked out p53 and pericentrin (Figure 7 – figure
351 supplement 2A-G). While it was not possible to induce centriole loss by centrinone treatment in
352 AKAP450/CAMSAP2/CDK5RAP2/MMG knockout cells because the proliferation of these cells was
353 arrested in the absence of centrioles (Wu et al., 2016), centriole removal was successful in
354 AKAP450/CAMSAP2/CDK5RAP2/MMG/p53/pericentrin knockout cells due to the absence of p53 and

355 led to microtubule disorganization (Figure 7 – figure supplement 2H). Interestingly, when these cells
356 were co-transfected with FKBP-linked CAMSAP2 and FRB-linked ppKin14 and treated with rapalog
357 (Figure 6D), we observed that CAMSAP2 clustering was even less efficient than in
358 AKAP450/CAMSAP2/p53/pericentrin knockout cells (Figure 7D,E). 49% of
359 AKAP450/CAMSAP2/CDK5RAP2/MMG/p53/pericentrin knockout cells had small bundles of CAMSAP2
360 stretches dispersed throughout the cytoplasm, and only 37% of these cells formed a ring of CAMSAP2-
361 decorated minus ends, whereas 80% of AKAP450/CAMSAP2/p53/pericentrin knockout cells did form
362 such a ring. We examined the ER and mitochondria in these cells and found that in cells that did form
363 a CAMSAP2 ring, the ER displayed an overlapping ring-like density, although the mitochondria inside
364 the CAMSAP2 ring were more scattered compared to those of AKAP450/CAMSAP2/p53/pericentrin
365 knockout cells (Figure 7 – figure supplement 1B). In cells with dispersed CAMSAP2-positive bundles,
366 no increased ER density or central accumulation of mitochondria were observed (Figure 7 – figure
367 supplement 1B). These data further support the notion that during the formation an aMTOC, minus-
368 end-directed transport of CAMSAP2-stabilized minus ends needs to be augmented by PCM function
369 dependent on pericentrin, CDK5RAP2 and possibly also MMG.

370 **Discussion**

371 In this study, we explored the mechanisms driving MTOC assembly in acentriolar cells and showed
372 that centrioles are not strictly needed to form a central compact MTOC and a radial microtubule array
373 in interphase mammalian cells. Our data indicate that in the absence of the pathways that promote
374 formation of non-centrosomal microtubules, cytoplasmic dynein can assemble a single aMTOC by
375 bringing together microtubule minus ends that are nucleated and stabilized by PCM. However, the
376 formation of MTOC in acentriolar cells is slow and less robust than in centriole-containing cells. Similar
377 to the formation of spindle poles in mitosis (Meraldi, 2016), centrioles can thus be regarded as
378 catalysts of interphase centrosome assembly.

379 We found that self-assembly of aMTOCs is driven by dynein-dependent transport of PCM
380 components that include pericentrin, CDK5RAP2, γ-TuRC and ninein. In acentriolar cells that we
381 studied, the major scaffold for interphase PCM assembly is pericentrin, which recruits CDK5RAP2 and
382 ninein, in agreement with previous work (Chen et al., 2014; Delaval and Doxsey, 2010; Kim and Rhee,
383 2014; Lawo et al., 2012). Moreover, it has been established previously that CDK5RAP2 binds and
384 activates γ-TuRC (Choi et al., 2010; Fong et al., 2008), and the same may be true for pericentrin
385 (Takahashi et al., 2002) and possibly also for ninein (Delgehyr et al., 2005; Mogensen et al., 2000).
386 Pericentrin and ninein can both directly interact with dynein (Purohit et al., 1999; Redwine et al.,
387 2017), and an interaction between CDK5RAP2 and dynein has also been reported (Jia et al., 2013; Lee
388 and Rhee, 2010). All these interactions likely contribute to the formation of aMTOCs.

389 Pericentrin-dependent MTOC assembly has also been observed in acentriolar mitotic cells
390 (Chinen et al., 2021; Watanabe et al., 2020), but the interphase pathway displays some interesting
391 differences. It seems that while oligomerization and clustering of pericentrin molecules is important
392 for MTOC formation both in interphase and in mitosis, during mitotic entry, pericentrin may form
393 condensates (Jiang et al., 2020), while in interphase, dynein-mediated motility dominates the behavior
394 of pericentrin clusters. The compact aMTOC structure we observed in interphase was not simply a
395 result of small pericentrin- and CDK5RAP2-positive PCM clusters coming into proximity of each other
396 and sticking together, but also depended on active transport. In AKAP450 knockout cells, we also
397 frequently observed CDK5RAP2-containing PCM clusters encountering each other, yet they did not
398 coalesce into a single MTOC because they kept moving in random directions on CAMSAP2-stabilized
399 microtubules. When most CAMSAP2-decorated minus ends were brought together by a minus-end-
400 directed motor, pericentrin accumulated in the vicinity of such an artificially formed MTOC and
401 contributed to its formation, but did not form a single solid body, likely because it kept moving along
402 the sides of CAMSAP2-decorated microtubules but was not attached to their outermost minus ends.

403 A strongly compacted aMTOC only formed when most microtubule minus ends were anchored by
404 PCM clusters. The shape of the MTOC was cylindrical rather than spherical in a significant proportion
405 of such cells, suggesting that it was optimized for increasing the surface area. A larger surface area
406 allows for the attachment of more microtubules and fits with the idea that aMTOC formation is
407 primarily driven by the coalescence of minus-end-attached PCM clusters rather than free oligomers
408 of PCM proteins. Altogether, it appears that active, dynein-mediated transport of pericentrin-based
409 PCM clusters rather than spontaneous formation of PCM condensates is the major driver of interphase
410 aMTOC assembly. This explains why aMTOCs are exquisitely sensitive to microtubule disassembly by
411 nocodazole: during intermediate stages of microtubule loss, PCM complexes that are no longer
412 attached to microtubule minus ends start to move on the remaining microtubules, and therefore, a
413 few surviving minus-end-out microtubules can serve as rails to drive the dispersal of the aMTOC
414 (Figure 4H). Furthermore, PCM dynamics within aMTOCs show no hallmarks of liquid droplet-like
415 behavior: PCM components do not appear to be in equilibrium with the soluble cytoplasmic pool, and
416 GFP-CDK5RAP2 displays very slow redistribution within the aMTOC. As CDK5RAP2 is recruited to the
417 aMTOC by pericentrin, these data suggest that pericentrin is also quite immobile within aMTOCs.

418 Although pericentrin can directly bind to γ-TuRC, CDK5RAP2 and ninein are also needed for
419 aMTOC formation. Analysis of different stages of microtubule recovery after nocodazole washout
420 suggested that CDK5RAP2 is important for efficient microtubule nucleation, consistent with its role as
421 an activator of γ-TuRC (Choi et al., 2010). Ninein can be detected within nascent aMTOC structures
422 with some delay after their formation and might be important for stabilizing these structures or
423 promoting minus-end anchoring, as proposed by many previous studies (Abal et al., 2002; Chong et
424 al., 2020; Delgehyr et al., 2005; Goldspink et al., 2017; Lechler and Fuchs, 2007; Mogensen et al., 2000;
425 Shinohara et al., 2013; Zheng et al., 2020). The importance of ninein for the formation of aMTOCs
426 illustrates its function in minus-end organization within the PCM that is independent of centriolar
427 appendages, one of the sites of ninein localization at the centrosome (Chong et al., 2020; Delgehyr et
428 al., 2005; Sonnen et al., 2012).

429 A major difference between interphase and mitotic MTOC assembly is the role of other major
430 PCM components, CEP192 and the γ-TURC-binding protein NEDD1. In our experiments, CEP192 and
431 its binding partners CEP152 and NEDD1 (Gomez-Ferreria et al., 2012; Joukov et al., 2014; Kim et al.,
432 2013; Sonnen et al., 2013) were not enriched at aMTOCs, and their depletion appeared to have no
433 impact on aMTOC formation. This is surprising, because during mitosis, CEP192 is essential (Gomez-
434 Ferreria et al., 2007; Joukov et al., 2014; Yang and Feldman, 2015; Zhu et al., 2008), and in acentriolar
435 cells that rely on pericentrin and CDK5RAP2 for spindle pole formation, CEP192 is recruited to
436 pericentrin clusters (Chinen et al., 2021; Watanabe et al., 2020). Moreover, although NEDD1 is

437 targeted to centrosomes by CEP192, pericentrin can also contribute to the centrosomal targeting of
438 NEDD1 independently of CEP192 (Chi et al., 2021). Therefore, the lack of enrichment of CEP192,
439 CEP152 and NEDD1 in interphase aMTOC is unexpected, particularly because these three proteins are
440 present within interphase PCM at the centrosome, and multiple other centrosomal and centriolar
441 proteins and MAPs are recruited to aMTOCs. Among the proteins enriched at aMTOCs, we did not
442 identify any additional factors that would be crucial for aMTOC formation, but it is of course possible
443 that this process requires some proteins that we have not tested. It is also important to note that
444 because siRNA-mediated protein depletion may be incomplete, we cannot exclude that low amounts
445 of some of the tested centrosome components or MAPs are sufficient to support aMTOC assembly.

446 An interesting question that remains unanswered by our work is the inhibitory role of PLK4 in
447 interphase aMTOC formation. We did observe aMTOCs in cells depleted of PLK4, indicating that, unlike
448 cells lacking TRIM37, which form PCM clusters containing catalytically inactive PLK4 (Meitinger et al.,
449 2020; Yeow et al., 2020), interphase cells studied here do not rely on enzymatically inactive PLK4 for
450 PCM assembly. PLK4 is known to phosphorylate NEDD1 (Chi et al., 2021), and it is possible that the
451 lack of phosphorylation prevents this γ-TuRC activator and its partners, such as CEP192, from
452 participating in interphase aMTOC assembly. It is of course also possible that PLK4 phosphorylation
453 inhibits the interactions or activities of some of the players that are driving aMTOC formation.

454 An important conclusion of our study is the key role of CAMSAP2-stabilized minus ends in
455 determining microtubule organization in the absence of the centrosome. Unlike the PCM components,
456 CAMSAP2 does not interact with dynein, and if CAMSAP2-decorated minus ends are not attached to
457 the Golgi membranes, which are themselves subject to dynein-based transport, the microtubule
458 system becomes strongly disorganized. However, linking a minus-end-directed motor to CAMSAP2 can
459 restore a radial microtubule array with a single MTOC, provided that the major active PCM
460 components are also transported to microtubule minus ends due to the presence of pericentrin.
461 Surprisingly, in the absence of pericentrin, minus-end-directed convergence of CAMSAP2-bound
462 minus ends drives "corralling" of ER and mitochondria. Since there are currently no indications that
463 CAMSAP2 specifically interacts with ER or mitochondria, we favor the idea that these organelles, which
464 are normally enriched in the central, thicker part of the cell, form a physical obstacle for CAMSAP2-
465 ppKin14-driven minus-end clustering, and that dynein-mediated transport of pericentrin-anchored
466 minus ends helps to overcome this obstacle and form a compact aMTOC. Removal of CDK5RAP2 and
467 its homologue MMG in these conditions further inhibits minus-end organization and aMTOC
468 formation. This indicates that minus-end-directed transport of CAMSAP2-stabilized microtubule
469 minus ends is by itself not sufficient to form a radial microtubule network but needs to synergize with
470 PCM-dependent microtubule organization.

471 These data have implications for understanding how microtubules are reorganized in
472 differentiated cells. During cell differentiation, the centrosome often loses its activity, and PCM is
473 redeployed to other cellular locations (Martin and Akhmanova, 2018; Muroyama and Lechler, 2017;
474 Sallee and Feldman, 2021). Our study shows that interphase PCM has the potential to self-assemble,
475 but this ability is inhibited by PLK4, and the regulation of this kinase may thus influence PCM assembly
476 and activity at different cellular locations. Further, we show that CAMSAP-dependent minus-end
477 organization has a very dominant effect on the overall microtubule network geometry but can be
478 affected by the presence of PCM components. This suggests that during microtubule reorganization
479 in differentiated cells, PCM-dependent and CAMSAP-dependent pathways are likely to be co-
480 regulated. This idea is strongly supported by studies of microtubule organization at the Golgi
481 membranes (Gavilan et al., 2018; Wu et al., 2016) and the apical membranes of polarized epithelial
482 cells, where components of both pathways colocalize and can display some redundancy (Goldspink et
483 al., 2017; Khanal et al., 2016; Noordstra et al., 2016; Toya et al., 2016; Wang et al., 2015). In muscle
484 cells, CAMSAPs are not expressed, and the organization of microtubule minus-ends is driven by the
485 Golgi adaptor AKAP450 and some PCM proteins that are localized to the nuclear envelope and the
486 Golgi (Gimpel et al., 2017; Oddoux et al., 2013; Vergarajauregui et al., 2020). In neurons, minus-ends
487 can be organized by PCM, CAMSAPs, the Golgi membranes and endosomes (Fu et al., 2019; Garbrecht
488 et al., 2021; Liang et al., 2020; Magescas et al., 2021; Pongrakhananon et al., 2018; Yau et al., 2014),
489 though the cross-talk between different pathways is insufficiently understood. One common feature
490 between these different systems and the data described here is that the function of PCM components,
491 redeployed to different locations in differentiated cells, is dominated by two structurally related
492 adaptors, AKAP450 and pericentrin, as well as CDK5RAP2 and ninein. In contrast, CEP192 seems to
493 have a much more important role in mitotic rather than interphase cells. In line with this idea, recent
494 work demonstrated that certain types of worm neurons contain an aMTOC that is formed by the
495 functional counterparts of CDK5RAP2 (SPD-5), pericentrin (PCMD-1) and γ-tubulin, but lacks
496 CEP192/SPD-2 (Garbrecht et al., 2021; Magescas et al., 2021). Future work will show whether this
497 distinction is generally applicable. It would also be important to know to which extent PCM transport
498 along microtubules contributes to microtubule organization in different cell types, and to determine
499 how the biochemical and functional coupling between different pathways of microtubule nucleation
500 and minus-end stabilization defines various geometries of microtubule networks.

501 **Materials and Methods**

502 ***DNA constructs and protein purification***

503 To generate the lentiviral vector pLVX-GFP-CDK5RAP2-IRES-Puro, pLVX-IRES-Puro plasmid (Clontech)
504 was digested with AgeI and NotI (FastDigest, Thermo Fisher), and then Gibson Assembly (NEB) was
505 performed with gel-purified PCR product of GFP-CDK5RAP2 (Wu et al., 2016). To generate pB80-FRB-
506 TagBFP-GCN4-ppKin14 and pB80-FRB-HA-GCN4-ppKin14, pB80-FRB-GFP-GCN4-ppKin14-VIb was
507 digested with XbaI and BsrGI (FastDigest, Thermo Fisher), and then TagBFP and HA-tag encoding DNA
508 fragments were subcloned into the linearized vector by Gibson Assembly.

509 To generate the PX459 with single guide RNA (sgRNA) sequences, pSpCas9(BB)-2A-Puro (PX459) V2.0
510 (Ran et al., 2013)(purchased from Addgene) was digested with FastDigest BbsI (Thermo Fisher), and
511 the annealing product of single-strand sgRNA-encoding oligonucleotides was inserted into the linear
512 PX459 linear vector by T4 ligation (Thermo Fisher). The sgRNA sequences that were used in this study
513 are: sgRNA targeting AKAP450 5'- gAGGGTTACCTATGGGACTGA -3'; sgRNA targeting CAMSAP2
514 encoding gene 5'-gCATGATCGATACCCTCATGA-3'; sgRNA targeting p53-encoding gene exon 2 #1 5'-
515 gCGTCGAGCCCCCTCTGAGTC-3'; sgRNA targeting p53 exon 4 #2 5'-gTCCATTGCTTGGGACGGCAA-3';
516 sgRNA targeting p53 exon 4 #3 5'-gCCATTGTTCAATATCGTCCG-3'; sgRNA targeting PCNT exon 5-1 #1
517 5'-gAGACGGCATTGACGGAGCTG-3'; sgRNA targeting pericentrin-encoding gene exon 5-2 #2 5'-
518 GCTCAACAGCCGGCGTGCCC-3'.

519 To generate the GST-DmKHC(1-421)-mNeonGreen construct used for protein purification for motor-
520 PAINT, the fragment containing amino acids 1 to 421 of the Drosophila melanogaster Kinesin Heavy
521 Chain (DmKHC) was amplified from donor construct DmKHC(1-421)-GFP-6x-His with a C-terminal
522 mNeonGreen tag by PCR and then cloned into a pGEX vector. The plasmid was transformed into *E.*
523 *coli* BL21 cells for purification. Bacteria were cultured until OD600 $\approx$0.7 and cultures were cooled
524 prior to inducing protein expression with 0.15 mM IPTG at 18°C overnight. Cells were then pelleted by
525 centrifugation, snap frozen in liquid nitrogen, and stored at -80°C until use. Cells were rapidly thawed
526 at 37°C before being resuspended in chilled lysis buffer (phosphate buffered saline (PBS)
527 supplemented with 5 mM $MgCl_2$, 0.5 mM ATP, 0.1% Tween 20, 250 mM NaCl, and 1x complete
528 protease inhibitor; pH 7.4). Bacteria were lysed by sonication (5 rounds of 30 s) and supplemented
529 with 5 mM DTT and 2mg/mL lysozyme and then incubated on ice for 45 min. The lysate was clarified
530 by centrifuging at 26000 xg for 30 minutes before being incubated with equilibrated Glutathione
531 Sepharose 4B resin for 1.75 hrs. Beads were then pelleted, resuspended in wash buffer (PBS
532 supplemented with 5 mM $MgCl_2$, 0.1% Tween 20, 250 mM NaCl, 1 mM DTT, and 0.5 mM ATP; pH 7.4),
533 and transferred to a BioRad column. Once settled, the resin was washed with 2 x 10 column volumes

534 (CV) wash buffer, followed by 1 x 10CV PreScission buffer (50 mM Tris-HCl, 5 mM $MgCl_2$, 100mM NaCl,
535 1 mM DTT, 0.5 mM ATP; pH 8.0). The resin was then incubated overnight in 4CV PreScission buffer
536 with 80U PreScission protease to cleave off the GST tag. The following morning, after allowing the
537 resin to settle, the eluent was collected, concentrated by spinning through a 3000kDa MWCO filter,
538 supplemented with an additional 0.1mM ATP, 1mM DTT, and 20% w/v sucrose before flash freezing
539 in liquid nitrogen, and finally stored at -80°C. Concentration was determined using a Nanodrop. All
540 steps from lysis onwards were performed at 4°C.

541

542 ***Cell culture and drug treatment***

543 hTERT immortalized RPE-1 (RPE1) cell lines were grown in an 1:1 mix of DMEM and F-10 (Lonza) and
544 Human Embryonic Kidney (HEK) 293T cells line were cultured in DMEM, both supplemented with 10%
545 fetal bovine serum (FBS, GE Healthcare) and 1% penicillin and streptomycin (Sigma-Aldrich). All cells
546 were grown in tissue culture polystyrene flasks (Corning) and were maintained in a humidified
547 incubator at 37°C with 5% CO_2. Mycoplasma contamination was routinely checked with LT07-518
548 Mycoalert assay (Lonza).

549 FuGENE 6 (Promega) was used to transfect RPE1 cells with plasmids for generating CRISPR/Cas9
550 knockouts, immunofluorescence staining and live cell imaging; RNAiMAX (Thermo Fisher Scientific)
551 was used to transfect RPE1 cells with siRNAs at 20 nM; MaxPEI was used to transfect HEK293T cells
552 for lentivirus packaging. Transfections were performed according to the manufacturer's instructions
553 within the recommended reagent/DNA or reagent/siRNA ratio range.

554 We used the following drugs: centrinone B (Tocris Bioscience), nocodazole (Sigma), rapalog (A/C
555 Heterodimerizer, Takara), dynapyrazole A (Sigma-Aldrich) and BI2536 (Selleckchem).

556 To remove centrioles, RPE1 cells were treated with 125 nM centrinone B containing complete medium
557 for ~10 days, and drug-containing medium was refreshed every 24 hrs; cell confluence was maintained
558 around ~50-80% during the treatment.

559 For the microtubule disassembly and regrowth assay, the acentriolar RPE1 cells were seeded onto
560 coverslips in 24-well plates and incubated for 24 hrs, then cells were treated with 10 µM nocodazole
561 for 1 hr in an incubator (37°C, 5% CO_2) and followed by another 1 hr treatment at 4°C to achieve
562 complete disassembly of stable microtubule fragments. Nocodazole washout was then carried out by
563 at least six washes on ice with ice-cold complete medium; subsequently, plates were moved to a 37°C
564 water bath and pre-warmed medium was added to each well to allow microtubule regrowth.

565 For the inducible ppKin14-CAMSAP2 heterodimerization experiment, acentriolar cells were seeded
566 onto coverslips in 24-well plates, cultured with centrinone B containing medium and co-transfected
567 with 2FKBP-mCherry-CAMSAP2 and FRB-TagBFP-GCN4-ppKin14 vectors. 24 hrs after transfection,
568 rapalog was added into the medium at a final concentration of 50 nM and incubated overnight for
569 preparation of fixed cells. For live imaging, rapalog was used at 100 nM.

570

571 ***Lentivirus packaging and generation of transgenic stable cell lines***

572 Lentiviruses were produced by MaxPEI-based co-transfection of HEK293T cells with the transfer
573 vectors together with the packaging vector psPAX2 and envelope vector pMD2.G (psPAX2 and
574 pMD2.G were a gift from Didier Trono, Addgene plasmid #12259 and #12260; RRID:Addgene_12259
575 and RRID:Addgene_12260). Supernatant of packaging cells was harvested 48-72 hrs after transfection,
576 filtered through a 0.45 µm filter, incubated with a polyethylene glycol (PEG)-6000-based precipitation
577 solution overnight at 4°C and centrifuged for 30 minutes at 1500 rpm to concentrate the virus.
578 Lentiviral pellet was resuspended in PBS.

579 Wild type, AKAP450 and AKAP450/CAMSAP2 knockout RPE1 cells were infected with lentivirus and
580 incubated in complete medium supplemented with 8 µg/ml polybrene (Sigma-Aldrich). After 24 hrs,
581 the cell medium was replaced with fresh medium. Starting 72 hrs after viral transduction, cells were
582 subjected to selection with puromycin at a concentration of 25 µg/ml for wild-type, 20 µg/ml for
583 AKAP450 knockout and 15 µg/ml for AKAP450/CASMAP2 knockout for up to 3 days (until most of the
584 untransduced control cells, treated with the same concentration of antibiotic, were dead). After
585 selection, cells were grown in normal medium for 3 days and individual colonies expressing GFP were
586 isolated into 96-well plates by fluorescence-activated cell sorting (FACS). Sorted single transgenic
587 stable cell lines were further confirmed by immunofluorescence staining to check the expression level
588 of GFP-CDK5RAP2 and its colocalization with other centrosomal proteins.

589

590 ***Generation of CRIPSR/Cas9 knockout cell lines***

591 The CRISPR/Cas9-mediated knockout of p53-, pericentrin-, AKAP450- and CAMSAP2-encoding genes
592 was performed as described previously (Ran et al., 2013). In brief, AKAP450/CAMSAP2 knockout RPE1
593 cells (Wu et al., 2016) were transfected with the vectors bearing the appropriate targeting sequences
594 using FuGENE 6. One day after transfection, the transfected AKAP450/CAMSAP2 knockout RPE1 cells
595 were subjected to selection with 15 µg/ml puromycin for up to 3 days. After selection, cells were
596 allowed to recover in normal medium for ∼7 days, and knockout efficiency was checked by

597 immunofluorescence staining. Depending on the efficiency, 50–500 individual clones were isolated
598 and confirmed by immunofluorescence staining, and the resulted single colonies were characterized
599 by Western blotting, immunostaining and genome sequencing. AKAP450/CAMSAP2/p53 and
600 AKAP450/CAMSAP2/MMG/CDK5RAP2/p53 knockout cell lines were generated first and subsequently,
601 each of them was used to knock out the gene encoding pericentrin. The mutated portions of the p53-
602 and pericentrin-encoding genes were sequenced using gel-purified PCR products obtained with
603 primers located in the vicinity of the corresponding sgRNA targeting sites.

604

605 ***Antibodies, immunofluorescence staining and Western blotting***

606 Antibodies used for immunostaining and Western blotting are listed in the Key Reagent or Resource
607 table. For immunofluorescence cell staining, cultured cells were fixed with –20°C methanol for 5 min
608 or with 4% paraformaldehyde (PFA) for 12 min at room temperature, rinsed in PBS for 5 min,
609 permeabilized with 0.15% Triton X-100 in PBS for 2 min, washed 3 times for 5 min with 0.05% Tween-
610 20 in PBS, sequentially incubated for 20 min in the blocking buffer (2% BSA and 0.05% Tween-20 in
611 PBS), 1 hr with primary antibodies in the blocking buffer, washed 3 times for 5 min with 0.05% Tween-
612 20 in PBS, then for 1 hr in secondary antibodies in the blocking buffer, washed 3 times for 5 min with
613 0.05% Tween-20 in PBS, and air-dried after a quick wash in 96% ethanol. Cells were mounted in
614 Vectashield mounting medium with or without DAPI (Vector laboratories, Burlingame, CA). Alexa Fluor
615 -405, -488, –594 and −647 conjugated goat antibodies against rabbit, rat and mouse IgG were used as
616 secondary antibodies (Molecular Probes, Eugene, OR).

617 For Western blotting, cells were harvested from six-well plates or 10 cm dishes at 90% confluence and
618 protein extracts were prepared using the lysis buffer containing 20 mM Tris-Cl, pH 7.5, 150 mM NaCl,
619 0.5 mM EDTA, 1 mM DTT, 1% Triton X-100 or RIPA buffer containing 50 mM Tris-HCl, pH 7.5, 150 mM
620 NaCl, 1% Triton X-100, 0.5% Sodium Deoxycholate supplemented with protease inhibitor and
621 phosphatase inhibitors (Roche). Samples were run on polyacrylamide gels, followed by transfer on
622 0.45 µm nitrocellulose membrane (Sigma-Aldrich). Blocking was performed in 2% BSA in PBS for 30
623 min at room temperature. The membrane was first incubated with the primary antibodies overnight
624 at 4°C and washed with 0.05% Tween-20 in PBS 3 times and subsequently incubated with secondary
625 antibodies for 1 hr at room temperature and washed 3 times with 0.05% Tween-20 in PBS. IRDye
626 800CW/680 LT Goat anti-rabbit and anti-mouse were used as secondary antibodies (Li-Cor
627 Biosciences, Lincoln, LE) and membranes were imaged on Odyssey CLx infrared imaging system (Image
628 Studio version 5.2.5, Li-Cor Biosciences).

629

630 ***Imaging and analysis of fixed cells***

631 Images of fixed cells were collected with a Nikon Eclipse Ni upright fluorescence microscope equipped
632 with a DS-Qi2 CMOS camera (Nikon), an Intensilight C-HGFI epi-fluorescence illuminator (Nikon), Plan
633 Apo Lambda 100× NA 1.45 or Plan Apo Lambda 60x N.A. 1.40 oil objectives (Nikon) and driven by NIS-
634 Elements Br software (Nikon).

635 Gated STED imaging was performed with Leica TCS SP8 STED 3X microscope driven by LAS X software
636 using HC PL APO 100x/1.4 oil STED WHITE objective, white laser (633 nm) for excitation and 775 nm
637 pulsed lased for depletion. Images were acquired in 2D STED mode with vortex phase mask. Depletion
638 laser power was equal to 90% of maximum power and an internal Leica HyD hybrid detector with a
639 time gate of $1 \leqslant tg \leqslant 8$ ns was used.

640 ImageJ was used for adjustments of intensity levels and contrast, quantification of the
641 immunofluorescence signal intensity and maximum intensity projections. To analyze PCM clustering
642 after nocodazole washout in AKAP450/CAMSAP2 knockout RPE1 cells, images were separated into
643 concentric circular areas using Concentric Circles plugin of ImageJ. The biggest PCM cluster (which
644 normally also had the highest fluorescence intensity) was selected as the center, around which 20
645 circles with 2 µm inner radius and 20 µm outer radius were drawn. Fluorescence intensity of PCM
646 clusters in these concentric circles was measured automatically and normalized by the sum of the total
647 PCM intensity in each cell per condition. To quantify the areas occupied by PCM clusters,
648 immunofluorescence images of fixed cells and time lapse images of live cells were analyzed by drawing
649 the smallest circle that covered visible PCM clusters to indicate the area occupied by the PCM clusters,
650 and the diameters of the circles were used for the quantification.

651

652 ***Measurements of microtubule radiality***

653 To analyze microtubule radiality, images of fluorescently labeled microtubules were separated into
654 radial and non-radial components using a customized ImageJ macro
655 (https://github.com/ekatrukha/radialitymap). First, a local orientation angle map was calculated for
656 each pixel using the OrientationJ plugin. We used 'cubic spline gradient' method and tensor sigma
657 parameter of 6 pixels (0.4 µm). The new origin of coordinates was specified by selecting the
658 centrosome position in the corresponding channel, or the brightest spot in case of centrinone
659 treatment. Radial local orientation angle was calculated as a difference between the local orientation
660 angle and the angle of the vector drawn from the new origin of coordinates to the current pixel

661 position. A radial map image was calculated as an absolute value of the cosine of the radial local
662 orientation angle at each pixel providing values between zero and one. A non-radial map image was
663 calculated as one minus the radial map. Both maps were multiplied with the original image to account
664 for different signal intensities; the two maps illustrate separated radial and non-radial image
665 components.

666

667 ***Live cell imaging and analysis***

668 Live fluorescent imaging was performed with spinning disk confocal microscopy on inverted research
669 microscope Nikon EclipseTi-E (Nikon), equipped with the Perfect Focus System (Nikon), Nikon Plan
670 Apo VC 60x NA 1.4 and Nikon Plan Apo VC 100x N.A. 1.40 oil objectives (Nikon) and spinning-disc
671 confocal scanner unit (CSU-X1-A1, Yokogawa). The system was also equipped with ASI motorized stage
672 with the piezo top plate MS-2000-XYZ (ASI), Photometrics Evolve 512 EMCCD camera (Photometrics)
673 and controlled by the MetaMorph 7.8 software (Molecular Devices). Vortran Stradus lasers (405 nm
674 100 mW, 488 nm 150 mW and 642 nm 165 mW) and Cobolt Jive 561 nm 110 mW laser were used as
675 the light sources. System was equipped with ET-DAPI (49000), ET-GFP (49002), ET-mCherry (49008)
676 and ET-Cy5 (49006) filter sets (Chroma). 16-bit images were projected onto the EMCCD chip with the
677 intermediate lens 2.0X (Edmund Optics) at a magnification of 110 nm per pixel (60x objective) and 67
678 nm per pixel (100x objective). To keep cells at 37°C and 5% CO_2 we used stage top incubator (INUBG2E-
679 ZILCS, Tokai Hit). Cells were plated on round 25 mm coverslips, which were mounted in Attofluor Cell
680 Chamber (Thermo fisher). Cells were imaged with a 2 s interval and 200 ms exposure for 1-3 hrs at
681 10% laser power.

682 For live imaging of nocodazole treatment and washout experiments, cells were incubated with the
683 medium containing 100 nM SiR-tubulin (Tebu-bio) overnight to image the microtubule network.
684 Centrinone B-treated cells were imaged for a desired period of time prior to the nocodazole
685 treatment, and then nocodazole was added into the medium at a final concentration of 10 µM while
686 imaging simultaneously. Culture medium was carefully removed when microtubules were completely
687 depolymerized and washed with prewarmed medium six times to let microtubules regrow. GFP-
688 CDK5RAP2 and SiR-tubulin imaging was performed with a 2 s interval with 200 ms exposure for 1-3
689 hrs in total, and maximum intensity projections, contrast adjustment and further processing was
690 performed using ImageJ.

691

692 ***FRAP***

693 FRAP experiments were performed on the spinning disc microscope describe above, equipped with
694 iLas platform and using Targeted Laser Action options of iLas and controlled with iLas software (Roper
695 Scientific, now Gataca Systems). Photobleaching in the GFP channel was performed with the 488 nm
696 laser. For the FRAP analysis, Polygon ROIs were set in photobleached and non-bleached regions as
697 well as in the background. The average fluorescence intensity was measured using ImageJ for each
698 frame, the background intensity was subtracted from the bleached and non-bleached areas and
699 normalized to the average of the frames acquired prior to the bleach. The mean fluorescence
700 intensities of the images before photobleaching were set as 100%, and the subsequent relative
701 recovery percentages were calculated. Time lapse acquisitions were corrected for drift with the
702 ImageJ plugins Template Matching.

703

704 ***motor-PAINT and analysis***

705 For motor-PAINT, a protocol published previously (Tas et al., 2017) was used, with minor adjustments.
706 Cells were incubated with 50 nM SiR-tubulin and 500 nM verapamil overnight to allow fields of view
707 suitable for imaging to be located before the addition of purified GST-DmKHC(1-421)-mNeonGreen.
708 For nocodazole-treated samples, cells were first incubated with 10 µM nocodazole for 15 minutes at
709 37°C. A single nocodazole-treated or control sample was then transferred to an imaging chamber, and
710 cells were subjected to extraction for 1 minute in extraction buffer (BRB80: 80 mM K-Pipes, 1 mM
711 $MgCl_2$, 1 mM EGTA; pH 6.8, supplemented with 1M sucrose and 0.15% TritonX-100) pre-warmed to
712 37°C. Pre-warmed fixation buffer (BRB80 supplemented with 2% PFA) was added to this (i.e. final PFA
713 concentration of 1%) and the solutions were mixed by gentle pipetting for 1 minute. This buffer was
714 removed and the chamber was washed for 4 times for 1 minute in pre-warmed wash buffer (BRB80
715 supplemented with 1 µM Taxol) before adding imaging buffer (BRB80 supplemented with 583 µg/mL
716 catalase, 42 µg/mL glucose oxidase, 1.7% w/v glucose, 1 mM DTT, 1 µM Taxol, and 5mM ATP). An
717 aliquot of GST-DmKHC(1-421)-mNeonGreen motors was warmed, spun in the Airfuge at 20 psi for 5
718 minutes in a pre-chilled rotor to remove any aggregates, and then transferred to a clean tube prior to
719 use. Motors were kept on ice and added locally to cells in 0.3 µl increments.

720 Imaging was performed immediately after sample preparation at room temperature on a Nikon Ti-E
721 microscope equipped with a 100x Apo TIRF oil immersion objective (NA. 1.49) and Perfect Focus
722 System 3 (Nikon). Excitation was achieved with a Lighthub-6 laser combiner (Omicron) containing a
723 647 nm laser (LuxX 140 mW, Omicron), a 488 nm laser (LuxX 200 mW, Omicron), and optics allowing
724 for a tunable angle of incidence. Illumination was adjusted for (pseudo-) total internal reflection
725 fluorescence (TIRF) microscopy. Emission light was separated from excitation light using a quad-band

726 polychroic mirror (ZT405/488/561/640rpc, Chroma), a quad-band emission filter
727 (ZET405/488/561/640m, Chroma), and an additional single-band emission filter (ET525/50m for
728 mNeonGreen emission, Chroma). Detection was achieved using a Hamamatsu Flash 4.0v2 sCMOS
729 camera. Image stacks were acquired with a 60 ms exposure time, 7% laser power, and 15000-22000
730 images per field of view. Components were controlled using MicroManager (Edelstein et al., 2014).

731 Acquired stacks were pre-processed using the Faster Temporal Median ImageJ plugin
732 (https://github.com/HohlbeinLab/FTM2; (Jabermoradi et al., 2021)) with a window size of 100 frames.
733 These stacks were then analyzed using Detection of Molecules (DoM) plugin v.1.2.1 for ImageJ
734 (https://github.com/ekatrukha/DoM_Utrecht), as has been described previously (Chazeau et al.,
735 2016; Tas et al., 2017). Each image in an acquired stack is convoluted with a two-dimensional Mexican
736 hat kernel. The resulting intensity histogram is used to create a thresholded mask based on a cut-off
737 of three standard deviations above the mean. This mask is then subject to rounds of dilution and
738 erosion to create a filtered mask used to calculate the centroids on the original image. These centroids
739 are used as initial values to perform unweighted nonlinear least squares fitting with a Levenberg-
740 Marquardt algorithm to an asymmetric two-dimensional Gaussian point spread function (PSF),
741 allowing for the sub-pixel localization of particles.

742 Images were drift-corrected using DoM. The normalized cross-correlation between intermediate
743 reconstructions of consecutive sub-stacks is used to calculate the drift in x and y between sub-stacks,
744 which is then linearly interpolated to adjust each individual frame in the stack.

745 Detected particles were linked into tracks again using DoM, which performs a quicker variant of a
746 nearest neighbor search, with a maximum distance of 5 pixels (~320nm) between consecutive frames
747 and no permitted frame gap. Tracks were later filtered to remove those shorter than 4 frames or
748 longer than 200 frames, those in which an angle between parts of the trajectory exceeded 90 degrees,
749 and those in which the speed of the motor was less than 100nm/s or more than 1500nm/s.

750 The particle table was then split into four particle tables corresponding to the four quadrants of the
751 image with tracks sorted based on their net displacement (i.e., $\Delta x>0 \wedge \Delta y>0$; $\Delta x>0 \wedge \Delta y<0$; Δ
752 $x<0 \wedge \Delta y>0$; $\Delta x<0 \wedge \Delta y<0$), as described previously (Tas et al., 2017). These directionality-filtered
753 particle tables were reconstructed using DoM, creating four super-resolved images of microtubule
754 segments pointing in a similar direction. These were merged with the reconstructed image of all
755 localizations to determine the direction of each microtubule segment. Each microtubule was manually
756 assessed to assign it as being plus-end-in or plus-end-out. Microtubules were manually traced with
757 lines 4 pixels (80 nm) wide, assigned a color based on their orientation, flattened onto the image,

758 filtered with a Gaussian Blur of radius 2, and finally merged with the reconstructed image of all
759 localizations.

760 To quantify the percentage of minus-end-out microtubule length to total microtubule length before
761 and after nocodazole treatment, the length of each microtubule (determined from kinesin-1
762 trajectories) in the cell was measured by calculating the Euclidean distance between all subsequent
763 pairs of points along the microtubule and summed. The ratio was calculated as the total minus-end-
764 out microtubule length divided by the total microtubule length.

765

766 ***Analysis of PCM cluster dynamics***

767 To represent the motion of PCM clusters during nocodazole treatment, ImageJ plugin
768 KymoResliceWide v.0.4 (https://github.com/ekatrukha/KymoResliceWide) was used for generating
769 kymographs from the time lapse images. The velocity of PCM clusters was measured manually using
770 kymographs starting from the time point when a small PCM cluster moved out of an aMTOC.
771 Microtubule density around each PCM cluster was determined by measuring the mean fluorescence
772 intensity of SiR-tubulin in a circular area with a 2 µm radius centered on the PCM cluster and
773 normalizing it to the mean fluorescence intensity of 20 images prior to nocodazole addition (set as
774 100%). The moment when a PCM cluster started to move out of the aMTOC was set as the initial time
775 point (0 min), and the subsequent PCM cluster motion velocity and the relative local microtubule
776 density at 43 time points were calculated and averaged.

777 The movement trajectories of PCM clusters were generated using ImageJ plugin TrackMate (version
778 is 6.0.2). The parameters and the settings used were as following: LoG (Laplacian of Gaussian) detector
779 with estimated blob diameter: 14.9 µm; thresholding value 12.25; sub-pixel localization was selected.
780 HyperStack Displayer was selected to overlay the spots and tracks on the current hyperstack window.
781 Simple LAP tracker was selected to track the distance and time with the linking max distance: 32.0 µm,
782 gap-closing max distance: 55.0 µm and gap-closing max frame gap: 2. All other parameters and
783 settings were used as the default.

784

785 ***Statistical analysis***

786 All statistical analyses were performed using GraphPad Prism 9. Statistical details for each experiment
787 can be found in the corresponding figure legends and supporting files.

788

789 ***Data and software availability***

790 All mentioned ImageJ plugins have source code available and are licensed under open-source GNU
791 GPL v3 license. The source data for the original Western blots are available within the paper.

792

793 **Acknowledgements**

794 We thank Lynne Cassimeris (Lehigh University, USA), Pierre Gönczy and Didier Trono (EPFL,
795 Switzerland), Dr. Duane Compton (Geisel School of Medicine at Dartmouth, USA) and Dr. Laurence
796 Pelletier (Lunenfeld-Tanenbaum Research Institute, Canada) for the gift of materials and Ilya Grigoriev
797 and Eugene Katrukha (Biology Imaging Center, Utrecht University) for the help with imaging and image
798 analysis. This work was supported by China Scholarship Council scholarships to Fangrui Chen, Jingchao
799 Wu and Chao Yang, the Netherlands Organization for Scientific Research Spinoza prize to A.A, as well
800 as the European Research Council Consolidator Grant 819219 to L.C.K. and the Eindhoven-
801 Wageningen-Utrecht Alliance (www.ewuu.nl) that supports the Center for Living Technologies.

802

803 **Competing financial interests**

804 The authors declare no competing financial interests.

805

806 **References**

807 Abal, M., M. Piel, V. Bouckson-Castaing, M. Mogensen, J.B. Sibarita, and M. Bornens. 2002.
808 Microtubule release from the centrosome in migrating cells. *J Cell Biol*. 159:731-737.

809 Akhmanova, A., C.C. Hoogenraad, K. Drabek, T. Stepanova, B. Dortland, T. Verkerk, W. Vermeulen,
810 B.M. Burgering, C.I. De Zeeuw, F. Grosveld, and N. Galjart. 2001. Clasps are CLIP-115 and -
811 170 associating proteins involved in the regional regulation of microtubule dynamics in
812 motile fibroblasts. *Cell*. 104:923-935.

813 Balczon, R., C.E. Varden, and T.A. Schroer. 1999. Role for microtubules in centrosome doubling in
814 Chinese hamster ovary cells. *Cell Motil Cytoskeleton*. 42:60-72.

815 Balestra, F.R., A. Dominguez-Calvo, B. Wolf, C. Busso, A. Buff, T. Averink, M. Lipsanen-Nyman, P.
816 Huertas, R.M. Rios, and P. Gonczy. 2021. TRIM37 prevents formation of centriolar protein
817 assemblies by regulating Centrobin. *Elife*. 10:e62640.

818 Burakov, A., O. Kovalenko, I. Semenova, O. Zhapparova, E. Nadezhdina, and V. Rodionov. 2008.
819 Cytoplasmic dynein is involved in the retention of microtubules at the centrosome in
820 interphase cells. *Traffic*. 9:472-480.

821 Cassimeris, L., and J. Morabito. 2004. TOGp, the human homolog of XMAP215/Dis1, is required for
822 centrosome integrity, spindle pole organization, and bipolar spindle assembly. *Mol Biol Cell*.
823 15:1580-1590.

824 Charrasse, S., M. Schroeder, C. Gauthier-Rouviere, F. Ango, L. Cassimeris, D.L. Gard, and C. Larroque.
825 1998. The TOGp protein is a new human microtubule-associated protein homologous to the
826 Xenopus XMAP215. *J Cell Sci*. 111 (Pt 10):1371-1383.

827 Chazeau, A., E.A. Katrukha, C.C. Hoogenraad, and L.C. Kapitein. 2016. Studying neuronal microtubule
828 organization and microtubule-associated proteins using single molecule localization
829 microscopy. *Methods Cell Biol*. 131:127-149.

830 Chen, C.T., H. Hehnly, Q. Yu, D. Farkas, G. Zheng, S.D. Redick, H.F. Hung, R. Samtani, A. Jurczyk, S.
831 Akbarian, C. Wise, A. Jackson, M. Bober, Y. Guo, C. Lo, and S. Doxsey. 2014. A unique set of
832 centrosome proteins requires pericentrin for spindle-pole localization and spindle
833 orientation. *Curr Biol*. 24:2327-2334.

834 Chi, W., G. Wang, G. Xin, Q. Jiang, and C. Zhang. 2021. PLK4-phosphorylated NEDD1 facilitates
835 cartwheel assembly and centriole biogenesis initiations. *J Cell Biol*. 220:e202002151.

836 Chinen, T., S. Yamamoto, Y. Takeda, K. Watanabe, K. Kuroki, K. Hashimoto, D. Takao, and D.
837 Kitagawa. 2020. NuMA assemblies organize microtubule asters to establish spindle bipolarity
838 in acentrosomal human cells. *EMBO J*. 39:e102378.

839 Chinen, T., K. Yamazaki, K. Hashimoto, K. Fujii, K. Watanabe, Y. Takeda, S. Yamamoto, Y. Nozaki, Y.
840 Tsuchiya, D. Takao, and D. Kitagawa. 2021. Centriole and PCM cooperatively recruit CEP192
841 to spindle poles to promote bipolar spindle assembly. *J Cell Biol*. 220:e202006085.

842 Choi, Y.K., P. Liu, S.K. Sze, C. Dai, and R.Z. Qi. 2010. CDK5RAP2 stimulates microtubule nucleation by
843 the gamma-tubulin ring complex. *J Cell Biol*. 191:1089-1095.

844 Chong, W.M., W.J. Wang, C.H. Lo, T.Y. Chiu, T.J. Chang, Y.P. Liu, B. Tanos, G. Mazo, M.B. Tsou, W.N.
845 Jane, T.T. Yang, and J.C. Liao. 2020. Super-resolution microscopy reveals coupling between
846 mammalian centriole subdistal appendages and distal appendages. *Elife*. 9:e53580.

847 Cizmecioglu, O., M. Arnold, R. Bahtz, F. Settele, L. Ehret, U. Haselmann-Weiss, C. Antony, and I.
848 Hoffmann. 2010. Cep152 acts as a scaffold for recruitment of Plk4 and CPAP to the
849 centrosome. *Journal of Cell Biology*. 191:731-739.

850 Conduit, P.T., A. Wainman, and J.W. Raff. 2015. Centrosome function and assembly in animal cells.
851 *Nat Rev Mol Cell Biol*. 16:611-624.

852 Delaval, B., and S.J. Doxsey. 2010. Pericentrin in cellular function and disease. *J Cell Biol*. 188:181-
853 190.

854 Delgehyr, N., J. Sillibourne, and M. Bornens. 2005. Microtubule nucleation and anchoring at the
855 centrosome are independent processes linked by ninein function. *J Cell Sci*. 118:1565-1575.

856 Edelstein, A.D., M.A. Tsuchida, N. Amodaj, H. Pinkard, R.D. Vale, and N. Stuurman. 2014. Advanced
857 methods of microscope control using muManager software. *J Biol Methods*. 1:e10.

858 Efimov, A., A. Kharitonov, N. Efimova, J. Loncarek, P.M. Miller, N. Andreyeva, P. Gleeson, N. Galjart,
859 A.R. Maia, I.X. McLeod, J.R. Yates, 3rd, H. Maiato, A. Khodjakov, A. Akhmanova, and I.
860 Kaverina. 2007. Asymmetric CLASP-dependent nucleation of noncentrosomal microtubules
861 at the trans-Golgi network. *Dev Cell*. 12:917-930.

862 Fong, C.S., G. Mazo, T. Das, J. Goodman, M. Kim, B.P. O'Rourke, D. Izquierdo, and M.F. Tsou. 2016.
863 53BP1 and USP28 mediate p53-dependent cell cycle arrest in response to centrosome loss
864 and prolonged mitosis. *Elife*. 5:e16270.

865 Fong, K.W., Y.K. Choi, J.B. Rattner, and R.Z. Qi. 2008. CDK5RAP2 is a pericentriolar protein that
866 functions in centrosomal attachment of the gamma-tubulin ring complex. *Mol Biol Cell*.
867 19:115-125.

868 Fu, J.Y., and D.M. Glover. 2012. Structured illumination of the interface between centriole and peri-
869 centriolar material. *Open Biology*. 2:120104.

870 Fu, M.M., T.S. McAlear, H. Nguyen, J.A. Oses-Prieto, A. Valenzuela, R.D. Shi, J.J. Perrino, T.T. Huang,
871 A.L. Burlingame, S. Bechstedt, and B.A. Barres. 2019. The Golgi Outpost Protein TPPP
872 Nucleates Microtubules and Is Critical for Myelination. *Cell*. 179:132-146.

873 Ganem, N.J., and D.A. Compton. 2004. The KinI kinesin Kif2a is required for bipolar spindle assembly
874 through a functional relationship with MCAK. *J Cell Biol*. 166:473-478.

875 Ganem, N.J., K. Upton, and D.A. Compton. 2005. Efficient mitosis in human cells lacking poleward
876 microtubule flux. *Curr Biol*. 15:1827-1832.

877 Garbrecht, J., T. Laos, E. Holzer, M. Dillinger, and A. Dammermann. 2021. An acentriolar centrosome
878 at the C. elegans ciliary base. *Curr Biol*. 31:2418-2428.

879 Gartenmann, L., C.C. Vicente, A. Wainman, Z.A. Novak, B. Sieber, J.H. Richens, and J.W. Raff. 2020.
880 Drosophila Sas-6, Ana2 and Sas-4 self-organise into macromolecular structures that can be
881 used to probe centriole and centrosome assembly. *J Cell Sci*. 133:jcs244574.

882 Gavilan, M.P., P. Gandolfo, F.R. Balestra, F. Arias, M. Bornens, and R.M. Rios. 2018. The dual role of
883 the centrosome in organizing the microtubule network in interphase. *EMBO Rep*. 19:e45942.

884 Gimpel, P., Y.L. Lee, R.M. Sobota, A. Calvi, V. Koullourou, R. Patel, K. Mamchaoui, F. Nedelec, S.
885 Shackleton, J. Schmoranzer, B. Burke, B. Cadot, and E.R. Gomes. 2017. Nesprin-1alpha-
886 Dependent Microtubule Nucleation from the Nuclear Envelope via Akap450 Is Necessary for
887 Nuclear Positioning in Muscle Cells. *Curr Biol*. 27:2999-3009.

888 Goldspink, D.A., C. Rookyard, B.J. Tyrrell, J. Gadsby, J. Perkins, E.K. Lund, N. Galjart, P. Thomas, T.
889 Wileman, and M.M. Mogensen. 2017. Ninein is essential for apico-basal microtubule

890 formation and CLIP-170 facilitates its redeployment to non-centrosomal microtubule
891 organizing centres. *Open Biol*. 7:160274.

892 Gomez-Ferreria, M.A., M. Bashkurov, A.O. Helbig, B. Larsen, T. Pawson, A.C. Gingras, and L. Pelletier.
893 2012. Novel NEDD1 phosphorylation sites regulate gamma-tubulin binding and mitotic
894 spindle assembly. *J Cell Sci*. 125:3745-3751.

895 Gomez-Ferreria, M.A., U. Rath, D.W. Buster, S.K. Chanda, J.S. Caldwell, D.R. Rines, and D.J. Sharp.
896 2007. Human Cep192 is required for mitotic centrosome and spindle assembly. *Curr Biol*.
897 17:1960-1966.

898 Grigoriev, I., S.M. Gouveia, B. van der Vaart, J. Demmers, J.T. Smyth, S. Honnappa, D. Splinter, M.O.
899 Steinmetz, J.W. Putney, Jr., C.C. Hoogenraad, and A. Akhmanova. 2008. STIM1 is a MT-plus-
900 end-tracking protein involved in remodeling of the ER. *Curr Biol*. 18:177-182.

901 Haren, L., M.H. Remy, I. Bazin, I. Callebaut, M. Wright, and A. Merdes. 2006. NEDD1-dependent
902 recruitment of the gamma-tubulin ring complex to the centrosome is necessary for centriole
903 duplication and spindle assembly. *J Cell Biol*. 172:505-515.

904 Haren, L., T. Stearns, and J. Luders. 2009. Plk1-dependent recruitment of gamma-tubulin complexes
905 to mitotic centrosomes involves multiple PCM components. *PLoS One*. 4:e5976.

906 Hoogenraad, C.C., P. Wulf, N. Schiefermeier, T. Stepanova, N. Galjart, J.V. Small, F. Grosveld, C.I. de
907 Zeeuw, and A. Akhmanova. 2003. Bicaudal D induces selective dynein-mediated microtubule
908 minus end-directed transport. *Embo J*. 22:6004-6015.

909 Jabermoradi, A., S. Yang, M. Gobes, J.P.M. van Duynhoven, and H. J. 2021. Enabling single-molecule
910 localization microscopy in turbid food emulsions. *bioRxiv*:2021.2003.2003.433739.

911 Jia, Y., K.W. Fong, Y.K. Choi, S.S. See, and R.Z. Qi. 2013. Dynamic recruitment of CDK5RAP2 to
912 centrosomes requires its association with dynein. *PLoS One*. 8:e68523.

913 Jiang, K., S. Hua, R. Mohan, I. Grigoriev, K.W. Yau, Q. Liu, E.A. Katrukha, A.F. Altelaar, A.J. Heck, C.C.
914 Hoogenraad, and A. Akhmanova. 2014. Microtubule minus-end stabilization by
915 polymerization-driven CAMSAP deposition. *Dev Cell*. 28:295-309.

916 Jiang, X., D. Bang Tam Ho, K. Mahe, J. Mia, G. Sepulveda, M. Antkowiak, L. Jiang, S. Yamada, and L.-E.
917 Jao. 2020. Condensation of pericentrin proteins in human cells illuminates phase separation
918 in centrosome assembly. *bioRxiv*:2020.2005.2008.084749.

919 Jonsson, E., M. Yamada, R.D. Vale, and G. Goshima. 2015. Clustering of a kinesin-14 motor enables
920 processive retrograde microtubule-based transport in plants. *Nat Plants*. 1:15087.

921 Joukov, V., J.C. Walter, and A. De Nicolo. 2014. The Cep192-organized aurora A-Plk1 cascade is
922 essential for centrosome cycle and bipolar spindle assembly. *Mol Cell*. 55:578-591.

923 Khanal, I., A. Elbediwy, C. Diaz de la Loza Mdel, G.C. Fletcher, and B.J. Thompson. 2016. Shot and
924 Patronin polarise microtubules to direct membrane traffic and biogenesis of microvilli in
925 epithelia. *J Cell Sci*. 129:2651-2659.

926 Khodjakov, A., R.W. Cole, B.R. Oakley, and C.L. Rieder. 2000. Centrosome-independent mitotic
927 spindle formation in vertebrates. *Curr Biol*. 10:59-67.

928 Kim, S., and K. Rhee. 2014. Importance of the CEP215-pericentrin interaction for centrosome
929 maturation during mitosis. *PLoS One*. 9:e87016.

930 Kim, T.S., J.E. Park, A. Shukla, S. Choi, R.N. Murugan, J.H. Lee, M. Ahn, K. Rhee, J.K. Bang, B.Y. Kim, J.
931 Loncarek, R.L. Erikson, and K.S. Lee. 2013. Hierarchical recruitment of Plk4 and regulation of

932 centriole biogenesis by two centrosomal scaffolds, Cep192 and Cep152. *Proc Natl Acad Sci U*
933 *S A*. 110:E4849-4857.

934 Kohlmaier, G., J. Loncarek, X. Meng, B.F. McEwen, M.M. Mogensen, A. Spektor, B.D. Dynlacht, A.
935 Khodjakov, and P. Gonczy. 2009. Overly Lona Centrioles and Defective Cell Division upon
936 Excess of the SAS-4-Related Protein CPAP. *Current Biology*. 19:1012-1018.

937 Kolano, A., S. Brunet, A.D. Silk, D.W. Cleveland, and M.H. Verlhac. 2012. Error-prone mammalian
938 female meiosis from silencing the spindle assembly checkpoint without normal
939 interkinetochore tension. *Proc Natl Acad Sci U S A*. 109:E1858-1867.

940 Komarova, Y., G. Lansbergen, N. Galjart, F. Grosveld, G.G. Borisy, and A. Akhmanova. 2005. EB1 and
941 EB3 control CLIP dissociation from the ends of growing microtubules. *Mol Biol Cell*. 16:5334-
942 5345.

943 Lambrus, B.G., V. Daggubati, Y. Uetake, P.M. Scott, K.M. Clutario, G. Sluder, and A.J. Holland. 2016. A
944 USP28-53BP1-p53-p21 signaling axis arrests growth after centrosome loss or prolonged
945 mitosis. *J Cell Biol*. 214:143-153.

946 Lansbergen, G., Y. Komarova, M. Modesti, C. Wyman, C.C. Hoogenraad, H.V. Goodson, R.P. Lemaitre,
947 D.N. Drechsel, E. van Munster, T.W.J. Gadella Jr., F. Grosveld, N. Galjart, G.G. Borisy, and A.
948 Akhmanova. 2004. Conformational changes in CLIP-170 regulate its binding to microtubules
949 and dynactin localisation. *J Cell Biol*. 166:1003-1014.

950 Lawo, S., M. Bashkurov, M. Mullin, M.G. Ferreria, R. Kittler, B. Habermann, A. Tagliaferro, I. Poser,
951 J.R. Hutchins, B. Hegemann, D. Pinchev, F. Buchholz, J.M. Peters, A.A. Hyman, A.C. Gingras,
952 and L. Pelletier. 2009. HAUS, the 8-subunit human Augmin complex, regulates centrosome
953 and spindle integrity. *Curr Biol*. 19:816-826.

954 Lawo, S., M. Hasegan, G.D. Gupta, and L. Pelletier. 2012. Subdiffraction imaging of centrosomes
955 reveals higher-order organizational features of pericentriolar material. *Nat Cell Biol*.
956 14:1148-1158.

957 Lechler, T., and E. Fuchs. 2007. Desmoplakin: an unexpected regulator of microtubule organization in
958 the epidermis. *J Cell Biol*. 176:147-154.

959 Lee, K., and K. Rhee. 2011. PLK1 phosphorylation of pericentrin initiates centrosome maturation at
960 the onset of mitosis. *J Cell Biol*. 195:1093-1101.

961 Lee, S., and K. Rhee. 2010. CEP215 is involved in the dynein-dependent accumulation of
962 pericentriolar matrix proteins for spindle pole formation. *Cell Cycle*. 9:774-783.

963 Liang, X., M. Kokes, R.D. Fetter, M.D. Sallee, A.W. Moore, J.L. Feldman, and K. Shen. 2020. Growth
964 cone-localized microtubule organizing center establishes microtubule orientation in
965 dendrites. *Elife*. 9:e56547.

966 Lin, Y.N., C.T. Wu, Y.C. Lin, W.B. Hsu, C.J. Tang, C.W. Chang, and T.K. Tang. 2013. CEP120 interacts
967 with CPAP and positively regulates centriole elongation. *J Cell Biol*. 202:211-219.

968 Luders, J., U.K. Patel, and T. Stearns. 2006. GCP-WD is a gamma-tubulin targeting factor required for
969 centrosomal and chromatin-mediated microtubule nucleation. *Nat Cell Biol*. 8:137-147.

970 Magescas, J., S. Eskinazi, M.V. Tran, and J.L. Feldman. 2021. Centriole-less pericentriolar material
971 serves as a microtubule organizing center at the base of C. elegans sensory cilia. *Curr Biol*.
972 31:2410-2417.

973 Martin, M., and A. Akhmanova. 2018. Coming into Focus: Mechanisms of Microtubule Minus-End
974 Organization. *Trends Cell Biol*. 28:574-588.

975 Martin, M., A. Veloso, J. Wu, E.A. Katrukha, and A. Akhmanova. 2018. Control of endothelial cell
976 polarity and sprouting angiogenesis by non-centrosomal microtubules. *Elife*. 7:e33864.

977 Meiring, J.C.M., B.I. Shneyer, and A. Akhmanova. 2020. Generation and regulation of microtubule
978 network asymmetry to drive cell polarity. *Curr Opin Cell Biol*. 62:86-95.

979 Meitinger, F., J.V. Anzola, M. Kaulich, A. Richardson, J.D. Stender, C. Benner, C.K. Glass, S.F. Dowdy,
980 A. Desai, A.K. Shiau, and K. Oegema. 2016. 53BP1 and USP28 mediate p53 activation and G1
981 arrest after centrosome loss or extended mitotic duration. *J Cell Biol*. 214:155-166.

982 Meitinger, F., M. Ohta, K.Y. Lee, S. Watanabe, R.L. Davis, J.V. Anzola, R. Kabeche, D.A. Jenkins, A.K.
983 Shiau, A. Desai, and K. Oegema. 2020. TRIM37 controls cancer-specific vulnerability to PLK4
984 inhibition. *Nature*. 585:440-446.

985 Meng, W., Y. Mushika, T. Ichii, and M. Takeichi. 2008. Anchorage of microtubule minus ends to
986 adherens junctions regulates epithelial cell-cell contacts. *Cell*. 135:948-959.

987 Mennella, V., D.A. Agard, B. Huang, and L. Pelletier. 2014. Amorphous no more: subdiffraction view
988 of the pericentriolar material architecture. *Trends Cell Biol*. 24:188-197.

989 Mennella, V., B. Keszthelyi, K.L. McDonald, B. Chhun, F. Kan, G.C. Rogers, B. Huang, and D.A. Agard.
990 2012. Subdiffraction-resolution fluorescence microscopy reveals a domain of the
991 centrosome critical for pericentriolar material organization. *Nat Cell Biol*. 14:1159-1168.

992 Meraldi, P. 2016. Centrosomes in spindle organization and chromosome segregation: a mechanistic
993 view. *Chromosome Res*. 24:19-34.

994 Mimori-Kiyosue, Y., I. Grigoriev, G. Lansbergen, H. Sasaki, C. Matsui, F. Severin, N. Galjart, F.
995 Grosveld, I. Vorobjev, S. Tsukita, and A. Akhmanova. 2005. CLASP1 and CLASP2 bind to EB1
996 and regulate microtubule plus-end dynamics at the cell cortex. *J Cell Biol*. 168:141-153.

997 Mogensen, M.M., A. Malik, M. Piel, V. Bouckson-Castaing, and M. Bornens. 2000. Microtubule
998 minus-end anchorage at centrosomal and non-centrosomal sites: the role of ninein. *J Cell Sci*.
999 113 (Pt 17):3013-3023.

1000 Muroyama, A., and T. Lechler. 2017. Microtubule organization, dynamics and functions in
1001 differentiated cells. *Development*. 144:3012-3021.

1002 Nijenhuis, W., M.M.P. van Grinsven, and L.C. Kapitein. 2020. An optimized toolbox for the
1003 optogenetic control of intracellular transport. *J Cell Biol*. 219:e201907149.

1004 Noordstra, I., Q. Liu, W. Nijenhuis, S. Hua, K. Jiang, M. Baars, S. Remmelzwaal, M. Martin, L.C.
1005 Kapitein, and A. Akhmanova. 2016. Control of apico-basal epithelial polarity by the
1006 microtubule minus-end-binding protein CAMSAP3 and spectraplakin ACF7. *J Cell Sci*.
1007 129:4278-4288.

1008 Oddoux, S., K.J. Zaal, V. Tate, A. Kenea, S.A. Nandkeolyar, E. Reid, W.H. Liu, and E. Ralston. 2013.
1009 Microtubules that form the stationary lattice of muscle fibers are dynamic and nucleated at
1010 Golgi elements. *Journal of Cell Biology*. 203:205-213.

1011 Paz, J., and J. Luders. 2017. Microtubule-Organizing Centers: Towards a Minimal Parts List. *Trends*
1012 *Cell Biol*:S0962-8924(0917)30187-30183.

1013 Pollock, R., R. Issner, K. Zoller, S. Natesan, V.M. Rivera, and T. Clackson. 2000. Delivery of a stringent
1014 dimerizer-regulated gene expression system in a single retroviral vector. *Proc Natl Acad Sci U*
1015 *S A*. 97:13221-13226.

1016 Pongrakhananon, V., H. Saito, S. Hiver, T. Abe, G. Shioi, W. Meng, and M. Takeichi. 2018. CAMSAP3
1017 maintains neuronal polarity through regulation of microtubule stability. *Proc Natl Acad Sci U*
1018 *S A*. 115:9750-9755.

1019 Prosser, S.L., and L. Pelletier. 2020. Centriolar satellite biogenesis and function in vertebrate cells. *J*
1020 *Cell Sci*. 133:jcs239566.

1021 Purohit, A., S.H. Tynan, R. Vallee, and S.J. Doxsey. 1999. Direct interaction of pericentrin with
1022 cytoplasmic dynein light intermediate chain contributes to mitotic spindle organization. *J*
1023 *Cell Biol*. 147:481-492.

1024 Raff, J.W. 2019. Phase Separation and the Centrosome: A Fait Accompli? *Trends Cell Biol*. 29:612-
1025 622.

1026 Ran, F.A., P.D. Hsu, J. Wright, V. Agarwala, D.A. Scott, and F. Zhang. 2013. Genome engineering using
1027 the CRISPR-Cas9 system. *Nat Protoc*. 8:2281-2308.

1028 Redwine, W.B., M.E. DeSantis, I. Hollyer, Z.M. Htet, P.T. Tran, S.K. Swanson, L. Florens, M.P.
1029 Washburn, and S.L. Reck-Peterson. 2017. The human cytoplasmic dynein interactome
1030 reveals novel activators of motility. *Elife*. 6:e28257.

1031 Rios, R.M. 2014. The centrosome-Golgi apparatus nexus. *Philos Trans R Soc Lond B Biol Sci*.
1032 369:20130462.

1033 Rivero, S., J. Cardenas, M. Bornens, and R.M. Rios. 2009. Microtubule nucleation at the cis-side of
1034 the Golgi apparatus requires AKAP450 and GM130. *EMBO J*. 28:1016-1028.

1035 Sallee, M.D., and J.L. Feldman. 2021. Microtubule organization across cell types and states. *Curr Biol*.
1036 31:R506-R511.

1037 Schlager, M.A., A. Serra-Marques, I. Grigoriev, L.F. Gumy, M. Esteves da Silva, P.S. Wulf, A.
1038 Akhmanova, and C.C. Hoogenraad. 2014. Bicaudal d family adaptor proteins control the
1039 velocity of Dynein-based movements. *Cell Rep*. 8:1248-1256.

1040 Schmidt, T.I., J. Kleylein-Sohn, J. Westendorf, M. Le Clech, S.B. Lavoie, Y.D. Stierhof, and E.A. Nigg.
1041 2009. Control of centriole length by CPAP and CP110. *Curr Biol*. 19:1005-1011.

1042 Shinohara, H., N. Sakayori, M. Takahashi, and N. Osumi. 2013. Ninein is essential for the
1043 maintenance of the cortical progenitor character by anchoring the centrosome to
1044 microtubules. *Biol Open*. 2:739-749.

1045 Sonnen, K.F., A.M. Gabryjonczyk, E. Anselm, Y.D. Stierhof, and E.A. Nigg. 2013. Human Cep192 and
1046 Cep152 cooperate in Plk4 recruitment and centriole duplication. *J Cell Sci*. 126:3223-3233.

1047 Sonnen, K.F., L. Schermelleh, H. Leonhardt, and E.A. Nigg. 2012. 3D-structured illumination
1048 microscopy provides novel insight into architecture of human centrosomes. *Biology Open*.
1049 1:965-976.

1050 Spektor, A., W.Y. Tsang, D. Khoo, and B.D. Dynlacht. 2007. Cep97 and CP110 suppress a cilia
1051 assembly program. *Cell*. 130:678-690.

1052 Splinter, D., M.E. Tanenbaum, A. Lindqvist, D. Jaarsma, A. Flotho, K.L. Yu, I. Grigoriev, D. Engelsma,
1053 E.D. Haasdijk, N. Keijzer, J. Demmers, M. Fornerod, F. Melchior, C.C. Hoogenraad, R.H.
1054 Medema, and A. Akhmanova. 2010. Bicaudal D2, dynein and kinesin-1 associate with nuclear
1055 pore complexes and regulate centrosome and nuclear positioning during mitotic entry. *PLoS*
1056 *Biol*. 8:e1000350.

1057 Steinman, J.B., C.C. Santarossa, R.M. Miller, L.S. Yu, A.S. Serpinskaya, H. Furukawa, S. Morimoto, Y.
1058 Tanaka, M. Nishitani, M. Asano, R. Zalyte, A.E. Ondrus, A.G. Johnson, F. Ye, M.V. Nachury, Y.

1059 Fukase, K. Aso, M.A. Foley, V.I. Gelfand, J.K. Chen, A.P. Carter, and T.M. Kapoor. 2017.
1060 Chemical structure-guided design of dynapyrazoles, cell-permeable dynein inhibitors with a
1061 unique mode of action. *Elife*. 6:e25174.

1062 Stolz, A., N. Ertych, and H. Bastians. 2015. A phenotypic screen identifies microtubule plus end
1063 assembly regulators that can function in mitotic spindle orientation. *Cell Cycle*. 14:827-837.

1064 Takahashi, M., A. Yamagiwa, T. Nishimura, H. Mukai, and Y. Ono. 2002. Centrosomal proteins CG-
1065 NAP and kendrin provide microtubule nucleation sites by anchoring gamma-tubulin ring
1066 complex. *Mol Biol Cell*. 13:3235-3245.

1067 Tanaka, N., W. Meng, S. Nagae, and M. Takeichi. 2012. Nezha/CAMSAP3 and CAMSAP2 cooperate in
1068 epithelial-specific organization of noncentrosomal microtubules. *Proc Natl Acad Sci U S A*.
1069 109:20029-20034.

1070 Tang, C.J.C., R.H. Fu, K.S. Wu, W.B. Hsu, and T.K. Tang. 2009. CPAP is a cell-cycle regulated protein
1071 that controls centriole length. *Nat Cell Biol*. 11:825-831.

1072 Tas, R.P., A. Chazeau, B.M.C. Cloin, M.L.A. Lambers, C.C. Hoogenraad, and L.C. Kapitein. 2017.
1073 Differentiation between Oppositely Oriented Microtubules Controls Polarized Neuronal
1074 Transport. *Neuron*. 96:1264-1271.

1075 Tibelius, A., J. Marhold, H. Zentgraf, C.E. Heilig, H. Neitzel, B. Ducommun, A. Rauch, A.D. Ho, J.
1076 Bartek, and A. Kramer. 2009. Microcephalin and pericentrin regulate mitotic entry via
1077 centrosome-associated Chk1. *J Cell Biol*. 185:1149-1157.

1078 Toya, M., S. Kobayashi, M. Kawasaki, G. Shioi, M. Kaneko, T. Ishiuchi, K. Misaki, W. Meng, and M.
1079 Takeichi. 2016. CAMSAP3 orients the apical-to-basal polarity of microtubule arrays in
1080 epithelial cells. *Proc Natl Acad Sci U S A*. 113:332-337.

1081 Vergarajauregui, S., R. Becker, U. Steffen, M. Sharkova, T. Esser, J. Petzold, F. Billing, M.S. Kapiloff, G.
1082 Schett, I. Thievessen, and F.B. Engel. 2020. AKAP6 orchestrates the nuclear envelope
1083 microtubule-organizing center by linking golgi and nucleus via AKAP9. *Elife*. 9:e61669.

1084 Vinopal, S., M. Cernohorska, V. Sulimenko, T. Sulimenko, V. Vosecka, M. Flemr, E. Draberova, and P.
1085 Draber. 2012. gamma-Tubulin 2 nucleates microtubules and is downregulated in mouse
1086 early embryogenesis. *PLoS One*. 7:e29919.

1087 Wang, G., Q. Chen, X. Zhang, B. Zhang, X. Zhuo, J. Liu, Q. Jiang, and C. Zhang. 2013. PCM1 recruits
1088 Plk1 to the pericentriolar matrix to promote primary cilia disassembly before mitotic entry. *J*
1089 *Cell Sci*. 126:1355-1365.

1090 Wang, S., D. Wu, S. Quintin, R.A. Green, D.K. Cheerambathur, S.D. Ochoa, A. Desai, and K. Oegema.
1091 2015. NOCA-1 functions with gamma-tubulin and in parallel to Patronin to assemble non-
1092 centrosomal microtubule arrays in C. elegans. *Elife*. 4:e08649.

1093 Watanabe, S., F. Meitinger, A.K. Shiau, K. Oegema, and A. Desai. 2020. Centriole-independent
1094 mitotic spindle assembly relies on the PCNT-CDK5RAP2 pericentriolar matrix. *J Cell Biol*.
1095 219:e202006010.

1096 Wong, Y.L., J.V. Anzola, R.L. Davis, M. Yoon, A. Motamedi, A. Kroll, C.P. Seo, J.E. Hsia, S.K. Kim, J.W.
1097 Mitchell, B.J. Mitchell, A. Desai, T.C. Gahman, A.K. Shiau, and K. Oegema. 2015. Cell biology.
1098 Reversible centriole depletion with an inhibitor of Polo-like kinase 4. *Science*. 348:1155-
1099 1160.

1100 Woodruff, J.B., B. Ferreira Gomes, P.O. Widlund, J. Mahamid, A. Honigmann, and A.A. Hyman. 2017.
1101 The Centrosome Is a Selective Condensate that Nucleates Microtubules by Concentrating
1102 Tubulin. *Cell*. 169:1066-1077.

1103 Wu, J., C. de Heus, Q. Liu, B.P. Bouchet, I. Noordstra, K. Jiang, S. Hua, M. Martin, C. Yang, I. Grigoriev,
1104 E.A. Katrukha, A.F. Altelaar, C.C. Hoogenraad, R.Z. Qi, J. Klumperman, and A. Akhmanova.
1105 2016. Molecular Pathway of Microtubule Organization at the Golgi Apparatus. *Dev Cell*.
1106 39:44-60.

1107 Yang, C., J. Wu, C. de Heus, I. Grigoriev, N. Liv, Y. Yao, I. Smal, E. Meijering, J. Klumperman, R.Z. Qi,
1108 and A. Akhmanova. 2017. EB1 and EB3 regulate microtubule minus end organization and
1109 Golgi morphology. *J Cell Biol*. 216:3179-3198.

1110 Yang, R., and J.L. Feldman. 2015. SPD-2/CEP192 and CDK Are Limiting for Microtubule-Organizing
1111 Center Function at the Centrosome. *Curr Biol*. 25:1924-1931.

1112 Yau, K.W., S.F. van Beuningen, I. Cunha-Ferreira, B.M. Cloin, E.Y. van Battum, L. Will, P. Schatzle, R.P.
1113 Tas, J. van Krugten, E.A. Katrukha, K. Jiang, P.S. Wulf, M. Mikhaylova, M. Harterink, R.J.
1114 Pasterkamp, A. Akhmanova, L.C. Kapitein, and C.C. Hoogenraad. 2014. Microtubule minus-
1115 end binding protein CAMSAP2 controls axon specification and dendrite development.
1116 *Neuron*. 82:1058-1073.

1117 Yeow, Z.Y., B.G. Lambrus, R. Marlow, K.H. Zhan, M.A. Durin, L.T. Evans, P.M. Scott, T. Phan, E. Park,
1118 L.A. Ruiz, D. Moralli, E.G. Knight, L.M. Badder, D. Novo, S. Haider, C.M. Green, A.N.J. Tutt, C.J.
1119 Lord, J.R. Chapman, and A.J. Holland. 2020. Targeting TRIM37-driven centrosome
1120 dysfunction in 17q23-amplified breast cancer. *Nature*. 585:447-452.

1121 Zheng, Y., R.A. Buchwalter, C. Zheng, E.M. Wight, J.V. Chen, and T.L. Megraw. 2020. A perinuclear
1122 microtubule-organizing centre controls nuclear positioning and basement membrane
1123 secretion. *Nat Cell Biol*. 22:297-309.

1124 Zhu, F., S. Lawo, A. Bird, D. Pinchev, A. Ralph, C. Richter, T. Muller-Reichert, R. Kittler, A.A. Hyman,
1125 and L. Pelletier. 2008. The mammalian SPD-2 ortholog Cep192 regulates centrosome
1126 biogenesis. *Curr Biol*. 18:136-141.

1127 Zhu, X.D., and I. Kaverina. 2013. Golgi as an MTOC: making microtubules for its own good.
1128 *Histochemistry and Cell Biology*. 140:361-367.

1129

1130 **Figure legends.**

1131 **Figure 1. Formation and characterization of aMTOCs in AKAP450/CAMSAP2 knockout cells**

1132 (A) Immunofluorescence images of control or centrinone B-treated wild type (WT) RPE1 cells stained
1133 for centrioles (CEP135, red; centrin, green). The zooms of the boxed area show the centrioles stained
1134 with the indicated markers.

1135 (B) Quantification shows the percentage of cells with centrioles before and after the centrinone
1136 treatment. 350 cells (n=7 fields of view) analyzed for each measurement in three independent
1137 experiments. The statistical significance was determined by unpaired two-tailed Mann-Whitney test
1138 in Prism 9.1 (***p<0.001). Values represent mean±SD.

1139 (C) Immunofluorescence images of centrinone-treated WT RPE1 cells stained for pericentrin (PCNT,
1140 green) and the Golgi marker GM130 (red). Inset shows the merged image of the boxed area.

1141 (D) Diagrams of the microtubule organization in WT and knockout (KO) cells used.

1142 (E) Immunofluorescence images of centrinone-treated WT and knockout RPE1 cell lines stained for
1143 pericentrin (green) and microtubules (α-tubulin, red). Enlargements of the boxed areas are shown in
1144 the bottom row.

1145 (F) Immunofluorescence images of centrinone-treated AKAP450/CAMSAP2 knockout RPE1 cells
1146 stained for different PCM components as indicated and imaged by STED microscopy.

1147 (G) Quantification of the length and width of cylindrical PCM clusters. n=65 cells analyzed in three
1148 independent experiments. Values represent mean±SD.

1149 (H) (Top left) Two frames of time-lapse images of centrinone-treated AKAP450/CAMSAP2 knockout
1150 RPE1 cells stably expressing GFP-CDK5RAP2 prior to FRAP experiments. (Top right) Schemes show
1151 regions of aMTOC where photobleaching was performed. (Middle) Kymographs illustrating
1152 fluorescence of unbleached aMTOC (No FRAP), fully photobleached aMTOC (Whole FRAP) and
1153 partially photobleached MTOC (Partial FRAP). (Bottom) Time-lapse images illustrating partial FRAP of
1154 a compact aMTOC. Time is min:sec.

1155 (I) Normalized fluorescence intensity as a function of time. The blue line shows averaged intensity
1156 traces of unbleached MTOCs (No FRAP), the black line shows averaged intensity traces of fully
1157 photobleached MTOCs (Whole FRAP), the red line shows averaged intensity traces of whole MTOC
1158 that were partially photobleached (whole MTOC intensity, Partial FRAP) and the green line shows
1159 averaged intensity traces of the photobleached region of the partially photobleached MTOC (FRAP
1160 region intensity, Partial FRAP). n=3 for No FRAP, 3 for Whole FRAP, 5 for Partial FRAP (whole MTOC

1161 intensity) and 5 for Partial FRAP (FRAP region intensity); time-lapse images of ~1600 timepoints with
1162 2 s interval were analyzed for each measurement. Values are mean±SD.

1163

1164 **Figure 2. Molecular composition of aMTOCs in AKAP450/CAMSAP2 knockout cells**

1165 (A-C) Immunofluorescence images of control or centrinone-treated AKAP450/CAMSAP2 knockout
1166 RPE1 cells stained for and depleted of the indicated proteins.

1167 (D, F-I) Immunofluorescence images of centrinone-treated AKAP450/CAMSAP2 knockout RPE1 cells
1168 stained for and depleted of the indicated proteins.

1169 (E) Immunofluorescence images of centrinone-treated AKAP450/CAMSAP2/p53 knockout and
1170 AKAP450/CAMSAP2/p53/pericentrin knockout RPE1 cells stained as indicated.

1171 In panels A-I, insets show enlargements of the merged channels of the boxed areas, and dashed lines
1172 indicate cell edges in panels where these are poorly visible.

1173 (J) Summarizing table of PCM localization and the depletion effects on aMTOC formation in
1174 AKAP450/CAMSAP2 knockout RPE1 cells. NT, not tested.

1175

1176 **Figure 3. Microtubule organization in acentriolar cells missing different aMTOC components**

1177 (A) Immunofluorescence images of centrinone-treated AKAP450/CAMSAP2 knockout RPE1 cells
1178 depleted of the indicated proteins and stained for microtubules (α-tubulin, red) and different PCM
1179 proteins (green). Insets show enlargements of the merged channels of the boxed areas and dashed
1180 lines show cell boundaries.

1181 (B) Quantification of the normalized overall microtubule intensity for the indicated conditions. The
1182 number of cells analyzed in three independent experiments: n=56 (siLuci), 45 (siPCNT), 33
1183 (siCDK5RAP2), 36 (siNinein), 43 (siγ-tubulin) and 28 (siDHC). The statistical significance was
1184 determined by unpaired two-tailed Mann-Whitney test in Prism 9.1 (***$p<0.001$). Values represent
1185 mean±SD.

1186 (C) Microtubule images were split into a radial and non-radial components (heat maps) based on
1187 microtubule orientation in relation to the PCM clusters or the brightest point, as described in
1188 Methods.

1189 (D) Quantification of the proportion of the non-radial microtubules shown in panel C (see Methods
1190 for details). The number of cells analyzed for each measurement in three independent experiments:
1191 n=25 (siLuci), 43 (siPCNT), 32 (siCDK5RAP2), 34 (siNinein), 37 (siγ-tubulin) and 25 (siDHC). The
1192 statistical significance was determined by unpaired two-tailed Mann-Whitney test in Prism 9.1
1193 (***p<0.001). Values represent mean±SD.

1194 (E) Diagram illustrating the distribution of PCM clusters and microtubule organization upon the
1195 depletion of the indicated proteins in centrinone-treated AKAP450/CAMSAP2 knockout cells.

1196

1197 **Figure 4. Microtubule- and dynein-dependent disassembly of aMTOCs**

1198 (A) Diagram illustrating different order of cell treatments with centrinone and/or dynapyrazole A (5
1199 µM) and the time points when the cells were fixed.

1200 (B) Immunofluorescence staining of centrinone-treated AKAP450/CAMSAP2 knockout cells treated as
1201 shown in panel A. Dashed red circles represent the areas occupied by PCM clusters in each condition.

1202 (C) Quantification of the area occupied by PCM clusters in each condition, as shown in panels A and B.
1203 n=35-53 cells analyzed for each measurement in three independent experiments. The statistical
1204 significance was determined by unpaired two-tailed Mann-Whitney test in Prism 9.1 (not significant
1205 (NS), *P*<0.12; **P*<0.033; ****P*<0.001). Values are represented as mean±SD.

1206 (D) Western blot showing that 3 hr treatment with dynaprazole A does not affect the expression of
1207 the endogenous dynein heavy chain and the dynactin large subunit p150Glued.

1208 (E) Time-lapse images of centrinone-treated AKAP450/CAMSAP2 knockout RPE1 cells stably
1209 expressing GFP-CDK5RAP2. Microtubules were visualized by treating cells with 100 nM SiR-tubulin
1210 overnight. Red arrows show the immobilized PCM clusters at indicated timepoints. Time is min:sec.
1211 Time-lapse images of the same cell prior to the nocodazole treatment were shown in Figure 1 - figure
1212 supplement 2B.

1213 (F) (Top) Kymograph illustrating the motility of PCM clusters during microtubule disassembly with
1214 nocodazole. (Bottom) Measurements of the normalized microtubule (SiR-tubulin) fluorescence
1215 intensity (red plot, left Y-axis) and the instantaneous velocity of GFP-CDK5RAP2 clusters (green plot,
1216 right Y-axis) during the movement of GFP-CDK5RAP2 clusters away from aMTOC. Microtubule density
1217 around each PCM cluster was determined by measuring mean fluorescence intensity of SiR-tubulin in
1218 a circular area with a 2 µm radius centered on the PCM cluster and normalizing it to the mean
1219 fluorescence intensity of 20 images prior to nocodazole addition (set as 100%). The moment when a

1220 PCM cluster started to move out of the aMTOC was set as the initial time point (0 min) for this cluster,
1221 and the subsequent PCM cluster motion velocity and the relative local microtubule density of 43 time
1222 points were calculated and averaged. n=12 clusters were analyzed in each condition. Values are
1223 represented as mean±SD.

1224 (G) Motor-PAINT images of centrinone-treated AKAP450/CAMSAP2 knockout RPE1 cells before and
1225 after nocodazole treatment. Plus-end-out microtubules are shown in white whereas minus-end-out
1226 microtubules are shown in magenta. Asterisks represent the putative position of aMTOC.

1227 (H) Summarizing diagram illustrating microtubule organization and the motility of GFP-CDK5RAP2-
1228 positive PCM clusters during nocodazole treatment and dynapyrazole A (treat first) and nocodazole
1229 co-treatment.

1230

1231 **Figure 5. Dynamics of microtubule nucleation and MTOC re-assembly in acentriolar cells**

1232 (A) Immunofluorescence images of microtubule regrowth after nocodazole washout at the indicated
1233 timepoints in centrinone-treated AKAP450/CAMSAP2 knockout RPE1 cells stained for PCM
1234 components (green) and newly nucleated microtubules (EB1, red). A Golgi marker, GM130 (blue), is
1235 included in the left row, and zooms of the boxed regions (numbered 1 and 2) show that microtubules
1236 nucleate from PCM clusters but not from the Golgi membranes. Dashed lines show cell boundaries.

1237 (B) Immunofluorescence images of microtubule regrowth experiments after depletion of the indicated
1238 proteins in centrinone-treated AKAP450/CAMSAP2 knockout RPE1 cells stained for the indicated PCM
1239 markers (green) and EB1 as a marker of nascent microtubules (red). Cell outlines are indicated with
1240 dashed lines and enlargements of the merged channels of the boxed areas are shown on the right.

1241 (C) Quantification of normalized microtubule intensity at 30 s after nocodazole washout in control
1242 cells and cells depleted of the indicated PCM proteins. n=40 (siLuci, siPCNT), 57 (siCDK5RAP2), 48
1243 (siNIN), 45 (siγ-tubulin) and 50 (siDHC) cells analyzed for each measurement in three independent
1244 experiments. The statistical significance was determined by unpaired two-tailed Mann-Whitney test
1245 in Prism 9.1 (**P<0.002; ***P<0.001). Values are represented as mean±SD.

1246 (D) Time-lapse images of centrinone-treated AKAP450/CAMSAP2 knockout RPE1 cells stably
1247 expressing GFP-CDK5RAP2 before and after nocodazole washout. Dispersed GFP-CDK5RAP2-positive
1248 PCM clusters (GFP, green) serve as microtubule nucleation sites (SiR-tubulin, red) and coalesce into a
1249 big cluster after nocodazole washout. Time is min:sec.

1250 (E) Immunofluorescence images of centrinone-treated AKAP450/CAMSAP2 knockout RPE1 cells
1251 stained for pericentrin (green) and microtubules (α-tubulin, red) at the indicated timepoints after
1252 nocodazole washout.

1253 (F) Measurements of normalized fluorescence intensity of PCM clusters at the indicated distances in
1254 relation to the brightest point, as described in Methods. The biggest PCM cluster (which normally also
1255 had the highest fluorescence intensity) was selected as the center, around which 10 concentric circles
1256 with 2 µm width were drawn. Fluorescence intensity of PCM clusters in these concentric circles was
1257 measured automatically and normalized by the sum of the total PCM intensity in each cell per
1258 condition. n=12 cells per plot per timepoint. Values represent mean±SD.

1259 (G) Summarizing diagram illustrating microtubule organization and motility of GFP-CDK5RAP2-positive
1260 PCM clusters during nocodazole washout.

1261

1262 **Figure 6. CAMSAP2-driven microtubule organization in acentriolar cells**

1263 (A) Immunofluorescence images of control or centrinone treated AKAP450 knockout RPE1 cells
1264 stained for CAMSAP2 (green), PCM protein (γ-tubulin, cyan) and microtubules (α-tubulin, red).
1265 Enlargements show the boxed regions of the merged images.

1266 (B) Time lapse images of centrinone treated AKAP450 knockout RPE1 cells stably expressing GFP-
1267 CDK5RAP2 (green). Microtubules were labeled with 100 nM SiR-tubulin overnight (red, top row). The
1268 maximum intensity projection includes 200 frames, 200 ms/frame. Red arrows show the motion
1269 directions of GFP-CDK5RAP2-positive PCM clusters. Time is min:sec.

1270 (C) A diagram of microtubule organization and PCM motility in AKAP450 knockout cells.

1271 (D, E) Diagram of the inducible heterodimerization assay with ppKin14 and CAMSAP2. (D) CAMSAP2
1272 was tagged with mCherry and fused to a tandemly repeated FKBP domain; tetramerized ppKin14 was
1273 tagged with TagBFP and fused to FRB. Rapalog induces the binding of CAMSAP2 and ppKin14 by linking
1274 FKBP to FRB. (E) Rapalog treatment induces the binding of CAMSAP2 (red) and ppKin14 (blue) and the
1275 formation of radial microtubule network. In this scheme, PCM-anchored microtubules are not shown.

1276 (F) Immunofluorescence images of centrinone-treated AKAP450/CAMSAP2 knockout RPE1 cells co-
1277 transfected with 2FKBP-mCherry-CAMSAP2 and FRB-TagBFP-GCN4-ppKin14 and stained for the
1278 indicated proteins in cells treated with DMSO or rapalog. Zooms show the magnifications of boxed
1279 areas.

1280 (G) Quantification of the proportion of cells with a radial, whirlpool-like or non-radial microtubule
1281 organization with and without rapalog treatment. Numbers on the histogram show the percentages.
1282 414 cells treated with DMSO (-Rapa) and 385 cells treated with rapalog (+Rapa) analyzed for each
1283 measurement in three independent experiments (n=3). Values represent mean±SD.

1284

1285 **Figure 7. The role of the PCM in CAMSAP2-driven formation of aMTOCs**

1286 (A,B) Immunofluorescence images of centrinone-treated AKAP450/CAMSAP2/p53/pericentrin
1287 knockout RPE1 cells transfected with 2FKBP-mCherry-CAMSAP2 and FRB-TagBFP-GCN4-ppKi14 and
1288 stained for the indicated components before (top) or after an overnight rapalog treatment. Zooms
1289 show magnifications of boxed areas. Black dashed lines show the position of the nucleus.

1290 (C) Cells treated as described for panel A were co-transfected with GFP-pericentrin and stained for
1291 mitochondria (cytochrome C, red) and CAMSAP2 (red) in same channel overnight after rapalog
1292 addition. Zooms show magnifications of boxed areas.

1293 (D) Quantification of the proportion of cells with different types of microtubule minus end
1294 organization before and after overnight rapalog treatment. Numbers on the histogram show the
1295 percentages. 334 (-Rapa), 424(+Rapa) cells of AKAP450/CAMSAP2/p53/pericentrin knockout RPE1
1296 cells, 206(-Rapa) and 239(+Rapa) of AKAP450/CAMSAP2/CDK5RAP2/MMG/p53/pericentrin knockout
1297 RPE1 cells analyzed for each measurement in three independent experiments (n=3). Values represent
1298 mean±SD.

1299 (E) Immunofluorescence images of centrinone-treated
1300 AKAP450/CAMSAP2/CDK5RAP2/MMG/p53/pericentrin knockout RPE1 cells transfected with 2FKBP-
1301 mCherry-CAMSAP2 and FRB-TagBFP-GCN4-ppKi14 and stained for microtubules (α-tubulin, green)
1302 after an overnight rapalog treatment. Zooms show magnifications of boxed areas.

1303 **Legends to Supplemental Figures**

1304 **Figure 1 – figure supplement 1. Characterization of aMTOCs in AKAP450/CAMSAP2 knockout cells**

1305 (A) Immunofluorescence images of centrinone B treated AKAP450 knockout RPE1 cells stained for
1306 CAMSAP2 (green) and γ-tubulin (red), transfected either with control (Luciferase) or CAMSAP2 siRNAs.
1307 Insets show enlargements of the merged images of the boxed areas.

1308 (B) Quantification of CAMSAP2 depletion and aMTOC formation related to panel A. For normalized
1309 CAMSAP2 intensity, n=76 (siLuciferase) and 62 (siCAMSAP2) cells from three independent experiment
1310 were analyzed; to calculate the percentage of cells showing dispersed or clustered PCM, n=300
1311 (siLuciferase) and 299 (siCAMSAP2) cells analyzed for each measurement in three independent
1312 experiments. The statistical significance was determined by unpaired two-tailed Mann-Whitney test
1313 in Prism 9.1 (***$p<0.001$). Values represent mean±SD.

1314 (C) Immunofluorescence images of AKAP450/CAMSAP2 knockout treated with DMSO or centrinone B
1315 and stained for pericentrin and centrin show the main PCM organization types (centrin-negative cells
1316 with cylindrical or round PCM cluster, dispersed PCM or no cluster, and centrin-positive centrosomes)
1317 in each condition. Enlargements of the merged channels of the boxed areas are shown on the right.

1318 (D) Quantification of the main PCM organization types in centrinone-treated AKAP450 knockout and
1319 AKAP450/CAMSAP2 knockout RPE1 cells. Numbers on the histogram show the percentages. 465
1320 (AKAP450 KO) and 495 (AKAP450/CAMSAP2 KO) cells analyzed for each measurement in three
1321 independent experiments (n=3). Values represent mean±SD.

1322 (E) Diagram showing the generation of CPAP or PLK4 depleted AKAP450/CAMSAP2 knockout RPE1
1323 cells with different drug treatments. Cells were transfected with siRNAs to depleted CPAP and PLK4
1324 respectively. After 2 days, the transfection was performed again to increase the depletion efficiency.
1325 After 2 more days, cells were treated with thymidine to block cell proliferation or with a combination
1326 of thymidine and centrinone B, or thymidine, centrinone B and the PLK1 inhibitor BI 2536 for one or
1327 three days. Cells were fixed for the first time (Fix1) after a 24 hr drug treatment, and for the second
1328 time (Fix2) after a 72 hr drug treatment.

1329 (F) Quantification of the main PCM organization types, as described for panel D, for cells prepared as
1330 described in panel E. Numbers on the histogram show the percentages and numbers in brackets show
1331 cells analyzed for each measurement in three independent experiments (n=3; 247-612 cells analyzed
1332 per condition). Values represent mean±SD.

1333 (G-I) Immunofluorescence images of Fix2 (as described in panel E) showing control (transfected with
1334 siRNA against Luciferase), or depleted of PLK4 or CPAP and treated as indicated. Cells were stained for
1335 centrioles (CEP135, centrin), PCM proteins (PCNT) and microtubules (α-tubulin). Images illustrate the
1336 PCM organization types in each condition. Insets show enlargements of the merged channels for the
1337 boxed areas.

1338

1339 **Figure 1 – figure supplement 2. PCM dynamics visualized with GFP-CDK5RAP2**

1340 (A) Immunofluorescence images of control and centrinone B treated WT RPE1 cell stably expressing
1341 GFP-CDK5RAP2 (green) stained for α-tubulin (red) and pericentrin (PCNT, blue). Zooms show
1342 enlargements of the boxed regions.

1343 (B) Time-lapse images of centrinone-treated AKAP450/CAMSAP2 knockout RPE1 cells stably
1344 expressing GFP-CDK5RAP2. Microtubules are visualized by treating the cells with 100 nM SiR-tubulin
1345 overnight. PCM labeled with GFP-CDK5RAP2 (green) forms a stable cluster that functions as the MTOC.
1346 Zooms show the enlarged GFP channel of the boxed regions. Time is min:sec.

1347

1348 **Figure 2 – figure supplement 1. Characterization of PCM components localizing to aMTOCs in**
1349 **AKAP450/CAMSAP2 knockout cells**

1350 (A) Western blot showing that endogenous NEDD1 and CEP192 are present in centrinone-treated
1351 AKAP450/CAMSAP2 knockout cells.

1352 (B) Western blot results showing the depletion of the indicated PCM proteins.

1353 (C) Immunofluorescence images of centrinone-treated AKAP450/CAMSAP2 knockout RPE1 cells
1354 showing the localization and the effects of depletion of the indicated proteins on the aMTOCs. siRNA
1355 against luciferase was used as a control. Zooms show enlargements of the merged channels of the
1356 boxed areas.

1357

1358 **Figure 2 – figure supplement 2. Generation of the AKAP450/CAMSAP2/p53/pericentrin knockout**
1359 **RPE1 cell line**

1360 (A) Diagram illustrating two sgRNA sites targeting p53 exon 2 and exon 4. The green and red boxes
1361 indicate the position of the PAM sites, and the predicted Cas9 cut sites are indicated by scissors.

1362 (B,C) Genotyping results of the genomic mutation using gel-purified PCR product which covers exon 2
1363 and exon 4 of the p53-encoding gene in AKAP450/CAMSAP2/p53 knockout cell line and a diagram
1364 illustrating the induced inversion.

1365 (D) Diagram illustrating the binding sites of p53 antibodies and the position of the mutation induced
1366 in p53-encoding gene.

1367 (E,F) Immunofluorescence and Western blot images showing p53 expression in control and
1368 AKAP450/CAMSAP2/p53 knockout cells.

1369 (G-H) Genotyping results of the genomic mutation using gel-purified PCR product which covers the
1370 two sgRNAs targeting sites within pericentrin-encoding gene in AKAP450/CAMSAP2/p53/pericentrin
1371 knockout cell line and a diagram illustrating the induced genomic mutations within exon 5 of the
1372 pericentrin-encoding gene. The green and red boxes indicate the position of the PAM sites, and the
1373 predicted Cas9 cut sites are indicated by scissors.

1374 (I) Diagram illustrating the binding domain of the pericentrin antibody and the positions of the
1375 mutations induced downstream of the Cas9 cutting sites.

1376 (J) Immunofluorescence images confirming the loss of pericentrin in
1377 AKAP450/CAMSAP2/p53/pericentrin knockout cells.

1378 (K) Western blot confirming the loss of p53 and pericentrin in AKAP450/CAMSAP2/p53/pericentrin
1379 knockout cells.

1380

1381 **Figure 2 – figure supplement 3. Characterization of PCM organization in AKAP450/CAMSAP2/p53/**
1382 **pericentrin knockout cells**

1383 Immunofluorescence images of centrinone-treated AKAP450/CAMSAP2/p53 knockout (Ctl) and
1384 AKAP450/CAMSAP2/p53/pericentrin knockout (PCNT KO) RPE1 cells showing staining for the
1385 indicated proteins. Zooms of the boxed areas show merged channels.

1386

1387 **Figure 2 – figure supplement 4. Effects of the depletion or knockout of EB1 and EB3 on aMTOC**
1388 **formation in AKAP450/CAMSAP2 knockout cells**

1389 (A) Immunofluorescence images of centrinone-treated AKAP450/CAMSAP2 knockout cells stained for
1390 EB1 or EB3 and pericentrin showing effects of EB1 or EB3 depletion on aMTOCs.

1391 (B) Western blot confirming the loss of AKAP450 and CAMSAP2 in AKAP450/CAMSAP2/EB1/EB3
1392 mutant cells.

1393 (C) Immunofluorescence images of control or centrinone-treated AKAP450/CASMSAP2/EB1/EB3
1394 mutant RPE1 cells stained for the indicated proteins. Zooms of the boxed areas show merged
1395 channels.

1396

1397 **Figure 4 – Figure supplement 1. PCM dynamics during nocodazole treatment in centrinone-treated**
1398 **AKAP450/CAMSAP2 knockout cells**

1399 (A) Time-lapse images illustrating the dynamics of GFP-CDK5RAP2 clusters (green, white arrows) and
1400 microtubules (visualized with an overnight treatment with 100 nM SiR-tubulin, red) during nocodazole
1401 treatment. A single frame of the whole cell is on the bottom left, with the boxed area indicating the
1402 location of the enlarged images. Time is min:sec.

1403 (B) Motor-PAINT images of centrinone-treated AKAP450/CAMSAP2 knockout RPE1 cells before and
1404 after treatment with 10 µM nocodazole for 15 min (the same cells, colorized differently, are displayed
1405 in Figure 4G). Microtubule segments were assigned a color based on their absolute orientation, with
1406 their plus-ends pointing in the directions indicated with the compass. Asterisks indicate approximate
1407 assumed positions of aMTOCs.

1408

1409 **Figure 5 – figure supplement 1. PCM dynamics and microtubule regrowth during nocodazole**
1410 **washout in AKAP450/CAMSAP2 knockout cells**

1411 (A) Immunofluorescence images of acentriolar AKAP450/CAMSAP2 knockout RPE1 cells fixed at 30 s
1412 and 10 min after nocodazole washout and stained for the indicated markers. Zooms show the
1413 enlargements of boxed areas. Dashed lines show the cell boundaries.

1414 (B) Summarizing table showing the presence of PCM components in clusters (including centrosome
1415 and aMTOC) before and after nocodazole washout in indicated conditions.

1416 (C) Immunofluorescence images of control acentriolar AKAP450/CAMSAP2 knockout RPE1 cells and
1417 cells lacking the indicated PCM proteins fixed 2 min after nocodazole washout and stained for EB1 (a
1418 marker of growing microtubules, red) and different PCM proteins (γ-tubulin, NIN and DHC, green;
1419 CDK5RAP2 and PCNT, blue). Insets show the enlargements of the boxed areas and zooms show the
1420 radial and non-radial part of growing microtubules. Dashed lines show the cell boundaries.

1421 (D) Quantification of the proportion of non-radial microtubules 2 min after nocodazole washout. The
1422 radial and the non-radial microtubule intensities were measured and the non-radial microtubule
1423 intensity was normalized by dividing it by the sum of the radial and the non-radial microtubule
1424 intensities for each group. n=20-25 cells analyzed for each measurement in three independent
1425 experiments. The statistical significance was determined by unpaired two-tailed Mann-Whitney test
1426 in Prism 9.1 (***p<0.001). Values represent mean±SD.

1427 (E) Diagram showing microtubule regrowth and PCM assembly in control acentriolar
1428 AKAP450/CAMSAP2 knockout RPE1 cells and cells depleted of the indicated PCM proteins at 30 s and
1429 2 min after nocodazole washout.

1430

1431 **Figure 5 – figure supplement 2. Pericentrin is required for PCM clustering in acentriolar**
1432 **AKAP450/CAMSAP2 knockout RPE1 cells**

1433 Time-lapse images of centrinone-treated AKAP450/CAMSAP2 knockout RPE1 cells stably expressing
1434 GFP-CDK5RAP2 (green), which is diffusely distributed and does not form any clear clusters.
1435 Microtubule regrowth experiments show random nucleation of microtubules (labeled with 100nM
1436 SiR-tubulin overnight) that remain disorganized. Summarizing diagram shows PCM clusters and
1437 microtubule network in the indicated conditions.

1438

1439 **Figure 6 – figure supplement 1. PCM dynamics and the effects of CAMSAP2 clustering on PCM**
1440 **organization in centrinone-treated RPE1 cells lacking AKAP450**

1441 (A) Time-lapse images illustrating the dynamics of PCM clusters (green, white arrows) and
1442 microtubules (SiR-tubulin, red) after nocodazole washout in centrinone-treated AKAP450 knockout
1443 RPE1 cells stably expressing GFP-CDK5RAP2. A single frame of the whole cell with numbered boxed
1444 areas indicating the location of enlarged time-lapse images is shown on the left. White arrows indicate
1445 moving PCM clusters after microtubules re-grow. Time is min:sec.

1446 (B) Time-lapse images of centrinone-treated AKAP450 knockout RPE1 cells stably expressing GFP-
1447 CDK5RAP2. GFP-CDK5RAP2 forms small clusters that are dynamic before microtubules (SiR-tubulin,
1448 red) are disassembled by nocodazole treatment. Red arrows show that these clusters become
1449 immobile when microtubules are completely depolymerized (enlargements of the boxed areas shown
1450 in the bottom rows). GFP-CDK5RAP2-positive clusters are sites of microtubule nucleation after

1451 nocodazole washout and become dynamic again once microtubules re-grow. The maximum intensity
1452 projections include 100 or 400 frames, 200 ms/frame. Time is min:sec.

1453 (C) Summarizing diagram illustrating microtubule organization and the motility of PCM clusters in
1454 acentriolar AKAP450 knockout RPE1 cells.

1455 (D) Movement trajectories of PCM clusters in acentriolar AKAP450 knockout cells before and after 1
1456 hr treatment with 5µM dynapyrazole A. 350 frames with a 2 s interval from the same cell were
1457 analyzed. Shaded areas represent the cell body.

1458 (E) Quantification of the length of the trajectories of moving PCM clusters. n=132 (without
1459 dynapyrazole A, from 5 cells) and 111 (after 1 hr dynapyrazole A treatment, from 4 cells) trajectories
1460 were analyzed for each condition. The statistical significance was determined by unpaired two-tailed
1461 Mann-Whitney test in Prism 9.1 (***$p<0.001$). Values represent mean±SD.

1462 (F) Immunofluorescence images of centrinone-treated AKAP450/CAMSAP2 knockout RPE1 cells
1463 transfected with 2FKBP-mCherry-CAMSAP2 and FRB-TagBFP-GCN4-ppKin14 and stained for the
1464 indicated proteins after overnight rapalog treatment. Zooms show the magnification of boxed area.

1465

1466 **Figure 6 – figure supplement 2. Pericentrin is required for PCM clustering in acentriolar AKAP450**
1467 **knockout RPE1 cells**

1468 Time-lapse images of centrinone-treated AKAP450 knockout RPE1 cells stably expressing GFP-
1469 CDK5RAP2 (green) depleted of pericentrin. GFP-CDK5RAP2 is diffusely distributed and does not form
1470 any clear clusters. Microtubule regrowth experiments show random nucleation of microtubules
1471 (labeled with 100nM SiR-tubulin overnight) that remain disorganized. Summarizing diagram shows
1472 PCM clusters and microtubule network in the indicated conditions.

1473

1474 **Figure 7 – figure supplement 1. Inducible CAMSAP2-driven radial microtubule rearrangement in**
1475 **AKAP450/CAMSAP2/p53/pericentrin knockout cell**

1476 (A) Time-lapse images of a centrinone-treated AKAP450/CAMSAP2/p53/pericentrin knockout cell
1477 transiently expressing 2FKBP-mCherry-CAMSAP2 and FRB-GFP-GCN4-ppKin14 imaged for 10 min (100
1478 frames, 6 s interval) prior to treatment with 100 nM rapalog and ~90 min after. Time is hr: min: sec.

1479 (B) Immunofluorescence images of centrinone-treated AKAP450/CAMSAP2/p53/pericentrin knockout
1480 and AKAP450/CAMSAP2/MMG/CDK5RAP2/p53/pericentrin knockout RPE1 cells, stained for the

1481 indicated markers. In the upper row, the cells were neither transfected nor treated with rapalog,
1482 whereas in the other panels, cells were transfected with 2FKBP-mCherry-CAMSAP2 and FRB-HA-
1483 GCN4-ppKin14 and treated with rapalog overnight. Zooms show the magnification of boxed areas.

1484

1485 **Figure 7 – figure supplement 2. Generation of the AKAP450/CAMSAP2/CDK5RAP2/MMG/**
1486 **p53/pericentrin knockout RPE1 cell line**

1487 (A) Diagram illustrating two sgRNA sites targeting p53 exon 4. The green and red boxes indicate the
1488 position of the PAM sites, and the predicted Cas9 cut sites are indicated by scissors. Genotyping results
1489 of the genomic mutation using gel-purified PCR product which covers exon 4 of the p53-encoding gene
1490 in AKAP450/CAMSAP2/MMG/CDK5RAP2/p53 knockout cell line are shown below.

1491 (B) Diagram illustrating the binding sites of p53 antibodies and the position of the mutation induced
1492 in p53-encoding gene.

1493 (C) Immunofluorescence images showing p53 staining in control and
1494 AKAP450/CAMSAP2/MMG/CDK5RAP2/p53 knockout cells.

1495 (D) Diagram illustrating two sgRNA sites targeting pericentrin exon 5. The green and red boxes indicate
1496 the position of the PAM sites, and the predicted Cas9 cut sites are indicated by scissors. Genotyping
1497 results of the genomic mutation using gel-purified PCR product which covers exon 5 of the pericentrin-
1498 encoding gene in AKAP450/CAMSAP2/MMG/CDK5RAP2/p53/pericentrin knockout cell line are shown
1499 below.

1500 (E) Diagram illustrating the binding domain of the pericentrin antibody and the positions of the
1501 mutations induced downstream of the Cas9 cut sites.

1502 (F) Immunofluorescence images showing the confirmation of pericentrin loss in control and
1503 AKAP450/CAMSAP2/MMG/CDK5RAP2/p53/pericentrin knockout cells.

1504 (G) Western blot illustrating the p53 and pericentrin loss in control and
1505 AKAP450/CAMSAP2/MMG/CDK5RAP2/p53/pericentrin knockout cells.

1506 (H) Immunofluorescence images of control and centrinone-treated AKAP450/CAMSAP2/
1507 CDK5RAP2/MMG/p53/pericentrin knockout cells staining microtubule (α-tubulin, red) and
1508 centrosome (CEP192, green). Zooms show magnification of the boxed area.

1509

1510 **Legends to Supplemental Videos**

1511 **Video 1. aMTOC disassembly during nocodazole treatment of acentriolar AKAP450/CAMSAP2**
1512 **knockout cells**

1513 PCM dynamics visualized by stable expression of GFP-CDK5RAP2 (green) in centrinone-treated
1514 AKAP450/CAMSAP2 knockout RPE1 cells. Microtubules were labeled overnight with 100 nM SiR-
1515 tubulin (red). The cell was imaged for ~3.5min (100 frames, 2 s interval) prior to the addition of 10 µM
1516 nocodazole. Time is min: sec.

1517 **Video 2. Depletion of pericentrin inhibits PCM clustering in acentriolar AKAP450/CAMSAP2**
1518 **knockout cells**

1519 A pericentrin-depleted acentriolar AKAP450/CAMSAP2 knockout cell stably expressing GFP-CDK5RAP2
1520 (green) and labeled overnight with 100 nM SiR-tubulin (red) was imaged for ~4.5 min (140 frames, 2 s
1521 time interval) prior to treatment with 10 µM nocodazole. Nocodazole was washed out at ~20 min
1522 (frame 591), when all microtubules were depolymerized. Time is hr: min: sec.

1523 **Video 3. PCM dynamics during nocodazole treatment and washout in acentriolar AKAP450 knockout**
1524 **cells**

1525 An acentriolar AKAP450 knockout RPE1 cell stably expressing GFP-CDK5RAP2 (green) and labeled
1526 overnight with 100 nM SiR-tubulin (red) was imaged for ~7min (200 frames, 2 s interval) prior to
1527 treatment with 10 µM nocodazole. Nocodazole was washed out at ~27 min (frame 801) when all
1528 microtubules were depolymerized. Time is min: sec.

1529 **Video 4. PCM dynamics in acentriolar AKAP450 knockout cells are inhibited by dynapyrazole**

1530 An acentriolar AKAP450 knockout RPE1 cell stably expressing GFP-CDK5RAP2 (green) and labeled
1531 overnight with 100 nM SiR-tubulin (red) was imaged for ~12 min (350 frames, 2 s interval) prior to the
1532 dynapyrazole treatment, treated with 5 µM Dynapyrazole A for 1h, and then the same cell was imaged
1533 for ~12 min. Time is min: sec.

1534 **Video 5. Depletion of pericentrin inhibits PCM clustering in acentriolar AKAP450 knockout cells**

1535 A pericentrin-depleted acentriolar AKAP450 knockout cell stably expressing GFP-CDK5RAP2 (green)
1536 and labeled overnight with 100 nM SiR-tubulin (red) was imaged for ~3 min (90 frames, 2 s time
1537 interval) prior to treatment with 10 µM nocodazole. Nocodazole was washed out at ~23 min (frame
1538 701) when all microtubules were depolymerized. Time is hr: min: sec.

1539 **Video 6. Inducible CAMSAP2-driven radial microtubule rearrangement in an**
1540 **AKAP450/CAMSAP2/p53/pericentrin knockout cell**

1541 An acentriolar AKAP450/CAMSAP2/p53/pericentrin knockout cell transiently expressing 2FKBP-
1542 mCherry-CAMSAP2 (red) and FRB-GFP-GCN4-ppKin14 (green) was imaged for 10 min (100 frames, 6 s
1543 interval) prior to treatment with 100 nM rapalog. Subsequently, the cell was imaged for ~1 hr and 35
1544 min after rapalog addition. Time is hr: min: sec.

1545

1546 **Source data 1**

1547 **Uncropped Western blots shown in this manuscript**

1548 (A,B) Western blots showing that NEDD1 and CEP192 are present in centrinone-treated
1549 AKAP450/CAMSAP2 knockout cells shown in Figure 2 – figure supplement 1A.

1550 (C-J) Western blots showing the depletion of indicated proteins in centrinone-treated
1551 AKAP450/CAMSAP2 knockout cells shown in Figure 2 – figure supplement 1B.

1552 (K) Western blot showing that 3 hr treatment with dynaprazole A does not affect the expression of
1553 the endogenous dynein heavy chain and the dynactin large subunit p150Glued in centrinone-treated
1554 AKAP450/CAMSAP2 knockout cells shown in Figure 4D.

1555

1556 **Source data 2**

1557 **Uncropped Western blots shown in this manuscript**

1558 (A) Western blots showing the knockout of p53 from AKAP450/CAMSAP2 knockout cell line shown in
1559 Figure 2 – figure supplement 2F.

1560 (B) Western blots showing the knockout of pericentrin from AKAP450/CAMSAP2/p53 knockout cell
1561 line shown in Figure 2 – figure supplement 2K.

1562 (C) Western blots showing the knockout of AKAP450 and CAMSAP2 from EB1/EB3 mutant RPE1 cell
1563 line shown in Figure 2 – figure supplement 4B.

1564 (D) Western blots showing the knockout of pericentrin in AKAP450/CAMSAP2/CDK5RAP2/MMG/p53/
1565 knockout cell line shown in Figure 7 – figure supplement 2G.

1566 ***Key reagent or resource table***

Reagent type (species) or resource	Designation	Source or reference	Identifiers	Additional information
Antibody	anti-Pericentrin (mouse monoclonal)	Abcam	Abcam Cat# ab28144, RRID:AB_2160664	(1:500) for IF
Antibody	anti-Pericentrin (rabbit polyclonal)	Abcam	Abcam Cat# ab4448, RRID:AB_304461	(1:500) for IF; (1:1000) for WB
Antibody	anti-CDK5RAP2 (rabbit polyclonal)	Bethyl Laboratories	Bethyl Cat# A300-554A, RRID:AB_477974	(1:300) for IF; (1:1000) for WB
Antibody	anti-γ-tubulin (mouse monoclonal)	Sigma-Aldrich	Sigma-Aldrich: T6557; RRID:AB_477584	(1:300) for IF; (1:2000) for WB
Antibody	anti-γ-tubulin (rabbit polyclonal)	Sigma-Aldrich	Sigma-Aldrich:T3559, RRID:AB_477575	(1:300) for IF
Antibody	anti-NEDD1 (mouse monoclonal)	Abnova	Abnova Corporation Cat# H00121441-M05, RRID:AB_534956	(1:300) for IF
Antibody	anti-NEDD1 (rabbit polyclonal)	Rockland	Rockland Cat# 109-401-C38S, RRID:AB_10893219	(1:1000) for WB
Antibody	anti-Ninein (rabbit polyclonal)	BETHYL	Bethyl Cat# A301-504A, RRID:AB_999627	(1:300) for IF; (1:2000) for WB
Antibody	anti-Ninein (mouse monoclonal)	Santa Cruz Biotechnology	Santa Cruz Biotechnology Cat# sc-376420, RRID:AB_11151570	(1:300) for IF
Antibody	anti-Dynein HC (rabbit polyclonal)	Santa Cruz Biotechnology	Santa Cruz Biotechnology Cat# sc-9115, RRID:AB_2093483	(1:300) for IF; (1:500) for WB
Antibody	anti-p150Glued (mouse monoclonal)	BD Biosciences	BD Biosciences Cat# 610473, RRID:AB_397845	(1:100) for IF; (1:500) for WB
Antibody	anti-PCM1 (mouse monoclonal)	Santa Cruz Biotechnology	Santa Cruz Biotechnology Cat# sc-398365, RRID:AB_2827155	(1:300) for IF
Antibody	anti-PCM1 (rabbit polyclonal)	Bethyl Laboratories	Bethyl Cat# A301-150A, RRID:AB_873100	(1:300) for IF
Antibody	anti-AKAP450 (mouse monoclonal)	BD Biosciences	BD Biosciences Cat# 611518, RRID:AB_398978	(1:500) for WB
Antibody	anti-CAMSAP2 (rabbit polyclonal)	Novus	Novus:NBP1-21402; RRID:AB_1659977	(1:200) for IF; (1:1000) for WB
Antibody	anti-p53 (mouse monoclonal)	Santa Cruz Biotechnology	Santa Cruz Biotechnology Cat# sc-126, RRID:AB_628082	(1:300) for IF; (1:1000) for WB
Antibody	anti-p53 (rabbit polyclonal)	BETHYL	Bethyl Cat# A300-248A, RRID:AB_263349	(1:300) for IF
Antibody	anti-EB1 (mouse monoclonal)	BD Biosciences	BD Biosciences:610535; RRID:AB_397892	(1:400) for IF

Antibody	anti-EB3 (rabbit polyclonal)	Martin, et al., 2018;		(1:300) for IF
Antibody	anti-Centrin (mouse monoclonal)	Millipore	Millipore Cat# 04-1624, RRID:AB_10563501	(1:500) for IF
Antibody	anti-CEP120 (rabbit polyclonal)	Thermo Fisher Scientific	Thermo Fisher Scientific Cat# PA5-55985, RRID:AB_2639665	(1:300) for IF
Antibody	anti-CEP135 (rabbit polyclonal)	Sigma-Aldrich	Sigma-Aldrich:SAB4503685; RRID:AB_10746232	(1:300) for IF
Antibody	anti-CEP152 (rabbit polyclonal)	Abcam	Abcam, Cat # ab183911	(1:300) for IF; (1:1000) for WB
Antibody	anti-CEP170 (mouse monoclonal)	Thermo Fisher Scientific	Thermo Fisher Scientific Cat# 41-3200, RRID:AB_2533502	(1:200) for IF
Antibody	anti-CEP192 (rabbit polyclonal)	Bethyl Laboratories	Bethyl Cat# A302-324A, RRID:AB_1850234	(1:300) for IF; (1:1000) for WB
Antibody	anti-GM130 (mouse monoclonal)	BD Biosciences	BD Biosciences:610823; RRID:AB_398142	(1:300) for IF; (1:2000) for WB
Antibody	anti-α-tubulin YL1/2 (rat monoclonal)	Pierce	Pierce: MA1-80017; RRID:AB_2210201	(1:300) for IF
Antibody	anti-α-tubulin (mouse monoclonal)	Sigma-Aldrich	Sigma-Aldrich:T5168; RRID:AB_477579	(1:400) for IF
Antibody	anti-α-tubulin (rabbit monoclonal antibody)	Abcam	Abcam Cat# ab52866, RRID:AB_869989	(1:800) for IF
Antibody	Anti-β-tubulin (mouse monoclonal)	Sigma-Aldrich	Sigma-Aldrich Cat# T8660, RRID:AB_477590	(1:2000) for WB
Antibody	anti-CLASP1 (rabbit polyclonal)	(Akhmanova et al., 2001)		(1:400) for IF
Antibody	anti-CLASP2 (rabbit polyclonal)	(Akhmanova et al., 2001)		(1:400) for IF
Antibody	anti-CLIP-115 #2238 (rabbit polyclonal)	(Akhmanova et al., 2001)		(1:300) for IF
Antibody	anti-CLIP-170 #2360 (rabbit polyclonal)	(Akhmanova et al., 2001)		(1:300) for IF
Antibody	anti-ch-TOG (rabbit polyclonal)	(Charrasse et al., 1998)	Dr. Lynne Cassimeris (Lehigh University, USA)	(1:200) for IF
Antibody	anti-CPAP (rabbit polyclonal)	(Kohlmaier et al., 2009)	Dr. Pierre Gönczy (EPFL, Switzerland)	(1:200) for IF
Antibody	anti-CP110 (rabbit monoclonal)	Proteintech	Proteintech Cat# 12780-1-AP, RRID:AB_10638480	(1:300) for IF
Antibody	anti-KIF1C (rabbit polyclonal)	Cytoskeleton	Cytoskeleton Cat# AKIN11-A, RRID:AB_10708792	(1:300) for IF
Antibody	anti-KIF2A (rabbit polyclonal)	(Ganem and Compton, 2004)	Dr. Duane Compton (Geisel School of Medicine at Dartmouth, USA)	(1:300) for IF

Antibody	anti-HAUS2 (rabbit polyclonal)	(Lawo et al., 2009)	Dr. Laurence Pelletier (Lunenfeld-Tanenbaum Research Institute, Canada)	(1:200) for IF
Antibody	anti-BICD2 (rabbit polyclonal)	(Hoogenraad et al., 2003)		(1:2500) for WB
Antibody	anti-Actin (mouse monoclonal)	Millipore	Millipore Cat# MAB1501, RRID:AB_2223041	(1:4000) for WB
Antibody	anti-Ku80 (mouse monoclonal)	BD Biosciences	BD Biosciences Cat# 611360, RRID:AB_398882	(1:2000) for WB
Antibody	anti-LaminA/C (mouse monoclonal)	BD Biosciences	BD Biosciences Cat# 612162, RRID:AB_399533	(1:400) for IF
Antibody	anti-Cytochrome C (mouse monoclonal)	BD Biosciences	BD Biosciences Cat# 556432, RRID:AB_396416	(1:300) for IF
Antibody	anti-Calnexin (rabbit polyclonal)	Abcam	Abcam Cat# ab22595, RRID:AB_2069006	(1:300) for IF
Antibody	Anti-Lamtor4 (rabbit monoclonal)	Cell Signaling (CST)/Bioke	Cell Signaling Technology Cat# 12284, RRID:AB_2797870	(1:800) for IF
	Anti-Tom20 (mouse monoclonal)	BD Biosciences	BD Biosciences Cat# 612278, RRID:AB_399595	(1:200) for IF
Antibody	IRDye 800CW/680LT secondaries	Li-Cor Biosciences	LI-COR Biosciences Cat# 926-32219, RRID:AB_1850025' LI-COR Biosciences Cat# 926-68020, RRID:AB_10706161; LI-COR Biosciences Cat# 926-32211, RRID:AB_621843; LI-COR Biosciences Cat# 926-68021, RRID:AB_10706309	(1:5000) for WB
Antibody	Alexa Fluor 405–, 488–, and 594– secondaries	Molecular Probes/ Thermo Fisher Scientific	Molecular Probes Cat# A-11007, RRID:AB_141374; Cat# A-11034, RRID:AB_2576217; Cat# A32723, RRID:AB_2633275; Cat# A-31553, RRID:AB_221604; Cat# A-11029, RRID:AB_138404; Cat# A-11032, RRID:AB_2534091; Cat# A-11006, RRID:AB_141373; Thermo Fisher Scientific Cat# A-11012, RRID:AB_2534079	(1:500) for IF
Sequence-based reagent	siRNA against PCNT #1	(Gavilan et al., 2018)	5'-AAAAGCUCUGAUUUAUCAAAAGAAG-3'	
Sequence-based reagent	siRNA against PCNT #2	(Gavilan et al., 2018)	5'-UGAUUGGACGUCAUCCAAUGAGAAA-3'	

Sequence-based reagent	siRNA against PCNT #3	(Tibelius et al., 2009)	5'-GCAGCUGAGCUGAAGGAGA-3'	
Sequence-based reagent	siRNA against CDK5RAP2	(Fong et al., 2008)	5'-UGGAAGAUCUCCUAACUAA-3'	
Sequence-based reagent	siRNA against γ-tubulin #1	(Luders et al., 2006)	5'-GGAGGACAUGUUCAAGGAA-3'	
Sequence-based reagent	siRNA against γ-tubulin #2	(Vinopal et al., 2012)	5'-CGCAUCUCUUUCUCAUAU-3'	
Sequence-based reagent	siRNA against Ninein	(Goldspink et al., 2017)	5'-CGGUACAAUGAGUGUAGAAUU-3'	
Sequence-based reagent	siRNA against PCM1	(Wang et al., 2013)	5'-UCAGCUUCGUGAUUCUCAG-3'	
Sequence-based reagent	siRNA against CEP152	(Cizmecioglu et al., 2010; Komarova et al., 2005)	5'-GCGGAUCCAACUGGAAAUCUA-3'	
Sequence-based reagent	siRNA against CEP120	(Ganem et al., 2005; Lin et al., 2013)	5'-AAUAUAUCUUCUUGCAUCUCCUUCC-3'	
Sequence-based reagent	siRNA against CEP192	(Sonnen et al., 2013)	5'-CAGAGGAAUCAAUAAUAAA -3'	
Sequence-based reagent	siRNA against NEDD1 #1	(Luders et al., 2006)	5'-GCAGACAUGUGUCAAUUUA-3'	
Sequence-based reagent	siRNA against NEDD1 #2	(Haren et al., 2006)	5'-GGGCAAAAGCAGACAUGUG-3'	
Sequence-based reagent	siRNA against DHC #1	(Splinter et al., 2010)	5'-CGUACUCCCGUGAUUGAUG-3'	
Sequence-based reagent	siRNA against DHC #2	(Splinter et al., 2010)	5'-GCCAAAAGUUACAGACUUU-3'	
Sequence-based reagent	siRNA against CAMSAP2	(Jiang et al., 2014)	5'-GUACUGGAUAAAUAAGGUA-3'	
Sequence-based reagent	siRNA against CEP170	(Stolz et al., 2015)	5'-GAAGGAAUCCUCCAAGUCA-3'	
Sequence-based reagent	siRNA against CPAP	(Tang et al., 2009)	5'-AGAAUUAGCUCGAAUAGAA-3'	
Sequence-based reagent	siRNA against CLIP170 #1	(Lansbergen et al., 2004; Mimori-Kiyosue et al., 2005)	5'-GGAGAAGCAGCAGCACAUU-3'	
Sequence-based reagent	siRNA against CLIP170 #2	(Lansbergen et al., 2004; Mimori-Kiyosue et al., 2005)	5'-UGAAGAUGUCAGGAGAUAA-3'	

Sequence-based reagent	siRNA against CLIP115 #1	(Lansbergen et al., 2004)	5'-GGCACAGCAUGAGCAGUAU-3'	
Sequence-based reagent	siRNA against CLIP115 #2	(Lansbergen et al., 2004)	5'-CUGGAAAUCCAAGCUGGAC-3'	
Sequence-based reagent	siRNA against ch-TOG:	(Cassimeris and Morabito, 2004; Lansbergen et al., 2004)	5'-GAGCCCAGAGUGGUCCAAA-3'	
Sequence-based reagent	siRNA against EB1	(Grigoriev et al., 2008; Lansbergen et al., 2004)	5'-AUUCCAAGCUAAGCUAGAA-3'	
Sequence-based reagent	siRNA against EB3	(Cassimeris and Morabito, 2004; Komarova et al., 2005)	5'-CUAUGAUGGAAAGGAUUAC-3'	
Sequence-based reagent	siRNA against KIF2A	(Ganem et al., 2005; Grigoriev et al., 2008)	5'-GGCAAAGAGAUUGACCUGG-3'	
Sequence-based reagent	siRNA against CP110	(Cizmecioglu et al., 2010; Spektor et al., 2007)	5'-AAGCAGCAUGAGUAUGCCAGU-3'	
Sequence-based reagent	siRNA against Luciferase	(Lansbergen et al., 2004; Lin et al., 2013)	5'-CGUACGCGGAAUACUUCGA-3'	
Sequence-based reagent	sgRNA target CAMSAP2	(Lansbergen et al., 2004; Wu et al., 2016)	5'-gCATGATCGATACCCTCATGA-3	
Sequence-based reagent	sgRNA target p53 e2 #1	This study	5′-gCGTCGAGCCCCCTCTGAGTC-3′;	
Sequence-based reagent	sgRNA target p53 e4 #2	This study	5′-gCCATTGTTCAATATCGTCCG-3′;	
Sequence-based reagent	sgRNA target p53 e4 #3	This study	5′-gTCCATTGCTTGGGACGGCAA-3′;	
Sequence-based reagent	sgRNA target PCNT e5-1 #1	This study	5′-gAGACGGCATTGACGGAGCTG-3′;	
Sequence-based reagent	sgRNA target PCNT e5-2 #2	This study	5′-GCTCAACAGCCGGCGTGCCC-3′;	

Sequence-based reagent	p53 KO sequencing primer F	This study	5′-TCAGACACTGGCATGGTGTT-3′;	
Sequence-based reagent	p53 KO sequencing primer R	This study	5′-AGAAATGCAGGGGGATACGG-3′;	
Sequence-based reagent	PCNT KO sequencing primer F	This study	5′-ATACAGCGAGGGAATTCGGG-3′;	
Sequence-based reagent	PCNT KO sequencing primer R	This study	5′-TAGAATGCCCACACCGAGC-3′;	
Chemical compound	Centrinone B	Tocris Bioscience	Tocris Bioscience Cat # 5690	125nM
Chemical compound	Nocodazole	Sigma-Aldrich	Sigma-Aldrich, Cat # M1404-10MG	10μM
Chemical compound	Rapalog (A/C Heterodimerizer)	Takara	Takara, Cat # 635056	50nM (fixation), 100nM (live imaging).
Chemical compound	Dynapyrazole A	Sigma-Aldrich	Sigma-Aldrich, Cat # SML2127-25MG	5μM
Chemical compound	BI2536	Selleckchem	Selleckchem, Cat # S1109	500nM
Chemical compound	SiR-tubulin	Tebu-bio	Tebu-bio, Cat # SC002	100nM
Software, algorithm	ImageJ radiality plugin	https://github.com/ekatrukha/radialitymap	Katrukha, 2017. radialitymap. Github. https://github.com/ekatrukha/radialitymap cf1e78f	
Recombinant DNA reagent	pLVX-IRES-puro (plasmid)	Clontech		
Recombinant DNA reagent	pB80-FRB-TagBFP-GCN4-ppKin14 (plasmid)	This work		
Recombinant DNA reagent	pB80-FRB-GFP-GCN4-ppKin14 (plasmid)	This work		
Recombinant DNA reagent	pB80-FRB-HA-GCN4-ppKin14 (plasmid)	This work		
Recombinant DNA reagent	2FKBP-mCherry-CAMSAP2 (plasmid)	This work		

Recombinant DNA reagent	GFP-PCNT (plasmid)	This work		
Recombinant DNA reagent	GST-DmKHC(1-421)-mNeonGreen (plasmid)	This work		
Cell line (Homo sapiens)	hTERT-RPE-1	ATCC	CRL-4000	
Cell line (Homo sapiens)	hTERT-RPE-1 AKAP450 knockout	(Wu et al., 2016)		
Cell line (Homo sapiens)	hTERT-RPE-1 AKAP450/CAMSAP2 knockout	(Wu et al., 2016)		
Cell line (Homo sapiens)	hTERT-RPE-1 AKAP450/CAMSAP2/p53 knockout	This work		
Cell line (Homo sapiens)	hTERT-RPE-1 AKAP450/CAMSAP2/p53/Pericentrin knockout	This work		
Cell line (Homo sapiens)	hTERT-RPE-1 AKAP450/CAMSAP2/EB1/EB3 mutant	This work		
Cell line (Homo sapiens)	hTERT-RPE-1 AKAP450/CAMSAP2/CDK5RAP2/MMG/p53/Pericentrin knockout	This work		
Cell line (Homo sapiens)	HEK 293T	ATCC	CRL-11268	

Figure 1

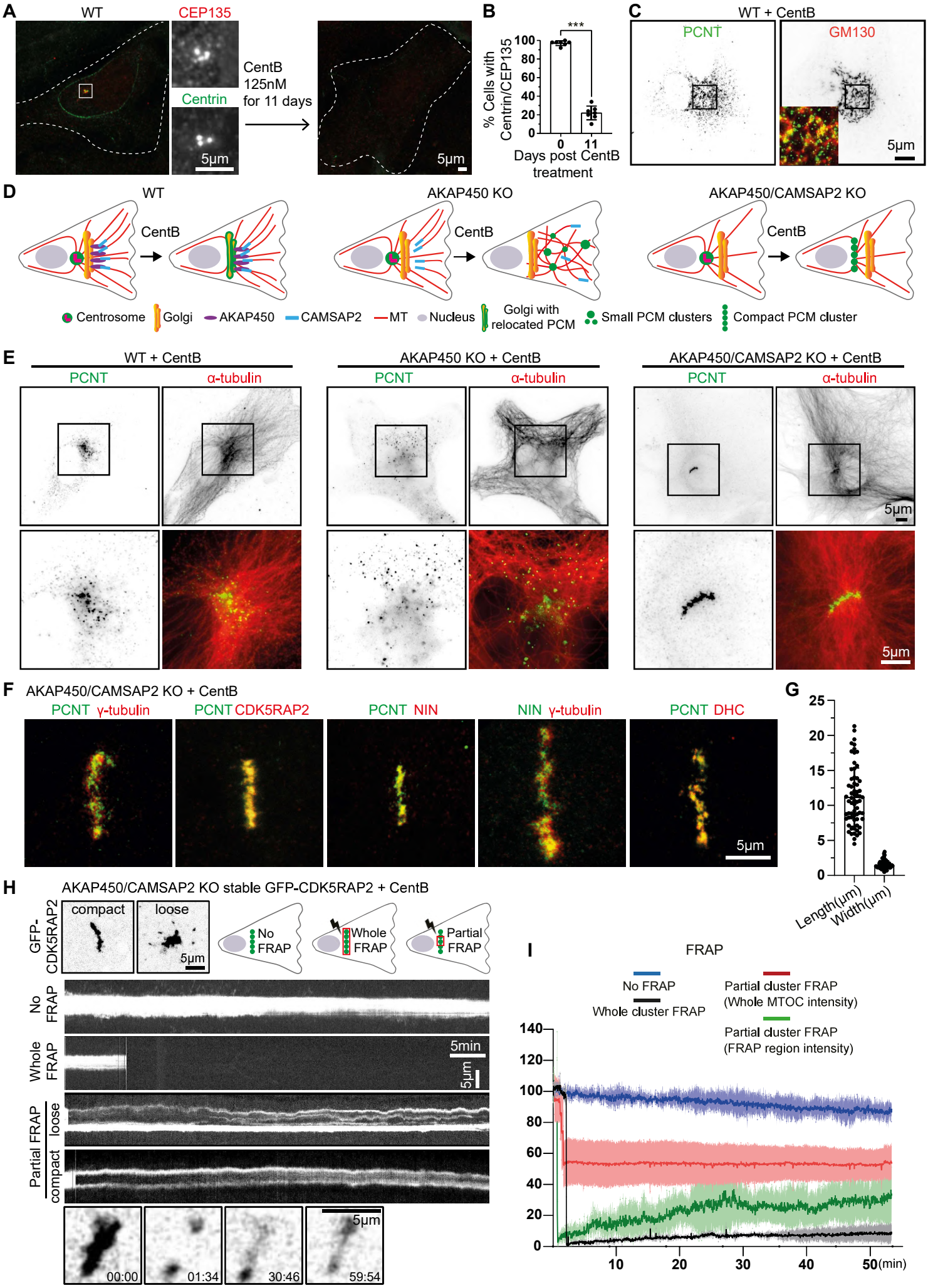
A
WT
CEP135
Centrin
5µm
CentB
125nM
for 11 days
5µm
B
***
% Cells with Centrin/CEP135
100
80
60
40
20
0
0
11
Days post CentB treatment
C
WT + CentB
PCNT
GM130
5µm
D
WT
AKAP450 KO
AKAP450/CAMSAP2 KO
CentB
Centrosome
Golgi
AKAP450
CAMSAP2
MT
Nucleus
Golgi with relocated PCM
Small PCM clusters
Compact PCM cluster
E
WT + CentB
AKAP450 KO + CentB
AKAP450/CAMSAP2 KO + CentB
PCNT
α-tubulin
5µm
F
AKAP450/CAMSAP2 KO + CentB
PCNT γ-tubulin
PCNT CDK5RAP2
PCNT NIN
NIN γ-tubulin
PCNT DHC
5µm
G
25
20
15
10
5
0
Length(µm)
Width(µm)
H
AKAP450/CAMSAP2 KO stable GFP-CDK5RAP2 + CentB
GFP-CDK5RAP2
compact
loose
5µm
No FRAP
Whole FRAP
Partial FRAP
No FRAP
Whole FRAP
5min
5µm
Partial FRAP
loose
compact
5µm
00:00
01:34
30:46
59:54
I
FRAP
No FRAP
Whole cluster FRAP
Partial cluster FRAP (Whole MTOC intensity)
Partial cluster FRAP (FRAP region intensity)
140
120
100
80
60
40
20
0
10
20
30
40
50(min)

Figure 2

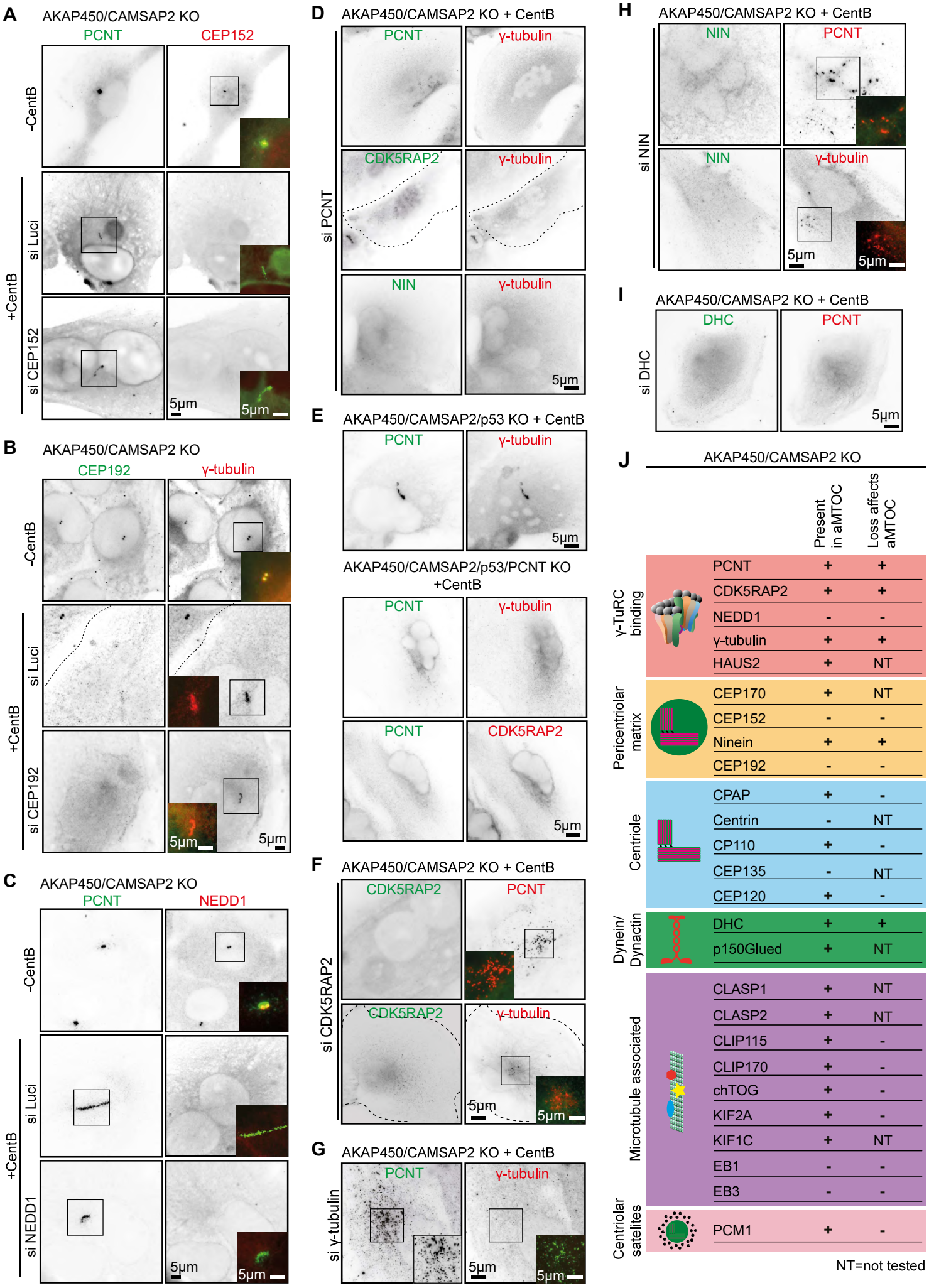
A
AKAP450/CAMSAP2 KO
PCNT
CEP152
-CentB
+CentB
si Luci
si CEP152
5µm
5µm
B
AKAP450/CAMSAP2 KO
CEP192
γ-tubulin
-CentB
+CentB
si Luci
si CEP192
5µm
5µm
C
AKAP450/CAMSAP2 KO
PCNT
NEDD1
-CentB
+CentB
si Luci
si NEDD1
5µm
5µm
D
AKAP450/CAMSAP2 KO + CentB
PCNT
γ-tubulin
CDK5RAP2
γ-tubulin
NIN
γ-tubulin
si PCNT
5µm
E
AKAP450/CAMSAP2/p53 KO + CentB
PCNT
γ-tubulin
5µm
AKAP450/CAMSAP2/p53/PCNT KO
+CentB
PCNT
γ-tubulin
PCNT
CDK5RAP2
5µm
F
AKAP450/CAMSAP2 KO + CentB
CDK5RAP2
PCNT
CDK5RAP2
γ-tubulin
si CDK5RAP2
5µm
5µm
G
AKAP450/CAMSAP2 KO + CentB
PCNT
γ-tubulin
si γ-tubulin
5µm
5µm
H
AKAP450/CAMSAP2 KO + CentB
NIN
PCNT
NIN
γ-tubulin
si NIN
5µm
5µm
I
AKAP450/CAMSAP2 KO + CentB
DHC
PCNT
si DHC
5µm
J
AKAP450/CAMSAP2 KO
Present in aMTOC
Loss affects aMTOC
γ-TuRC binding
PCNT + +
CDK5RAP2 + +
NEDD1 - -
γ-tubulin + +
HAUS2 + NT
Pericentriolar matrix
CEP170 + NT
CEP152 - -
Ninein + +
CEP192 - -
Centriole
CPAP + -
Centrin - NT
CP110 + -
CEP135 - NT
CEP120 + -
Dynein/ Dynactin
DHC + +
p150Glued + NT
Microtubule associated
CLASP1 + NT
CLASP2 + NT
CLIP115 + -
CLIP170 + -
chTOG + -
KIF2A + -
KIF1C + NT
EB1 - -
EB3 - -
Centriolar satelites
PCM1 + -
NT=not tested

Figure 3

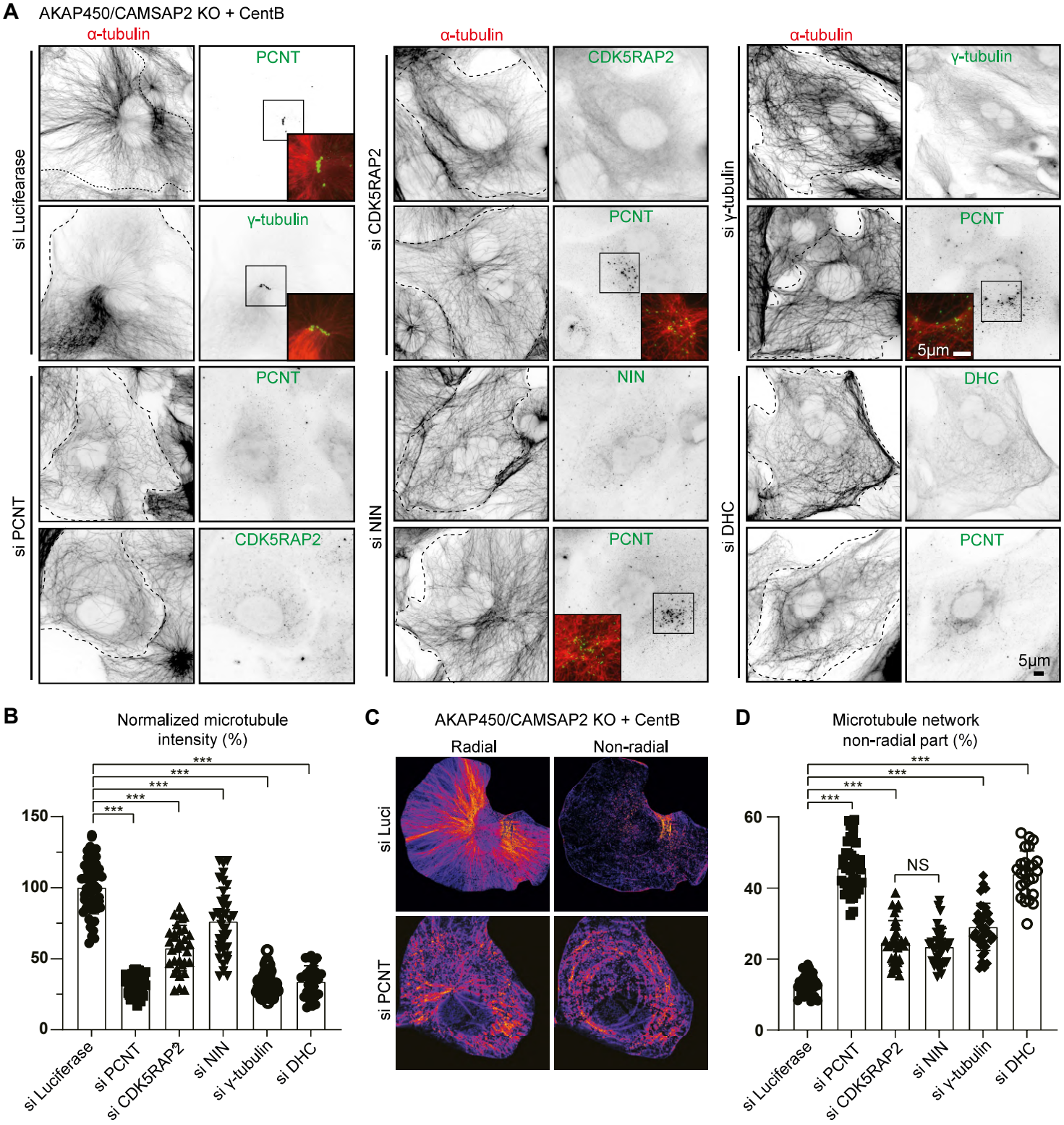
A
AKAP450/CAMSAP2 KO + CentB
α-tubulin
PCNT
γ-tubulin
CDK5RAP2
NIN
DHC
si Lucifearase
si CDK5RAP2
si γ-tubulin
si PCNT
si NIN
si DHC
5µm
B
Normalized microtubule intensity (%)
150
100
50
0
***
si Luciferase
si PCNT
si CDK5RAP2
si NIN
si γ-tubulin
si DHC
C
AKAP450/CAMSAP2 KO + CentB
Radial
Non-radial
si Luci
si PCNT
D
Microtubule network non-radial part (%)
60
40
20
0
NS

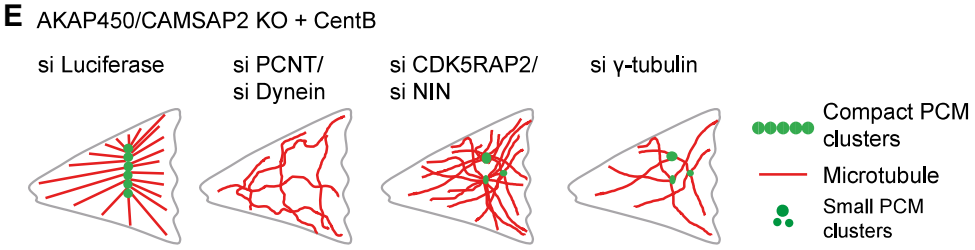
E
AKAP450/CAMSAP2 KO + CentB
si Luciferase
si PCNT/
si Dynein
si CDK5RAP2/
si NIN
si γ-tubulin
Compact PCM clusters
Microtubule
Small PCM clusters

Figure 4

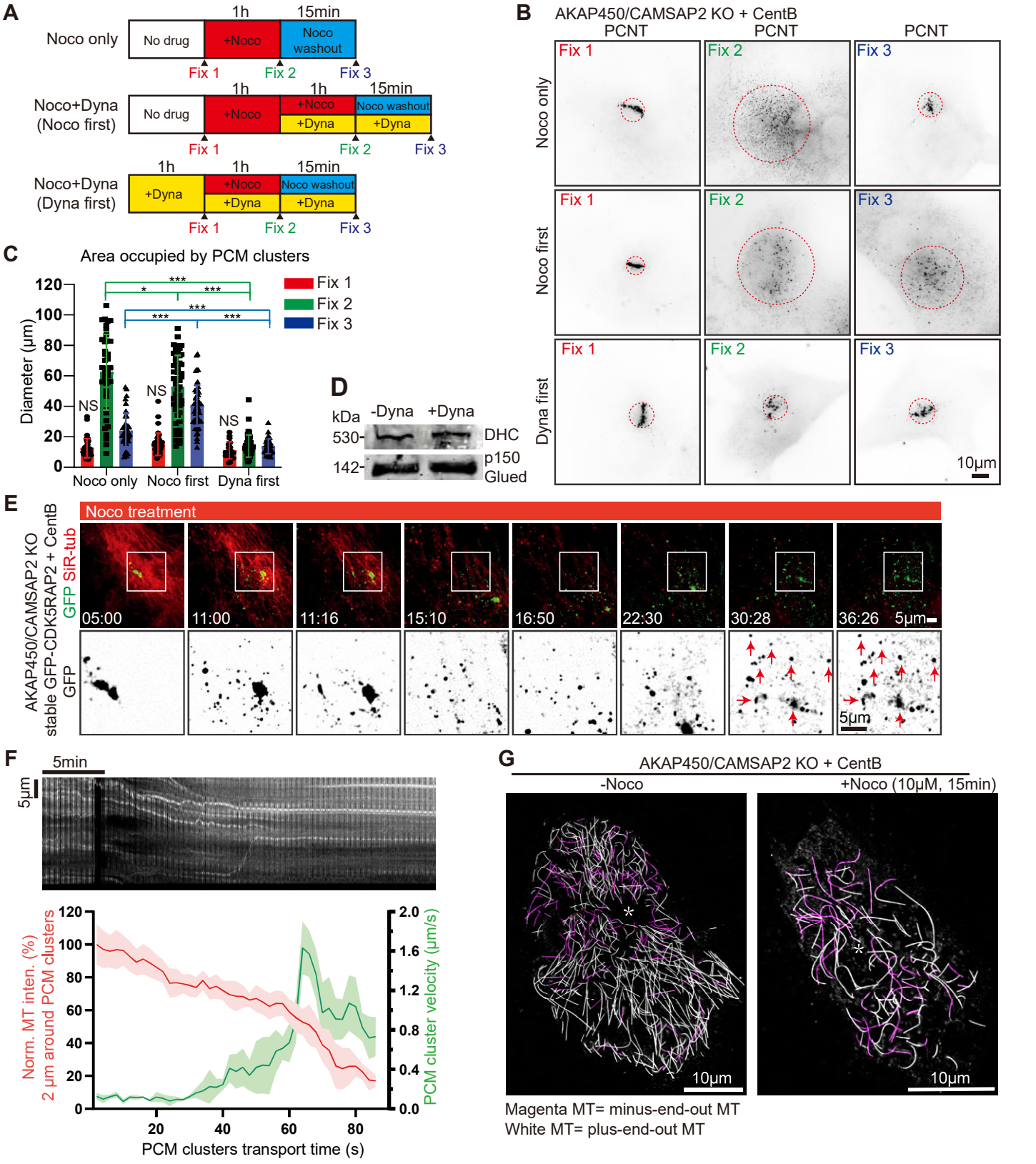
A
Noco only
No drug
1h
+Noco
15min
Noco washout
Fix 1
Fix 2
Fix 3
Noco+Dyna (Noco first)
+Dyna
Noco+Dyna (Dyna first)
B
AKAP450/CAMSAP2 KO + CentB
PCNT
Noco only
Noco first
Dyna first
10μm
C
Area occupied by PCM clusters
Diameter (μm)
NS
Noco only
Noco first
Dyna first
D
kDa
-Dyna
+Dyna
530-
142-
DHC
p150 Glued
E
Noco treatment
AKAP450/CAMSAP2 KO stable GFP-CDK5RAP2 + CentB
GFP SiR-tub
GFP
05:00
11:00
11:16
15:10
16:50
22:30
30:28
36:26
5μm
F
5min
5μm
Norm. MT inten. (%) 2 μm around PCM clusters
PCM cluster velocity (μm/s)
PCM clusters transport time (s)
G
AKAP450/CAMSAP2 KO + CentB
-Noco
+Noco (10μM, 15min)
10μm
Magenta MT= minus-end-out MT
White MT= plus-end-out MT
H
AKAP450/CAMSAP2 KO
+CentB
+Noco
Early stage
Late stage
+Dyna(treat first)
+Noco
Centrosome
MT
Nucleus
Compact PCM cluster
Small PCM clusters
Mobile PCM
Immobile PCM

Figure 5

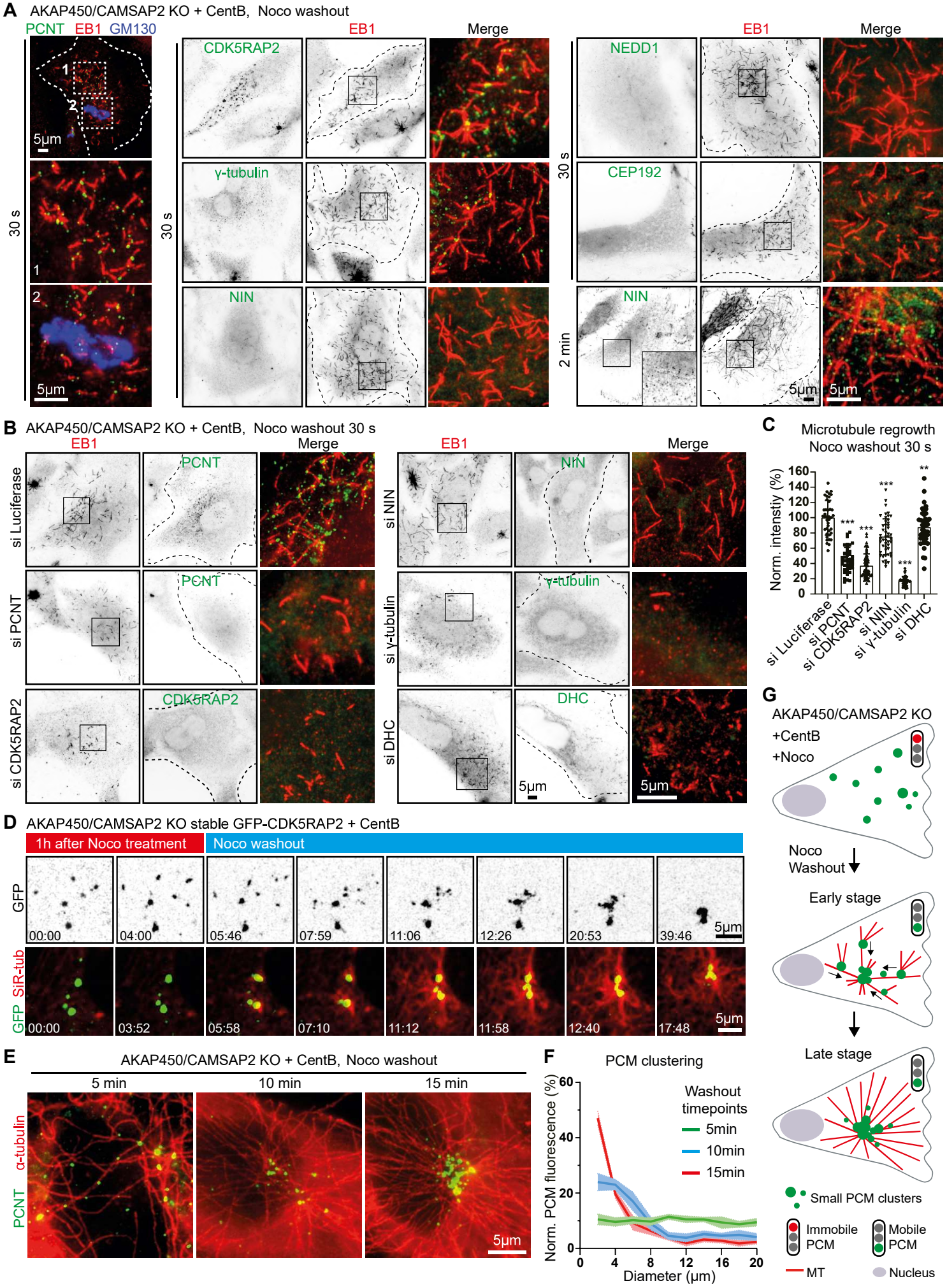
A
AKAP450/CAMSAP2 KO + CentB, Noco washout
PCNT EB1 GM130
EB1
Merge
CDK5RAP2
γ-tubulin
NIN
NEDD1
CEP192
30 s
2 min
5µm
B
AKAP450/CAMSAP2 KO + CentB, Noco washout 30 s
si Luciferase
si PCNT
si CDK5RAP2
si NIN
si γ-tubulin
si DHC
PCNT
DHC
C
Microtubule regrowth
Noco washout 30 s
Norm. intenstiy (%)
si Luciferase
si PCNT
si CDK5RAP2
si NIN
si γ-tubulin
si DHC
D
AKAP450/CAMSAP2 KO stable GFP-CDK5RAP2 + CentB
1h after Noco treatment
Noco washout
GFP
SiR-tub
00:00
04:00
05:46
07:59
11:06
12:26
20:53
39:46
03:52
05:58
07:10
11:12
11:58
12:40
17:48
E
AKAP450/CAMSAP2 KO + CentB, Noco washout
5 min
10 min
15 min
α-tubulin
PCNT
F
PCM clustering
Washout timepoints
5min
10min
15min
Norm. PCM fluorescence (%)
Diameter (µm)
G
AKAP450/CAMSAP2 KO
+CentB
+Noco
Noco Washout
Early stage
Late stage
Small PCM clusters
Immobile PCM
Mobile PCM
MT
Nucleus

Figure 6

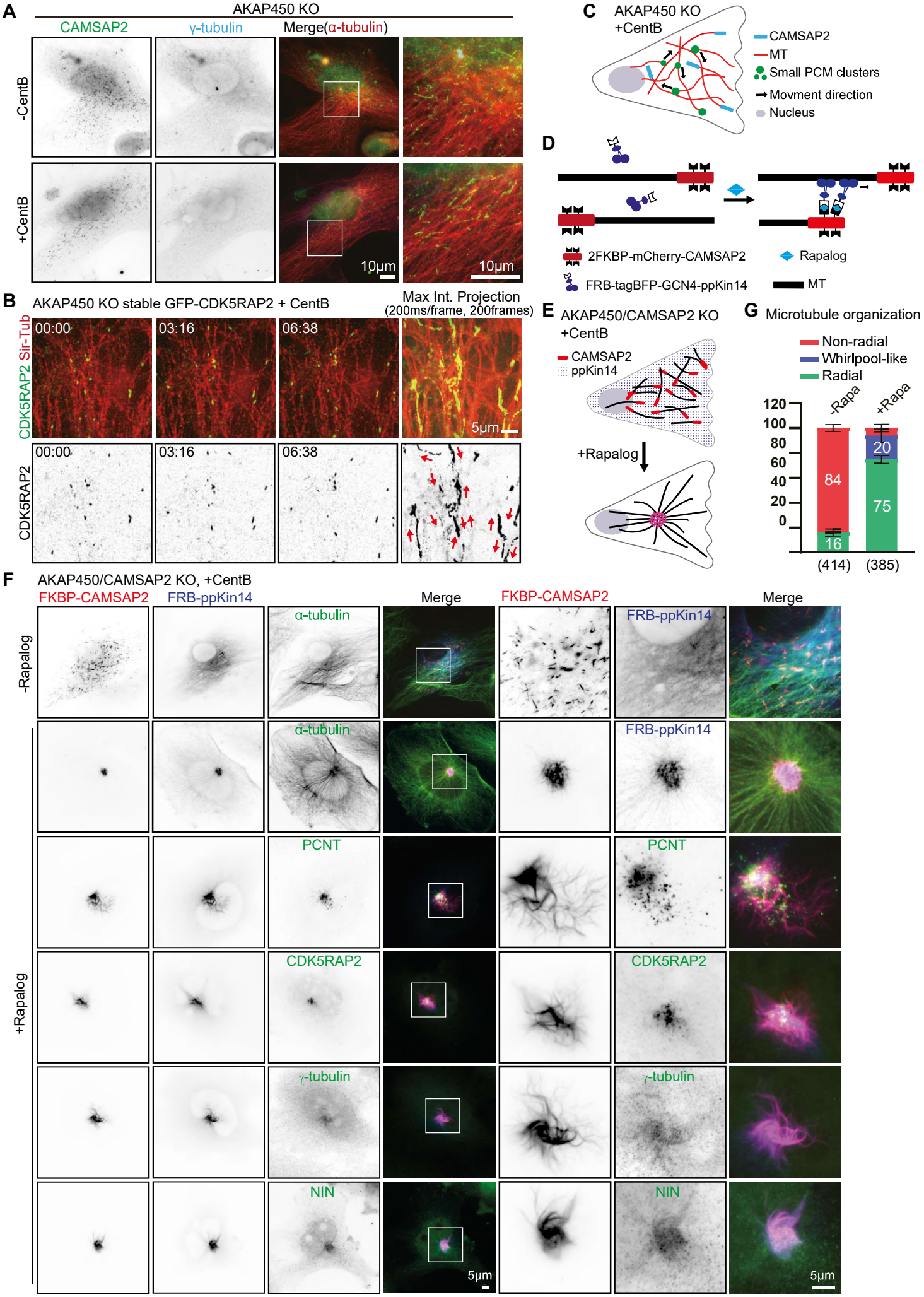
A
AKAP450 KO
CAMSAP2
γ-tubulin
Merge(α-tubulin)
-CentB
+CentB
10μm
10μm
B
AKAP450 KO stable GFP-CDK5RAP2 + CentB
Max Int. Projection
(200ms/frame, 200frames)
CDK5RAP2 Sir-Tub
00:00
03:16
06:38
5μm
CDK5RAP2
C
AKAP450 KO
+CentB
CAMSAP2
MT
Small PCM clusters
Movment direction
Nucleus
D
2FKBP-mCherry-CAMSAP2
Rapalog
FRB-tagBFP-GCN4-ppKin14
MT
E
AKAP450/CAMSAP2 KO
+CentB
CAMSAP2
ppKin14
+Rapalog
G
Microtubule organization
Non-radial
Whirlpool-like
Radial
-Rapa
+Rapa
120
100
80
60
40
20
0
84
20
75
16
(414)
(385)
F
AKAP450/CAMSAP2 KO, +CentB
FKBP-CAMSAP2
FRB-ppKin14
Merge
-Rapalog
+Rapalog
α-tubulin
PCNT
CDK5RAP2
γ-tubulin
NIN
5μm

Figure 7

A AKAP450/CAMSAP2/p53/PCNT KO, +CentB

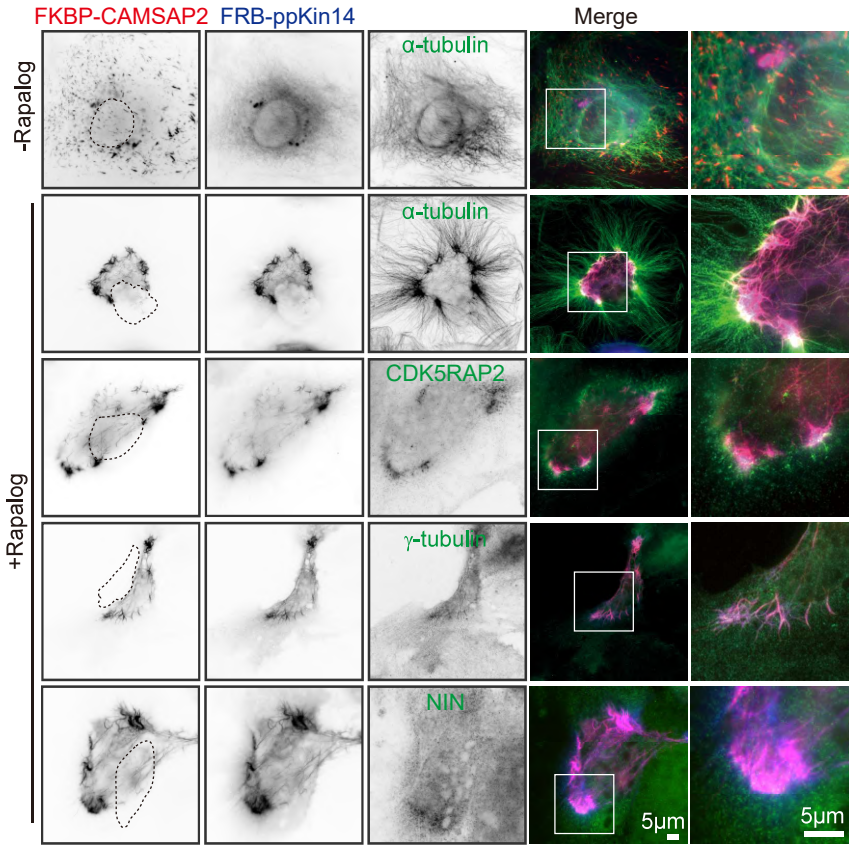

B AKAP450/CAMSAP2/p53/PCNT KO, +CentB

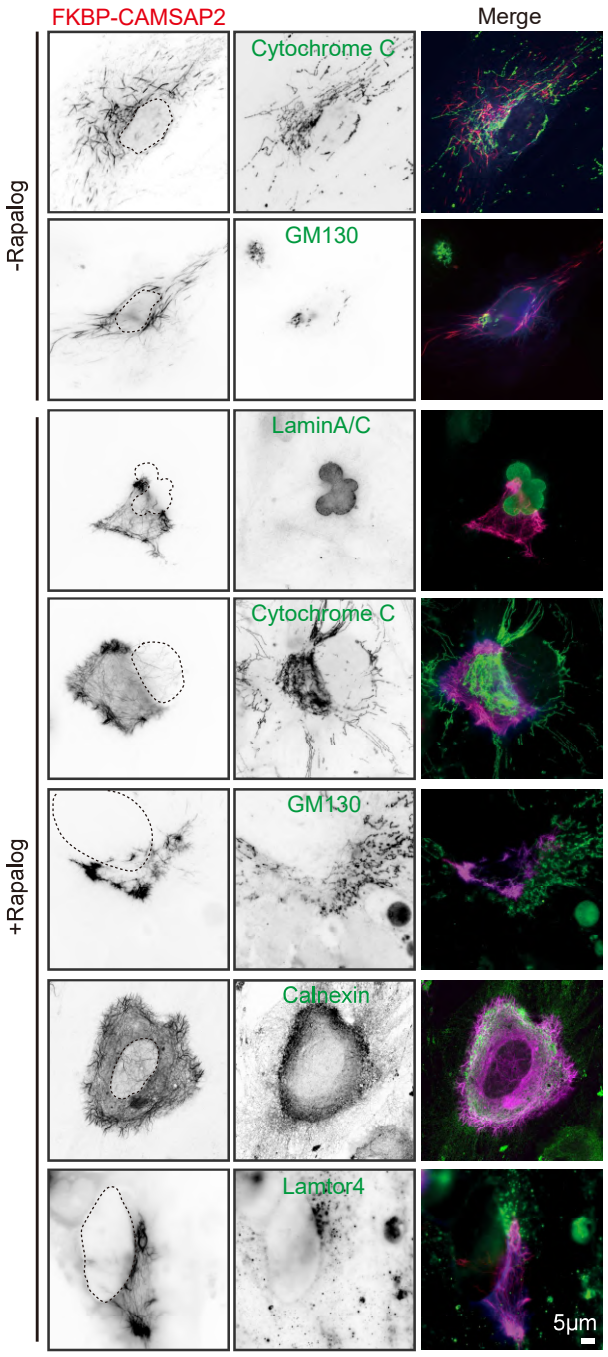

C AKAP450/CAMSAP2/p53/PCNT KO, +CentB + Rapa

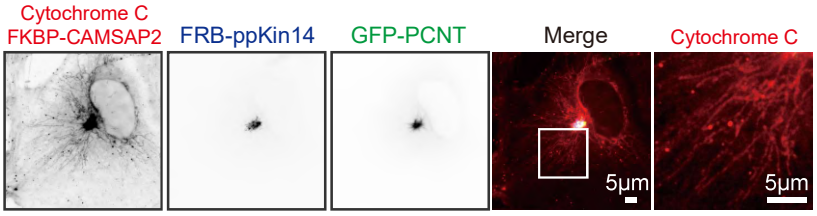

D

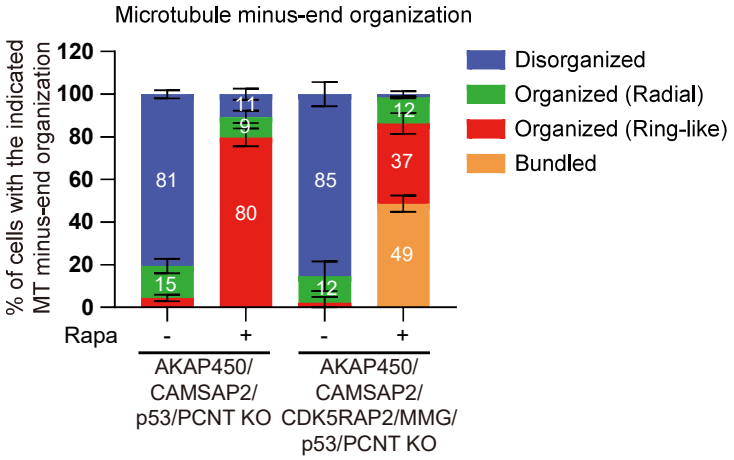

E AKAP450/CAMSAP2/CDK5RAP2/MMG/p53/PCNT KO, +CentB + Rapa

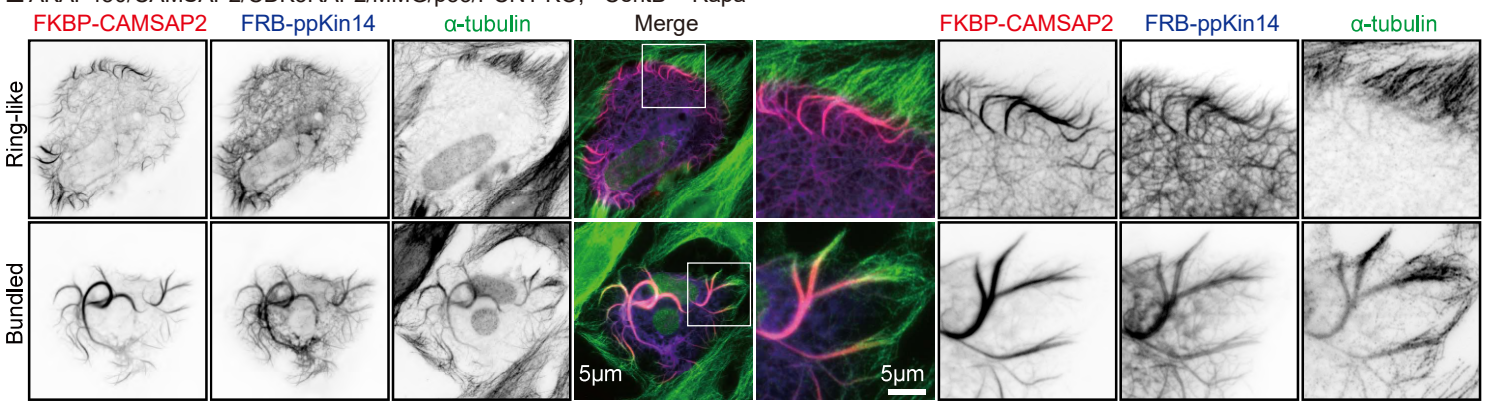

Figure 1 - figure supplement 1

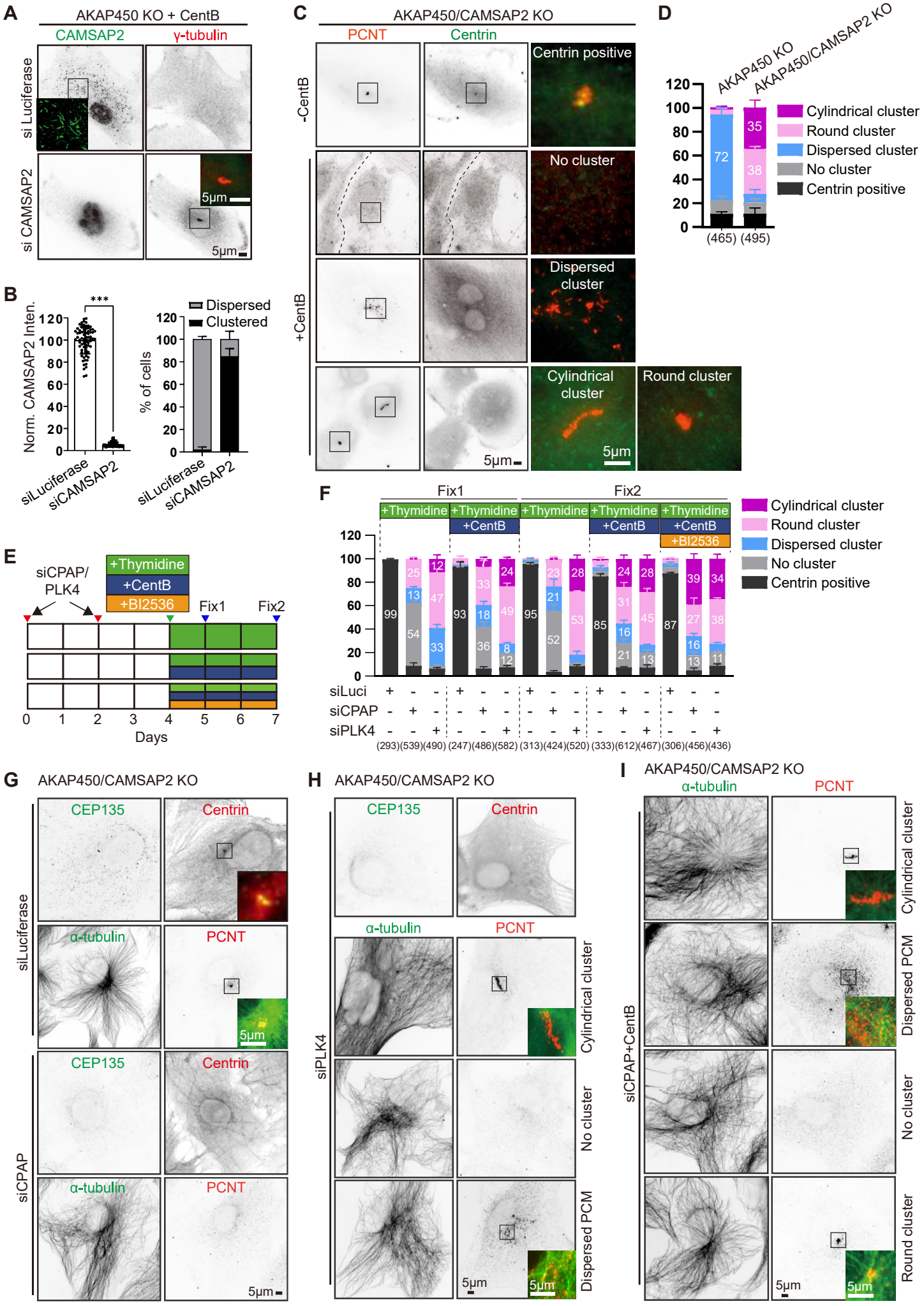

Figure 1 - figure supplement 2

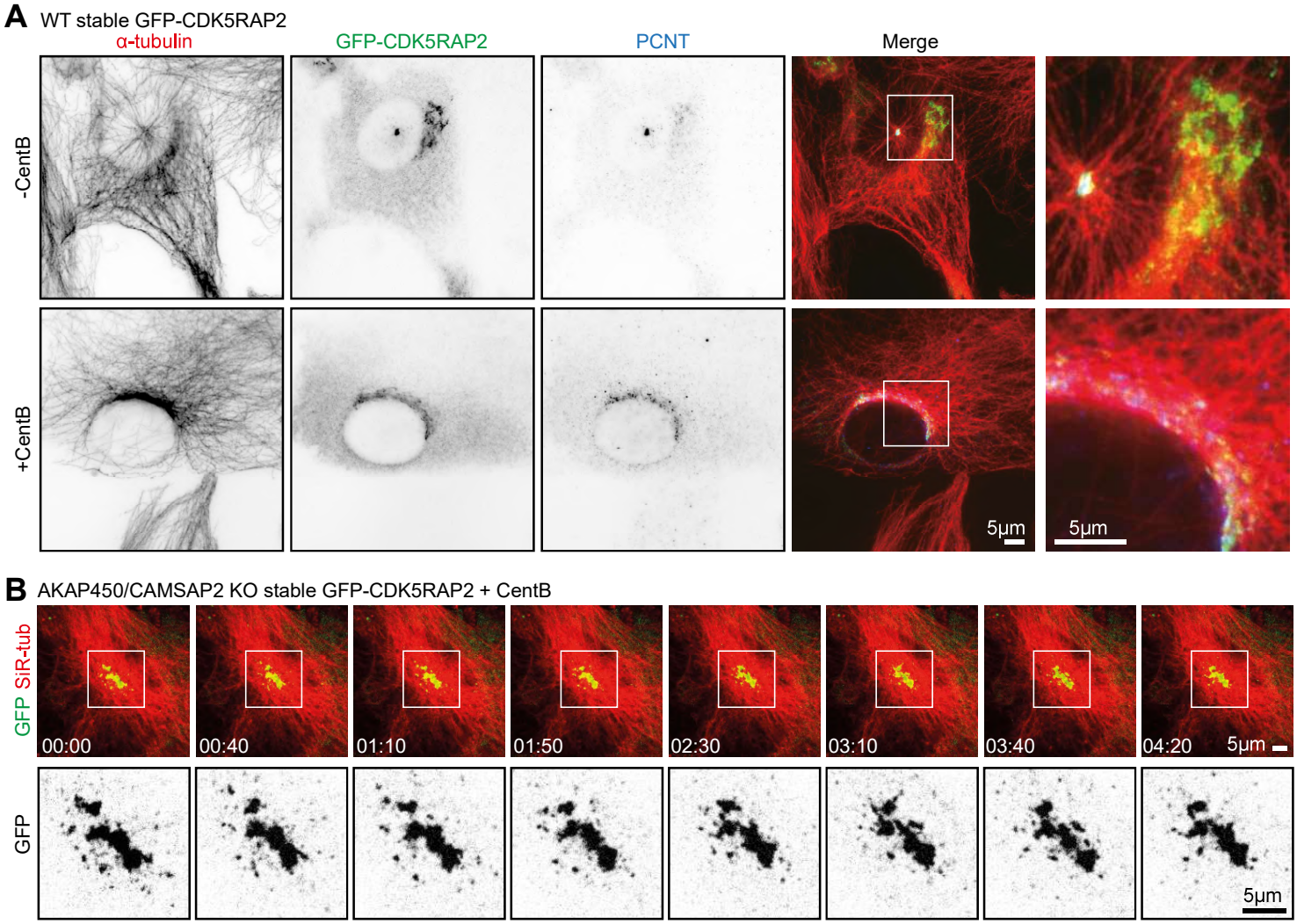

Figure 2- figure supplement 1

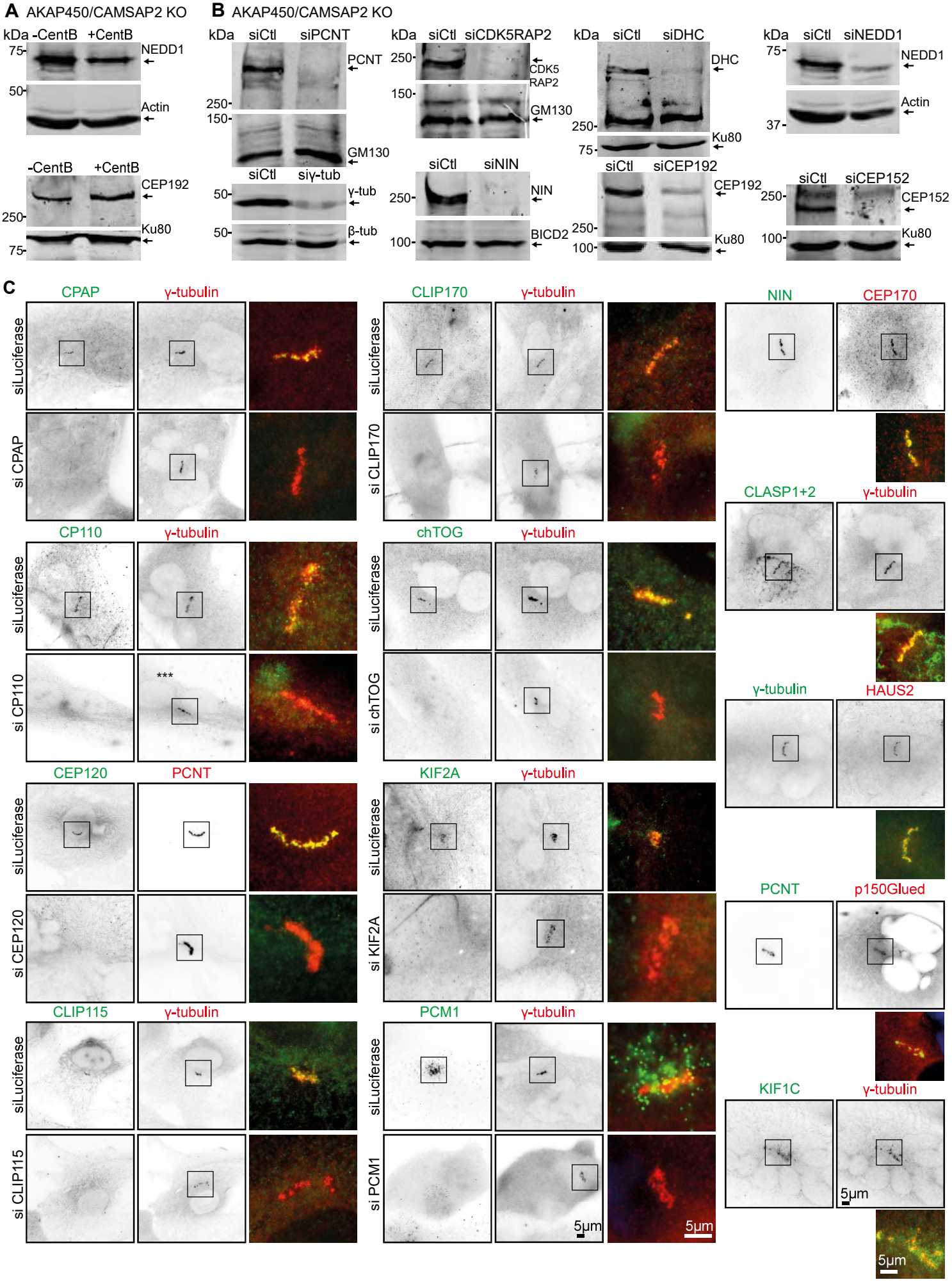

Figure 2 - figure supplement 2

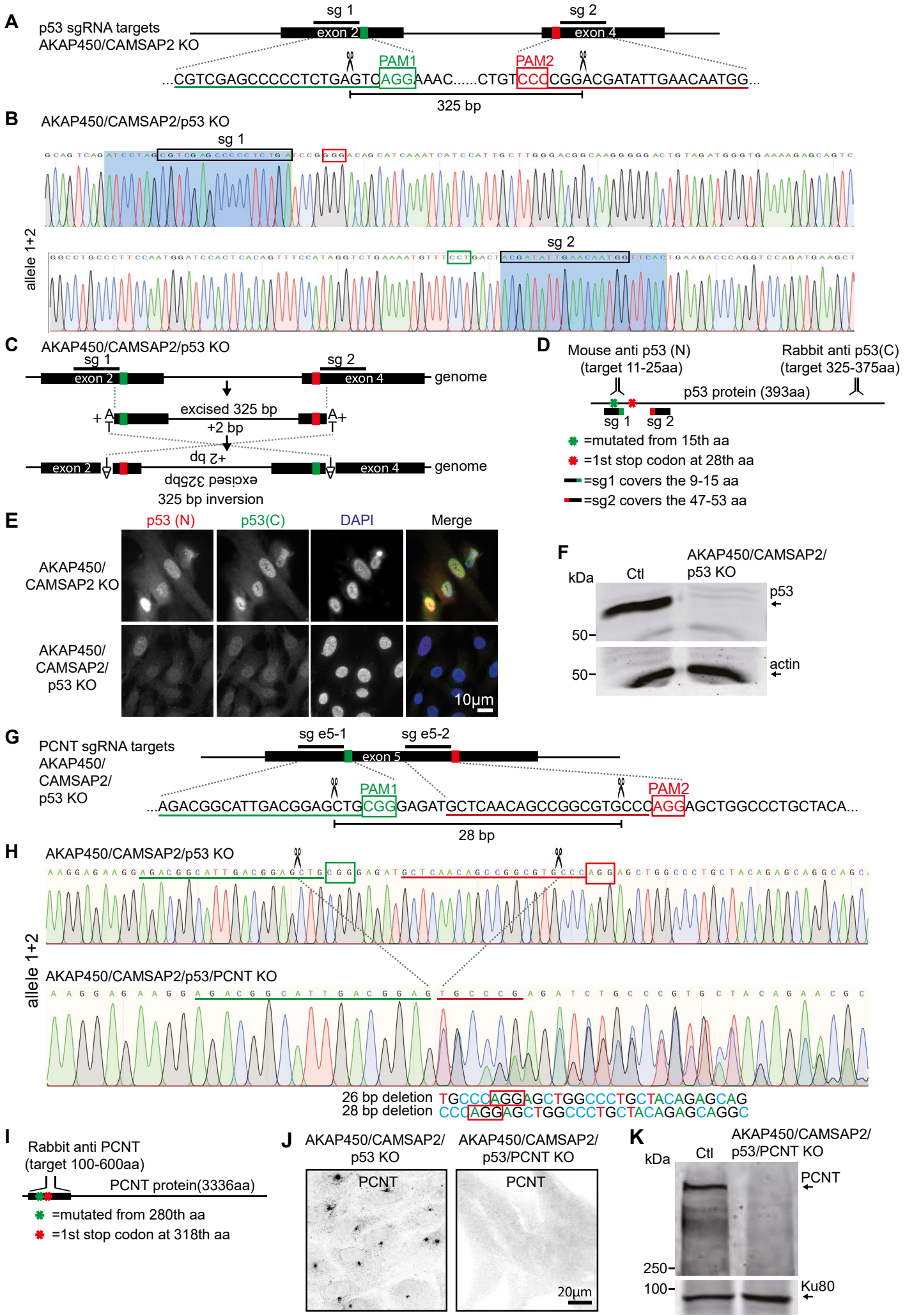

Figure 2 - figure supplement 3

Ctl=AKAP450/CAMSAP2/p53 KO + CentB

PCNT KO=AKAP450/CAMSAP2/p53/PCNT KO + CentB

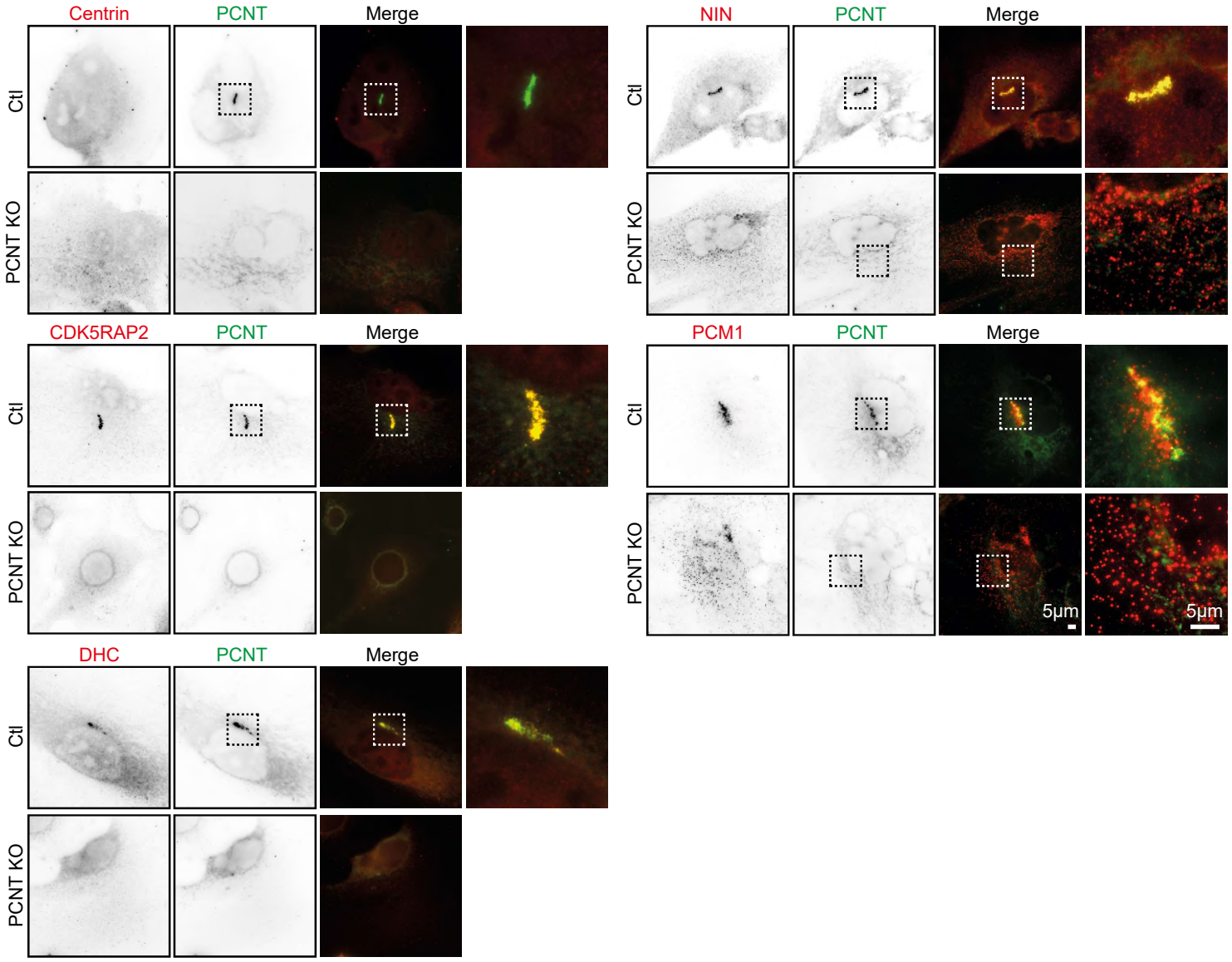

Figure 2 - figure supplement 4

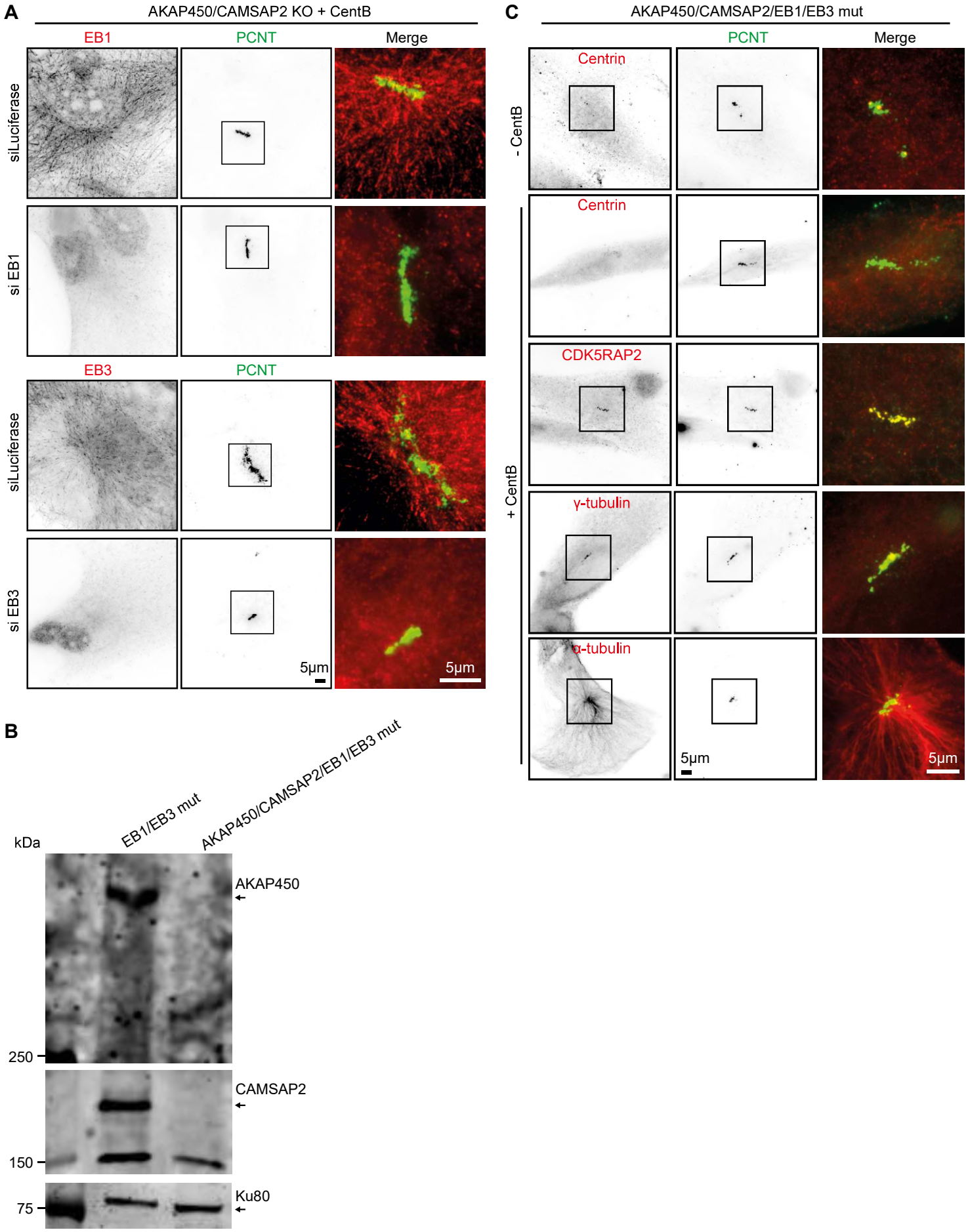

Figure 4 - figure supplement 1

A

AKAP450/CAMSAP2 KO stable GFP-CDK5RAP2 + CentB + Noco

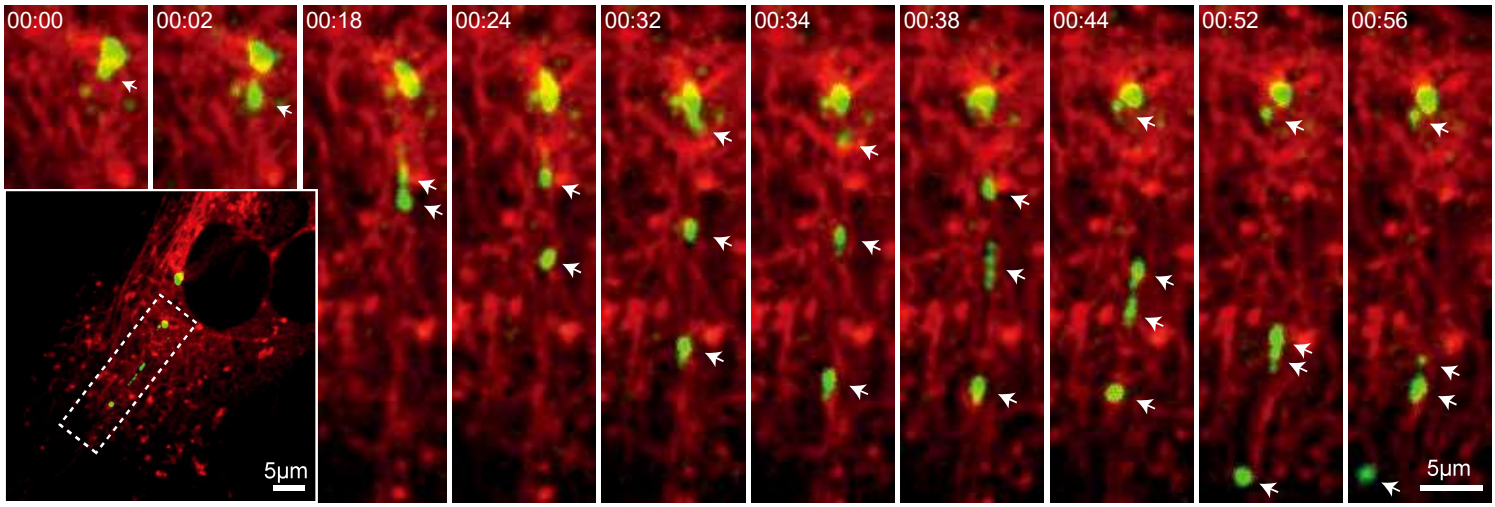

B

AKAP450/CAMSAP2 KO + CentB

-Noco | +Noco (10µM, 15min)

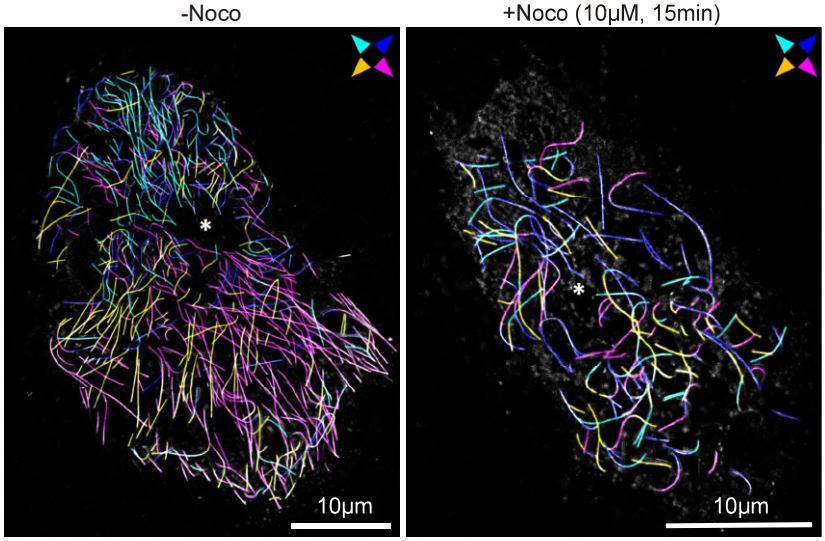

Figure 5 - figure supplement 1

A AKAP450/CAMSAP2 KO + CentB, Noco washout

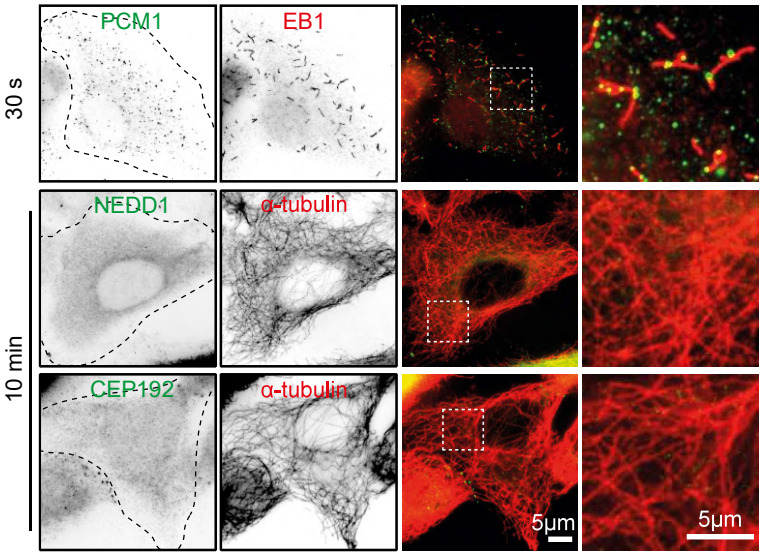

B Presence of PCM proteins in clusters before/after Noco washout

CentB	-	+	+	+	+	+
Nocodazole	-	-	+	+	+	+
Washout			30 s	2 min	5 min	10 min
PCNT	+	+	+	+	+	+
CDK5RAP2	+	+	+	+	+	+
γ-tubulin	+	+	+	+	+	+
NEDD1	+	-	-	-	-	-
Ninein	+	+	-	+	+	+
CEP192	+	-	-	-	-	-
PCM1	+	+	+	+	+	+

C AKAP450/CAMSAP2 KO + CentB, Noco washout 2 min

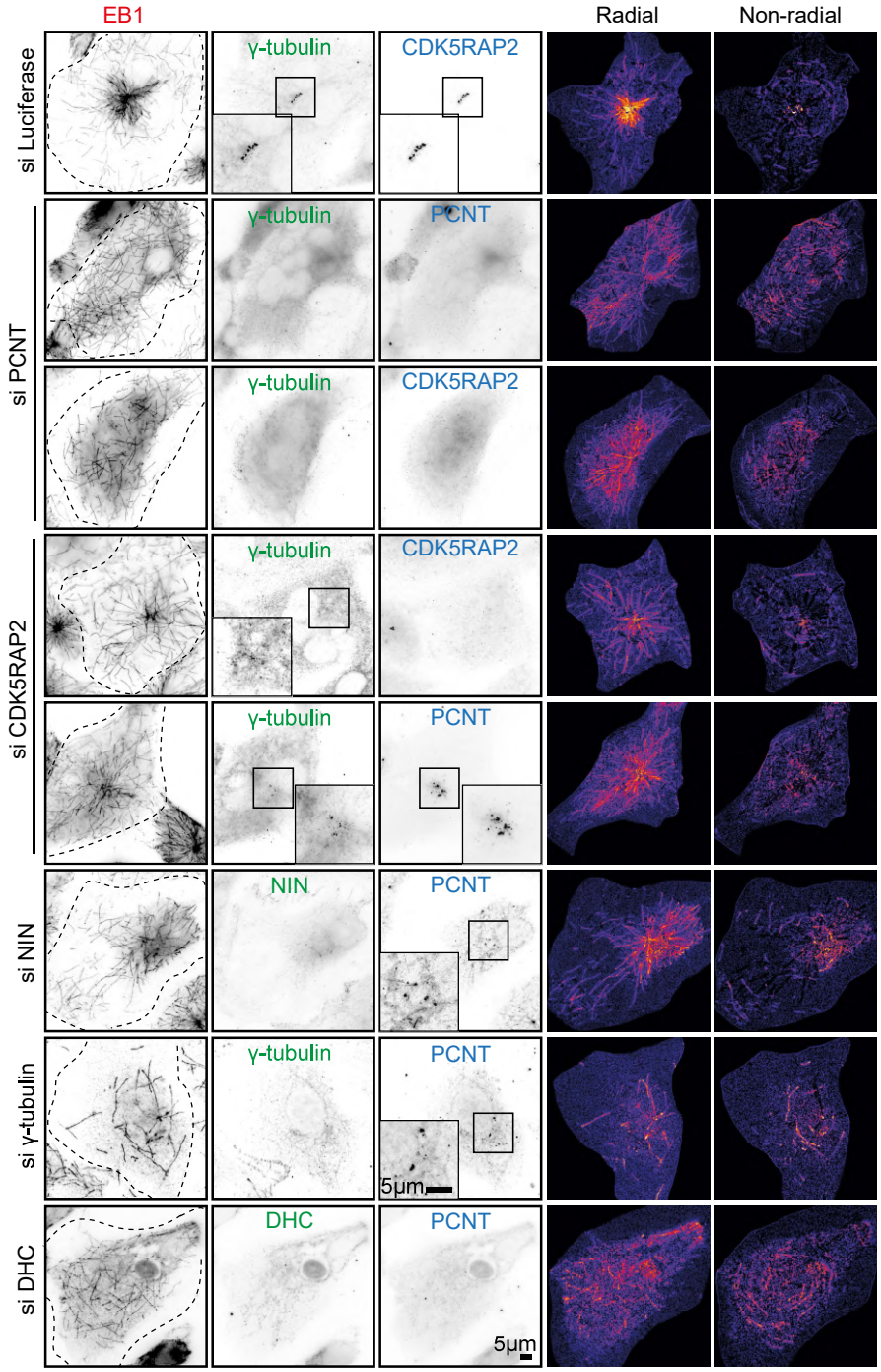

D

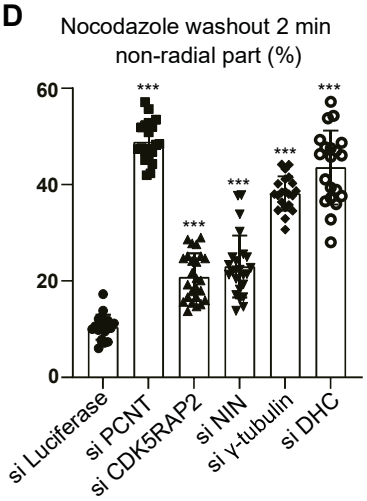

E AKAP450/CAMSAP2 KO CentB

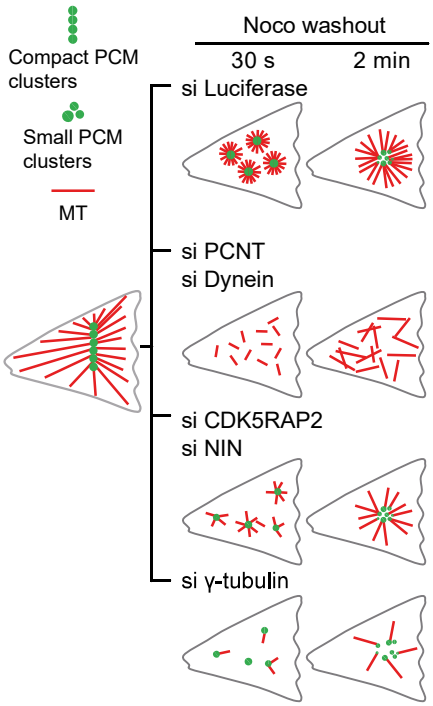

Figure 5 - figure supplement 2

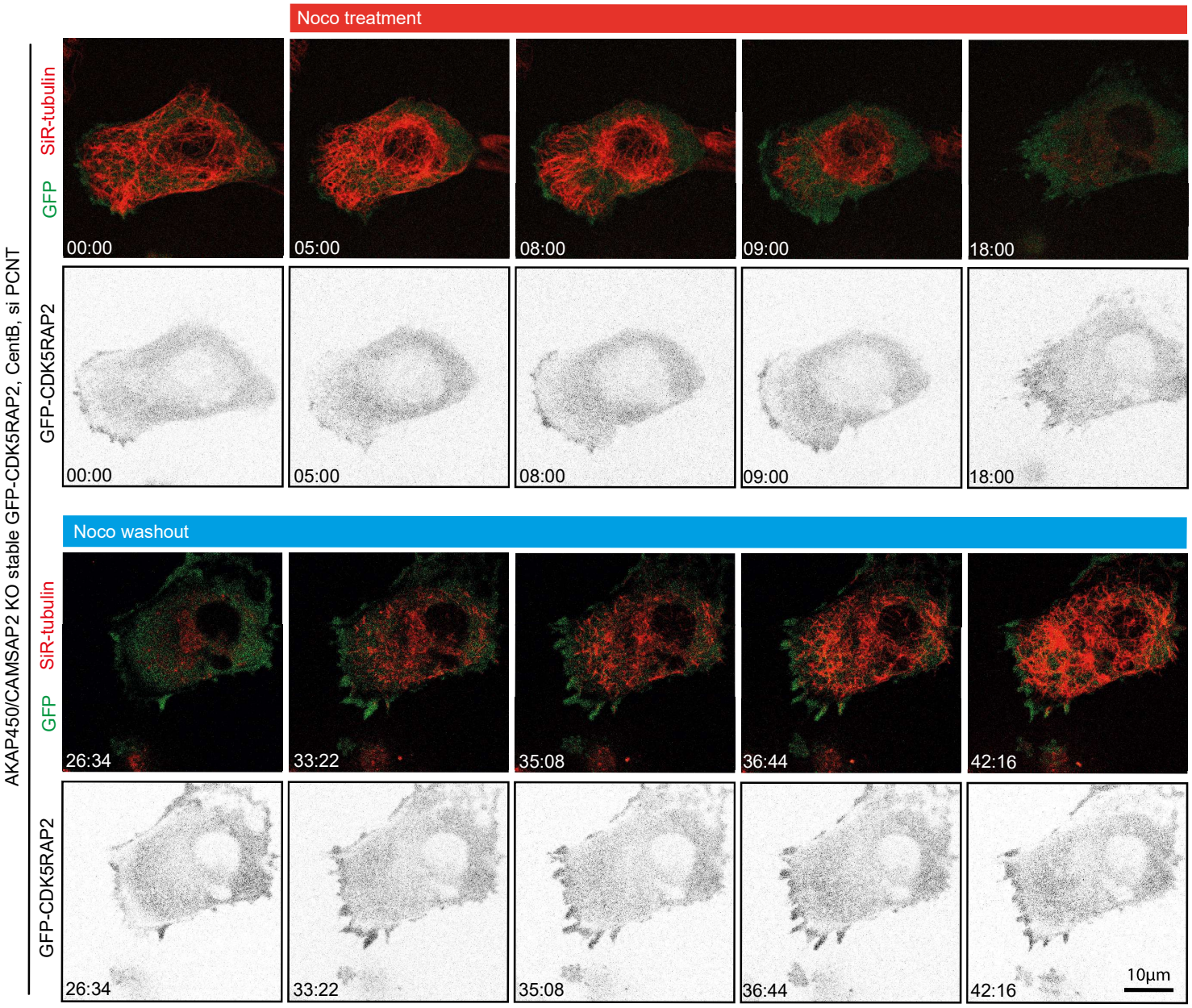

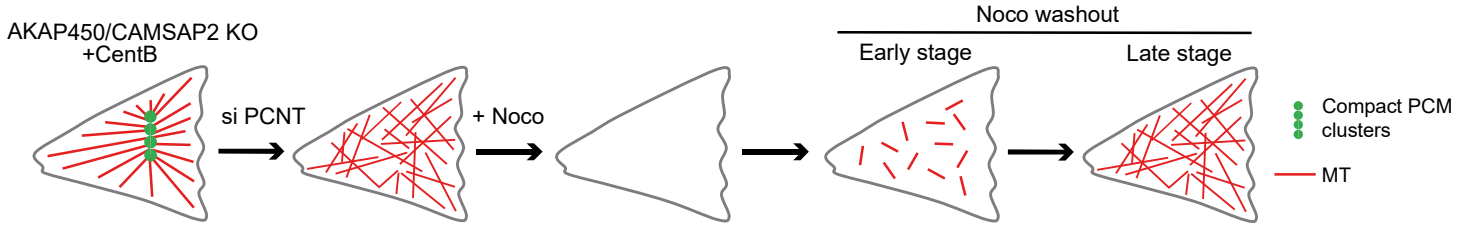

Figure 6 - figure supplement 1

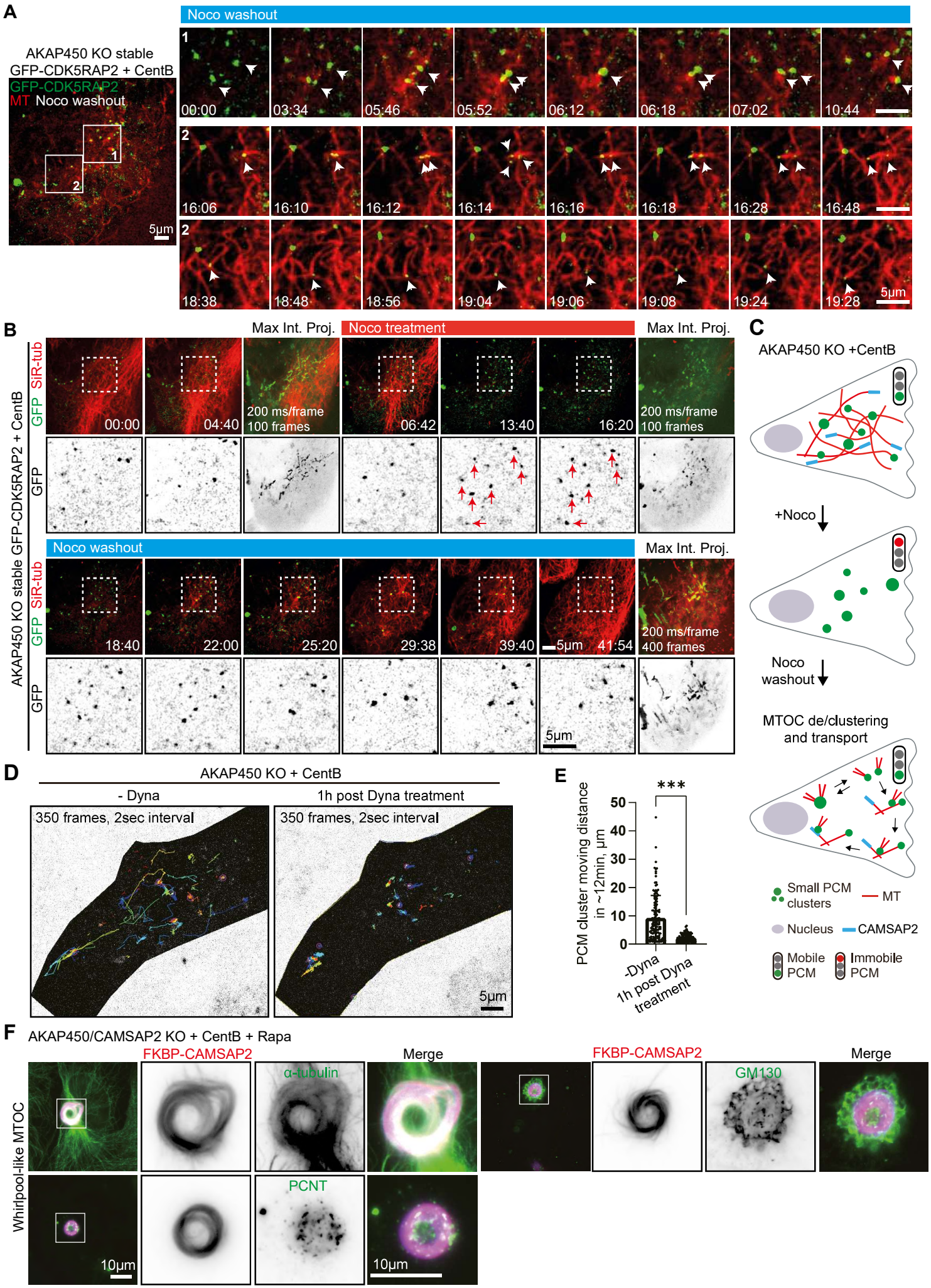

Figure 6 - figure supplement 2

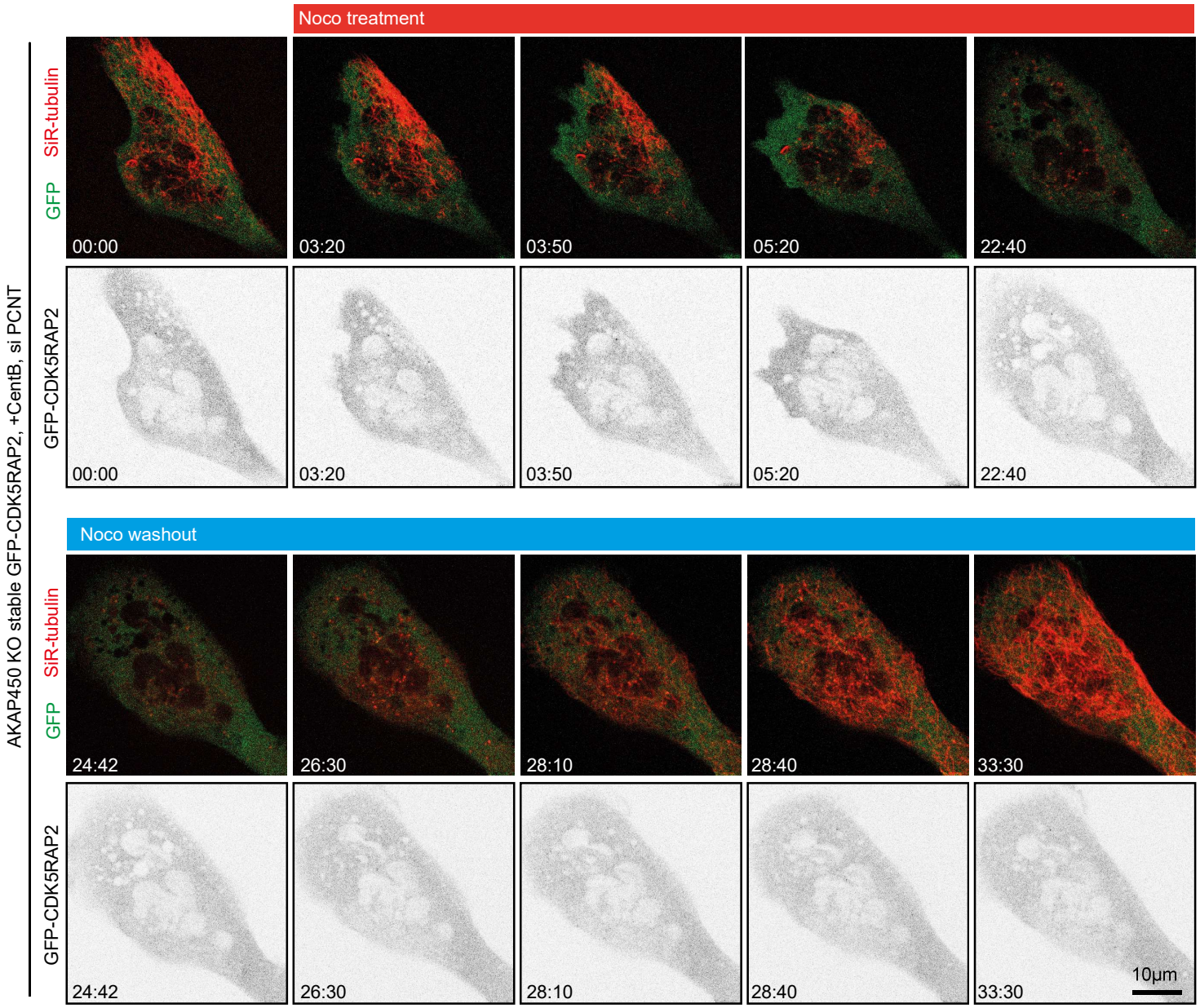

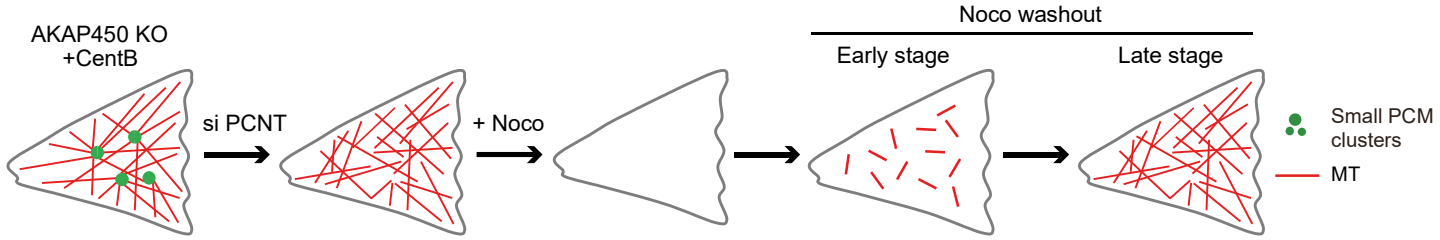

Figure 7 - figure supplement 1

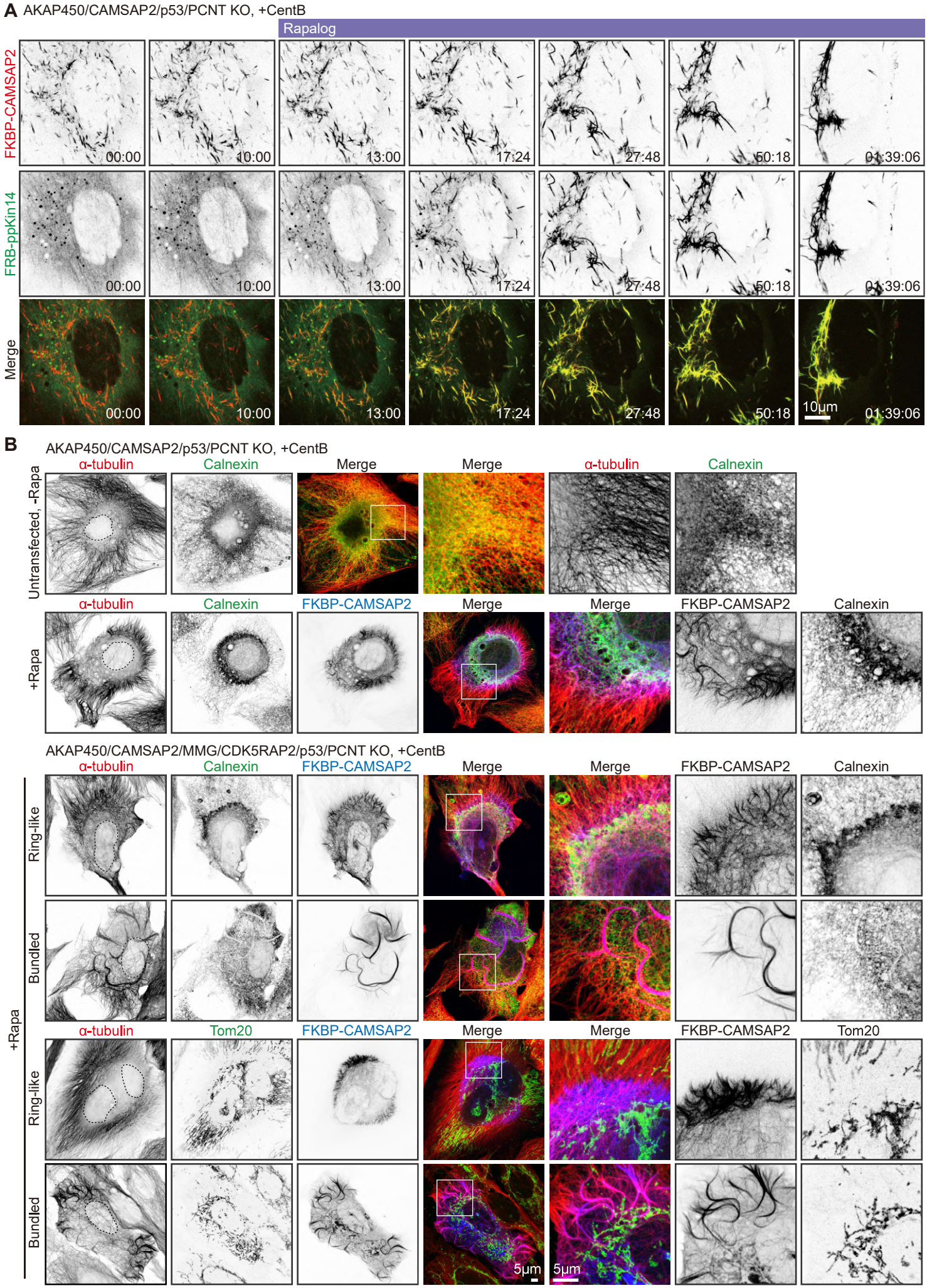

Figure 7- figure supplement 2

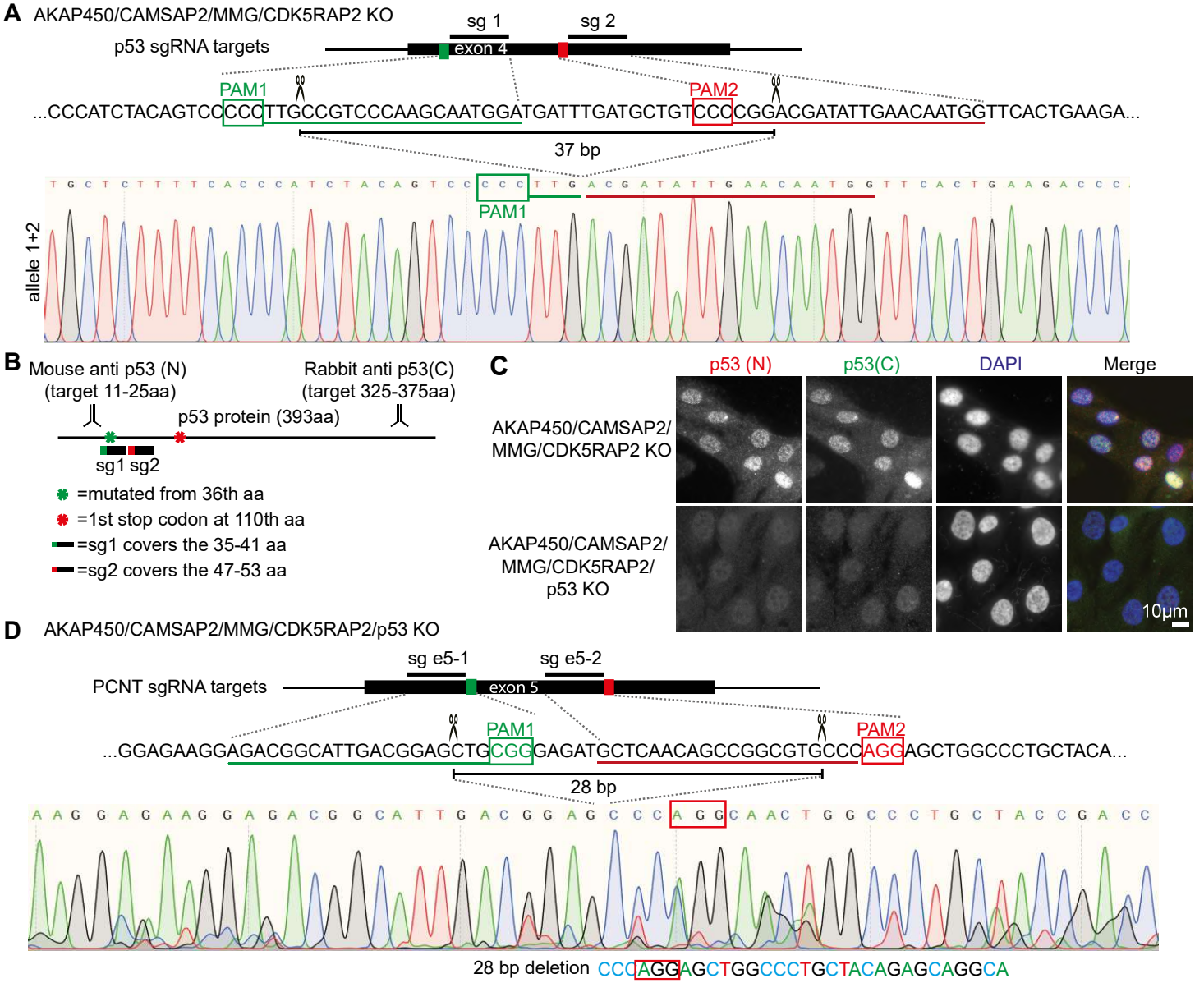

Source data 1
Uncropped Western blots shown in this manuscript

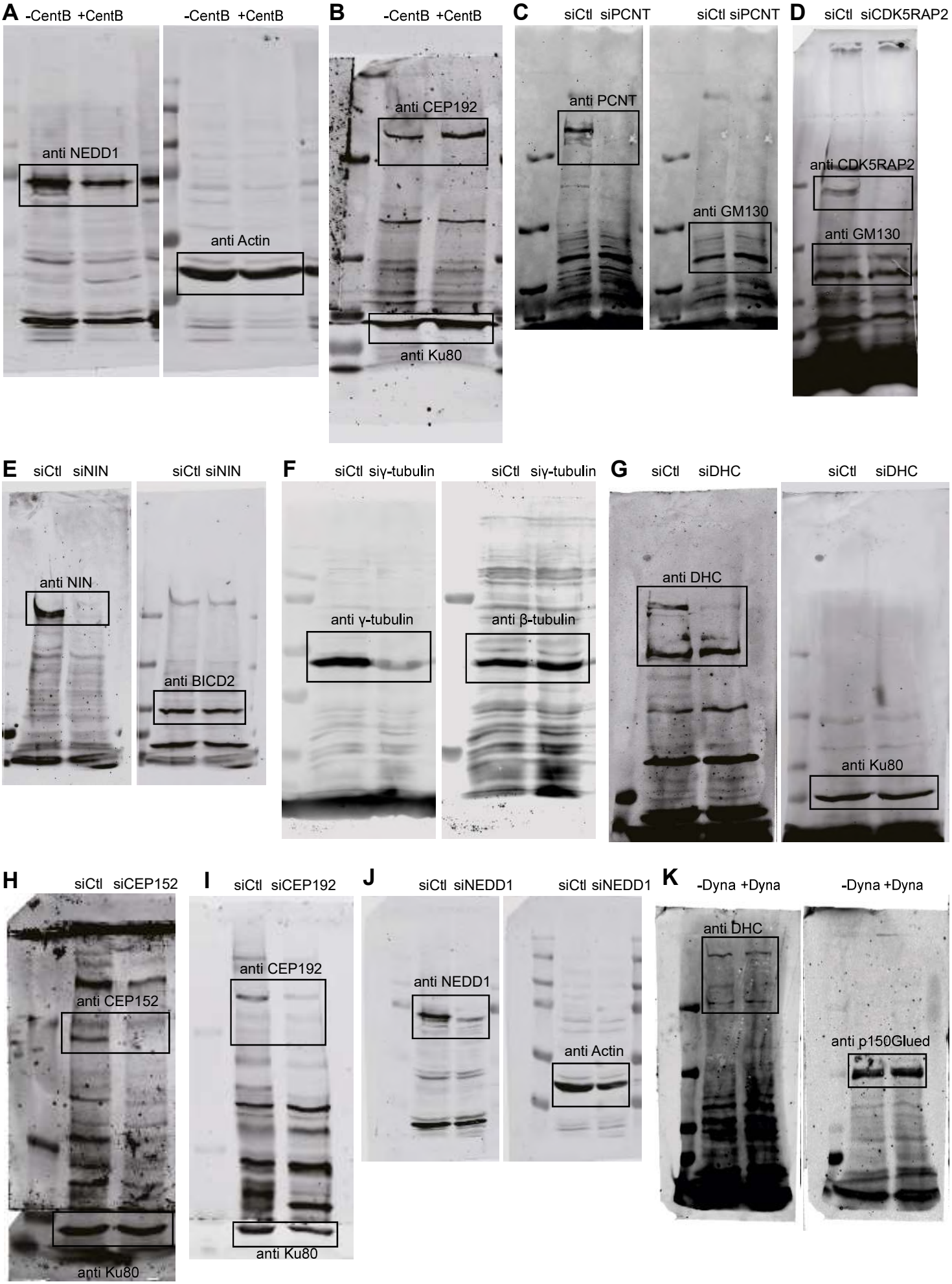
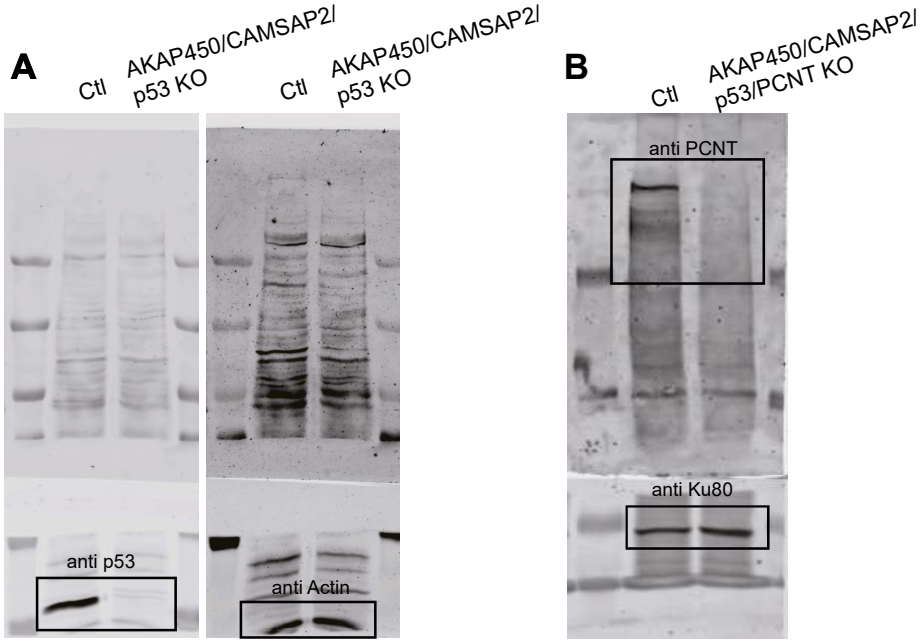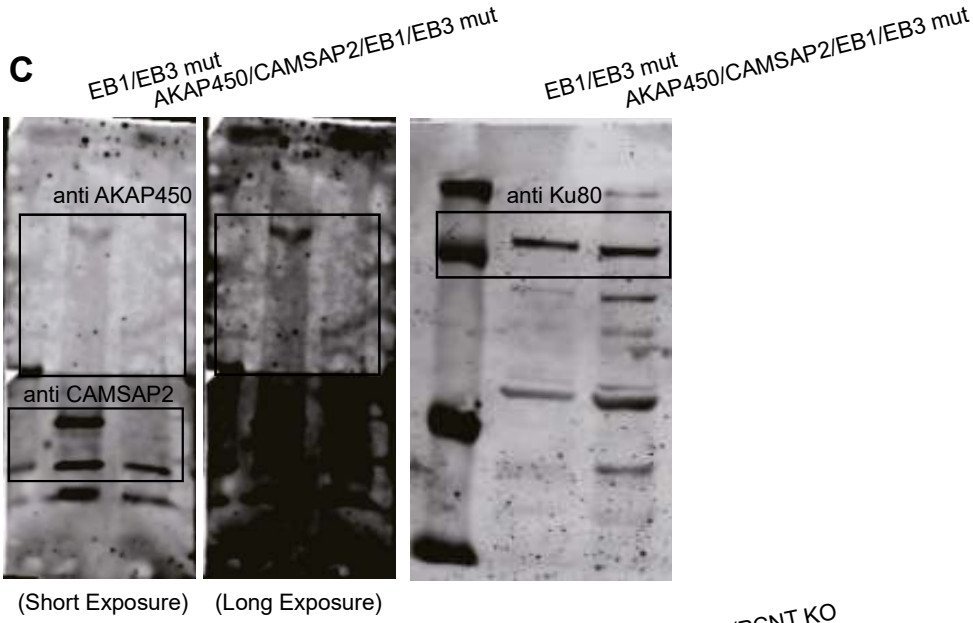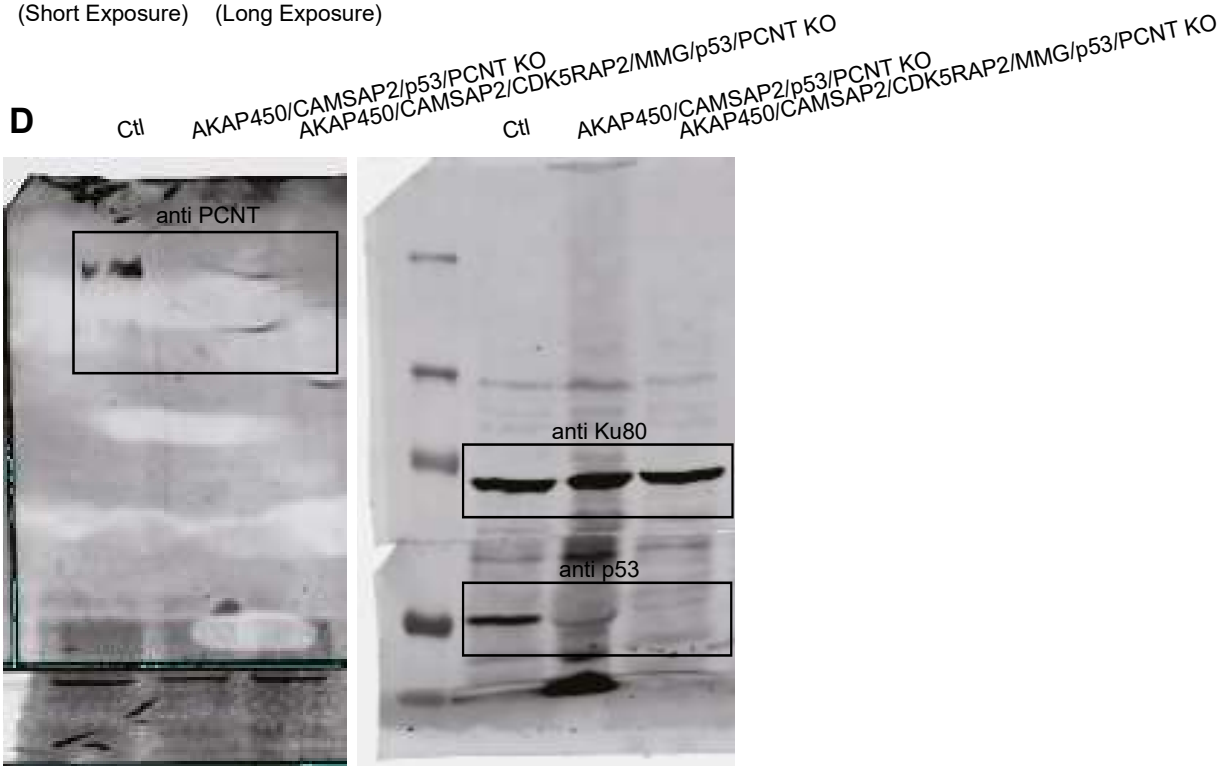
Source data 2
Uncropped Western blots shown in this manuscript